

**High-Resolution Characterization of Model Lipid Membranes
and their Interaction with Cholera Toxin**

By

CHAD EDWARD MILLER

B.S. (California Polytechnic State University, San Luis Obispo) 2000

DISSERTATION

Submitted in partial satisfaction of the requirements for the degree of

DOCTOR OF PHILOSOPHY

in

Biophysics

in the

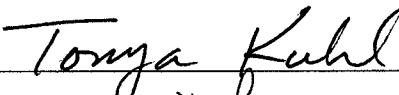
OFFICE OF GRADUATE STUDIES

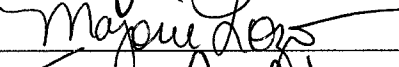
of the

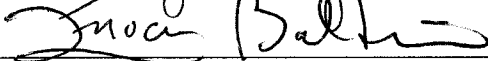
UNIVERSITY OF CALIFORNIA

DAVIS

Approved:







Committee in Charge

2005

UMI Number: 3203595

INFORMATION TO USERS

The quality of this reproduction is dependent upon the quality of the copy submitted. Broken or indistinct print, colored or poor quality illustrations and photographs, print bleed-through, substandard margins, and improper alignment can adversely affect reproduction.

In the unlikely event that the author did not send a complete manuscript and there are missing pages, these will be noted. Also, if unauthorized copyright material had to be removed, a note will indicate the deletion.

UMI[®]

UMI Microform 3203595

Copyright 2007 by ProQuest Information and Learning Company.

All rights reserved. This microform edition is protected against unauthorized copying under Title 17, United States Code.

ProQuest Information and Learning Company
300 North Zeeb Road
P.O. Box 1346
Ann Arbor, MI 48106-1346

Table of Contents

<u>Abstract.....</u>	<u>1</u>
----------------------	----------

<u>Chapter 1: Cholera Toxin Assault on Lipid Monolayers Containing Ganglioside GM₁: A Neutron Reflectivity Study.....</u>	<u>3</u>
--	----------

Chapter Abstract.....	3
Introduction.....	3
Experimental Section.....	6
Materials	6
Neutron Reflectivity.....	7
Results and Discussion.....	8
Table 1-1:.....	11
Table 1-2:.....	19
Conclusion.....	24

<u>Chapter 2: Cholera Toxin Assault on Lipid Membranes Containing Ganglioside GM₁: An X-ray Reflectivity and Grazing Incidence Diffraction Study at the Air-Water Interface.....</u>	<u>25</u>
---	-----------

Chapter Abstract.....	25
Introduction.....	25
Experimental Section.....	28
Materials	28
Grazing Incident X-Ray Diffraction	29
X-ray Reflectivity	31
Beam Damage.....	32
Results.....	33
Pressure – Area Isotherms.....	33
Area Expansion Analysis.....	33
Reflectivity Analysis (pH=8).....	35
Reflectivity Analysis (pH=5).....	39
GIXD Analysis (pH=8).....	44
GIXD Analysis (pH=5).....	55
Discussion/Conclusions.....	62
Table 2-1.....	65
Table 2-2.....	65
Table 2-3.....	66
Table 2-4.....	67

Chapter 3: Characterization of Single Biological Membranes at the Solid-Liquid

***Interface by X-Ray Reflectivity* 68**

Chapter Abstract..... 68

Introduction..... 68

Experimental Section..... 71

Results and Discussion..... 73

 Table 3-1:..... 76

 Table 3-2:..... 78

Chapter 4: Grazing Incidence Diffraction of Cadmium Arachidate Multilayers at the

***Solid-Liquid Interface* 81**

Chapter Abstract..... 81

Introduction..... 81

Experimental Section..... 82

 X-ray Reflectivity 83

 Grazing Incidence Diffraction 85

 Beam Damage..... 87

Results 88

 Reflectivity..... 88

 Grazing Incidence Diffraction 89

 Table 4-1 91

 Table 4-2..... 92

Discussion/Conclusions..... 95

Acknowledgments..... 95

References 96

Chad Edward Miller
December 2005
Biophysics
Advisor: Tonya L. Kuhl

**High-Resolution Characterization of Model Lipid Membranes
and their Interaction with Cholera Toxin**

Abstract

Many bacterial toxins bind to and gain entrance to target cells through specific interactions with membrane components. This work has characterized the structure of cholera toxin before and during binding to lipid monolayers. To reap its destructive effects on the cell, cholera toxin must bind to and infiltrate the cellular membrane, a specialized and controlled barrier. The mechanism by which cholera toxin crosses the membrane remains unresolved. These studies using neutron/x-ray reflectivity (NR/XR) and x-ray grazing incidence diffraction (GIXD) provide clues that membrane perturbation caused by cholera toxin's binding unit can initiate uptake into the cell and support the important role of low endosomal pH in the infection pathway. Our findings suggest that the B₅ pentamer plays a more active role in the membrane penetration mechanism than solely binding cholera toxin to its cell surface receptor and suggest that the mechanism of membrane translocation by the protein may be aided by alterations in lipid packing. Structural parameters such as the density and thickness of the lipid layer, extension of the GM₁ oligosaccharide headgroup, and orientation and position of the protein upon binding are reported.

This work also demonstrates that 18 keV x-rays can be used to perform reflectometry on single, phospholipid bio-membranes at the solid-liquid interface. Previously, characterization of biomimetic structures normal to a "buried" interface was

the domain of neutron reflectivity. The increased dynamic range of x-ray reflectivity over comparable neutron reflectivity measurements enabled the density distribution of the membranes to be determined with much greater precision allowing subtle features in membrane structure and leaflet segregation to be revealed. Using x-rays to study biological systems has birthed the possibility of using GIXD to study lipid membranes in a fully hydrated state. Using complementary XR and GIXD, these studies have characterized the structure of supported thin-organic layers in contact with water. The goal was to demonstrate the feasibility of similar experiments to study much thinner single bilayer bio-membranes. These studies are the first successful GIXD experiments of ultra thin-organic films composed of a few layers at the solid-liquid interface.

Chapter 1: Cholera Toxin Assault on Lipid Monolayers Containing Ganglioside GM₁: A Neutron Reflectivity Study

Chapter Abstract

Many bacterial toxins bind to and gain entrance to target cells through specific interactions with membrane components. Using neutron reflectivity, we have characterized the structure of mixed DPPE: GM₁ lipid monolayers before and during the binding of cholera toxin (CTAB₅) or its B subunit (CTB₅). Structural parameters such as the density and thickness of the lipid layer, extension of the GM₁ oligosaccharide headgroup, and orientation and position of the protein upon binding are reported. The density of the lipid layer was found to decrease slightly upon protein binding. However, the A subunit of the whole toxin is clearly located below the B pentameric ring, away from the monolayer, and does not penetrate into the lipid layer prior to enzymatic cleavage. Using Monte Carlo simulations, the observed monolayer expansion was found to be consistent with geometrical constraints imposed on DPPE by multivalent binding of GM₁ by the toxin. Our findings suggest that the mechanism of membrane translocation by the protein may be aided by alterations in lipid packing.

Introduction

Many bacterial toxins bind to and gain entrance to target cells through specific interactions with membrane components. One such example is cholera toxin (CTAB₅), a pathologically active agent secreted by the bacterium *Vibrio cholerae* [1]. The toxin has an AB₅ arrangement of subunits. Five identical B subunits (CTB₅), each composed of 103 amino acids, form a pentameric ring with a vertical height of 32Å and a radius of

31Å [2, 3]. CTB₅ is responsible for binding the toxin to its cell-surface receptor, ganglioside GM₁. The single A-unit is a disulfide-linked dimer composed of an A1 and A2-subunit that is aligned through the central pore “doughnut hole“ of the B₅ subunit. After proteolytic cleavage (between residues 192 and 194) and reduction of the disulfide bond (cys187=cys199), it has been proposed that the A1 peptide crosses the cell membrane and reaches the cytoplasmic face [4]. There, it interacts with integral membrane proteins, disrupting their normal function, resulting in a large efflux of water and ions from the cell (severe diarrhea) [5]. Although much is known about the structure and catalytic activity of cholera toxin, the mechanism by which cholera toxin crosses the plasma membrane remains unknown.

Because of its detrimental effect on health, cholera toxin has been the focus of many studies. Several different methods have shown that the B₅ portion of the toxin is responsible for binding to lipid membranes containing GM₁. Experiments involving electron microscopy, ellipsometry, and flow cytometry indicate that cholera toxin has minimal non-specific adsorption to lipid membranes in the absence of GM₁ [6-8]. Flow cytometry has further shown that CTAB₅ binds to GM₁ with a 100-fold larger affinity than CTB₅ [7]. Because binding is multivalent (one B monomer per GM₁), off-rates of the toxin are slow. If the concentration of GM₁ receptor is large enough, it is possible for macroscopic, two-dimensional cholera toxin crystals to be assembled with high coverage [6]. At the molecular level, AFM studies have shown that CTB₅ binds to GM₁ rich domains of lipid bilayers [9, 10]. Electron microscopy, impedance spectroscopy, and surface plasmon resonance have shown with moderate confidence that the A unit faces away from the lipid layer when bound [8, 11].

In the last few years there has been an increased interest in using neutron reflectivity (NR) to study biological or biomimetic thin films. NR is a novel method for characterizing protein adsorption and penetration into lipid layers. The technique allows the average structure of a thin film at an interface to be determined (depth profiling). Averaging over an area of a few square centimeters, NR is sensitive to the structure of homogeneous samples with Ångstrom resolution. However, a smooth, planar geometry is required for detection of the reflected neutron beam. This constraint prevents NR from being used on actual cells. Nevertheless, model biological membranes (at the air-liquid and solid liquid interface) can be designed to mimic the structure and function of cellular membranes under physiological conditions [12]. Compared to other structural characterization techniques, NR has the ability to observe a system in its native state and does not require fixation, staining, or low vacuum. Studies have investigated protein adsorption (including protein/surfactant mixtures), model biomembranes [13, 14], and the nature of protein-membrane interactions. Krueger Review (2001) provides an excellent summary of previous studies on biomembranes and protein-membrane interactions using NR. For example, NR has been used to show the importance of metal ion chelation in myoglobin adsorption to lipid monolayers at the air-water interface [15]. NR combined with x-ray scattering techniques has been used to observe the reconstitution of supramolecular S-layer protein self-organization at a lipid interface [16, 17]. NR has also been used to study lipid-solvent interactions to determine the hydration of phosphatidylcholine headgroups by D₂O as a function of surface pressure and lipid phase [18]. Combined with other techniques such as x-ray reflectivity, x-ray grazing incidence diffraction, fluorescence microscopy, atomic force microscopy, and surface force

apparatus (SFA) measurements, NR is a powerful tool for characterizing the structure of thin biomimetic films.

We have used neutron reflectivity to characterize the structure of lipid monolayers with cholera toxin bound in its native state to its receptor, GM₁. At a resolution of a few Ångstroms, the glycol-lipid extension of GM₁ (cholera toxin's lipid receptor), the orientation of the bound cholera toxin molecule and the distance between the protein layer and the lipid layer have been identified. Our studies performed at the air-liquid interface along with previous knowledge of the three-dimensional crystal structure of CTAB₅ and CTB₅ at 2.5Å resolution [2, 3] have provided an opportunity to examine and compare the correlations between structure and function of the toxin.

Experimental Section

Materials

Lipid monolayers were studied at the air-water interface using a Langmuir trough designed to fit at the horizontal reflectometer beamline (NG7) at the National Institute of Standards and Technology (NIST), Center for Neutron Research (NCNR, Gaithersburg, MD). The lipid monolayer was composed of 80:20 mole % of d-DPPE: GM₁ [deuterated 16:0 1,2-Dipalmitoyl-D62-*sn*-Glycero-3-Phosphoethanolamine: Galactosyl-N-Acetylgalactosaminy (N-acetyl-neuraminy) Galactosylglucosylceramide (GM₁ Ganglioside)]. GM₁ and d-DPPE were obtained from Avanti Polar Lipids* and were used without further purification. Cholera Toxin CTAB₅ was purchased from BioMol Research Labs and CTB₅ was purchased from Sigma. D₂O was obtained from Cambridge

* Identification of a commercial product does not imply endorsement by the National Institute of Standards and Technology

Isotope Laboratories; Inc. Lipids were dissolved in chloroform:methanol 90:10 (~1.2mg/mL), mixed to obtain a 80:20 mole ratio, and deposited on H₂O or D₂O buffer (170 mM NaCl, 1.4 mM NaN₃, 0.3mM EDTA, 15mM Trizma-HCl, pH = 5.5 – 6.1) subphase. The molar composition of the monolayer, surface pressure of 20 mN/m, and temperature of 20°C were held constant for all experiments reported here.

Neutron Reflectivity

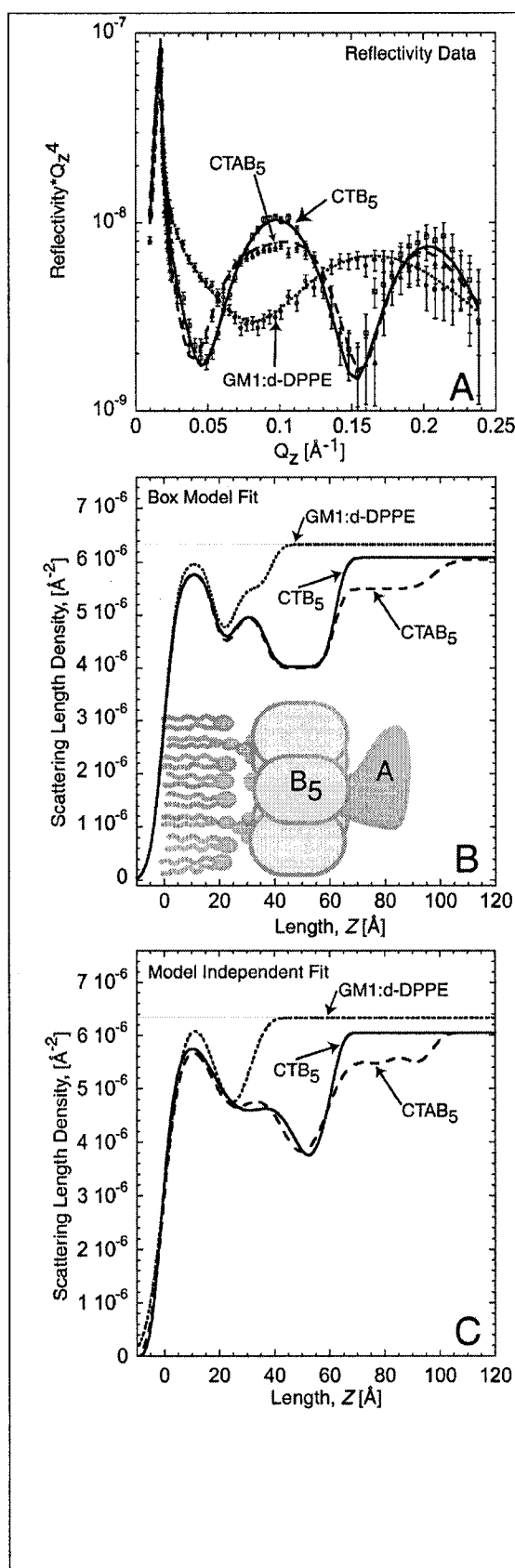
Reflectivity, R , is defined as the intensity ratio of neutrons elastically and specularly scattered from the surface relative to the incident neutron beam. When measured as a function of wave-vector transfer ($Q_z = |\mathbf{k}_{out} - \mathbf{k}_{in}| = 4\pi\sin\alpha/\lambda$, where α is the angle of incidence and λ is the wavelength of the neutron beam), the reflectivity curve contains information regarding the sample-normal profile of the in-plane average of the coherent scattering length densities. Using a 4.75 Å wavelength neutron beam, the reflectivity as a function of Q_z values from 0.01 to 0.24 Å⁻¹ was determined with reasonable statistics to values of $R \sim 10^{-6}$. Typical scanning times for this Q_z range were 3 hours. The reflected neutrons were counted using an Ordela position sensitive ³He detector. The data was reduced and plotted as RQ_z^4 versus the perpendicular scattering vector, Q_z (this accounts for a sharp Q_z^{-4} decrease of the reflectivity due to the Fresnel's law). The error bars on the data represent the statistical errors in the measurements (standard deviation, σ_R) where the uncertainty in the Q_z resolution, $\sigma_{Q_z}/Q_z \approx 2\%$, was nearly constant over this scattering vector range. Analysis on the measured reflectivity curves was performed using two methods. The first method was a cubic beta spline fitting

routine [19]. In this case, the best fit to the experimentally obtained reflectivity profile was obtained without user-defined constraints based on physical characteristics of the system. In the second method, the structural components of the system were divided into homogeneous molecular slabs or boxes of different scattering length density. These boxes, which physically represent different portions of the lipid-protein layers, were then refined using a least-squared method [20]. As a result, method 2 provides the thickness of each layer (box), scattering length density ($\beta(z)$), and adjacent interfacial roughness, enabling the structural components perpendicular to the interface to be resolved. In general, consistency between the two models indicates a good representation of the system in real space.

Results and Discussion

Reflectivity measurements of the lipid-toxin system at the air-water interface enabled the average scattering length density profile normal to the interface to be determined. The experimentally measured reflectivity profiles for (1) the mixed d-DPPE: GM₁ monolayer, (2) the monolayer with CTB₅, and (3) the monolayer with CTAB₅ on a D₂O subphase are shown in **Fig. 1-1A**. A few qualitative observations can be made directly from the reflectivity profiles. First, from the position of the interference peak maximum in reciprocal space, $Q_z \sim 0.16 \text{ \AA}^{-1}$, the thickness of the lipid monolayer is approximately 40 Å. This corresponds to the total thickness at the interface, including the GM₁ saccharide region. Second, when either CTB₅ or CTAB₅ bind to the monolayer there is a shift in the interference maximum to smaller Q_z values ($\sim 0.1 \text{ \AA}^{-1}$), due to a $\sim 23 \text{ \AA}$ increase in thickness at the interface from protein binding. This total thickness of 60 Å corresponds to the monolayer and protein thickness. More quantitative details can be

obtained using both box model and cubic beta spline fits to the data. The scattering length density profiles, $\beta(z)$, obtained from the box model fits (solid and dashed curves) are shown in **Fig. 1-1B** and reported in **Table 1-1**. **Fig. 1-1C** shows the $\beta(z)$ from the cubic beta spline fitting routine.

**Fig. 1-1:**

A – Neutron reflectivity of the monolayer, monolayer with bound CTB₅, and monolayer with bound CTAB₅. Points with error bars are measured data. Solid and dashed lines indicate fits to the data corresponding to the scattering length density profile in **B**.

B – Scattering Length Density Profile of box model fits shown in **A**. A detailed schematic of the box model is provided in **Fig. 1-2**. In the profile for the monolayer, the lipid tail, head and saccharide regions are clearly distinguishable. When CTB₅ and CTAB₅ are bound, the structure of the lipid monolayer is not significantly altered. The decrease in scattering length density ($\beta(z)$) of the lipid tail and headgroup regions is due to an increase in the area per molecule consistent with geometrical constraints applied when cholera toxin binds GM₁. The A subunit clearly resides below the B₅ pentamer, facing away from the lipid layer.

C – $\beta(z)$ profile from the cubic beta spline fitting routine. Reflectivity fits are not shown in **A** for clarity, but were slightly better than the box model fits. The $\beta(z)$ profiles from both fitting methods are very similar suggesting that the real-space structure from the box model fits is reasonable

Note: The difference in the $\beta(z)$ of the subphase is due to the small addition of H₂O used for solvating the protein prior to incubation with the monolayer.

Table 1-1:
Box Model Fitting Scattering Length Densities for Monolayers on D₂O[#]

Region	DPPE: GM ₁ Monolayer			with CTB ₅			with CTAB ₅		
	Z (Å)	$\beta(z)$ x10 ⁻⁶	σ (Å) [§]	Z (Å)	$\beta(z)$ x10 ⁻⁶	σ (Å)	Z (Å)	$\beta(z)$ x10 ⁻⁶	σ (Å)
Lipid Tail	17.8 ±2	6.0 ±0.1	4 ±1	17.8*	5.8	4*	17.8 *	5.8	4*
Headgroup	7.5	4.5	3	7.5*	4.4	3*	7.5*	4.3	3*
GM ₁	13.5	5.5	3	11.7	5.0	3*	11.2	5.0	3*
CTB ₅				25	4.0	3	25*	4.0	3*
CTAB ₅							36.3	5.5	3
Subphase [‡]		6.3	3		6.1*	3*		6.1*	5
Area Expansion with protein	N/A			8±5%			8±5%		

[#] χ^2 values were between 1.7 and 2.4 for box model fits reported in this table.

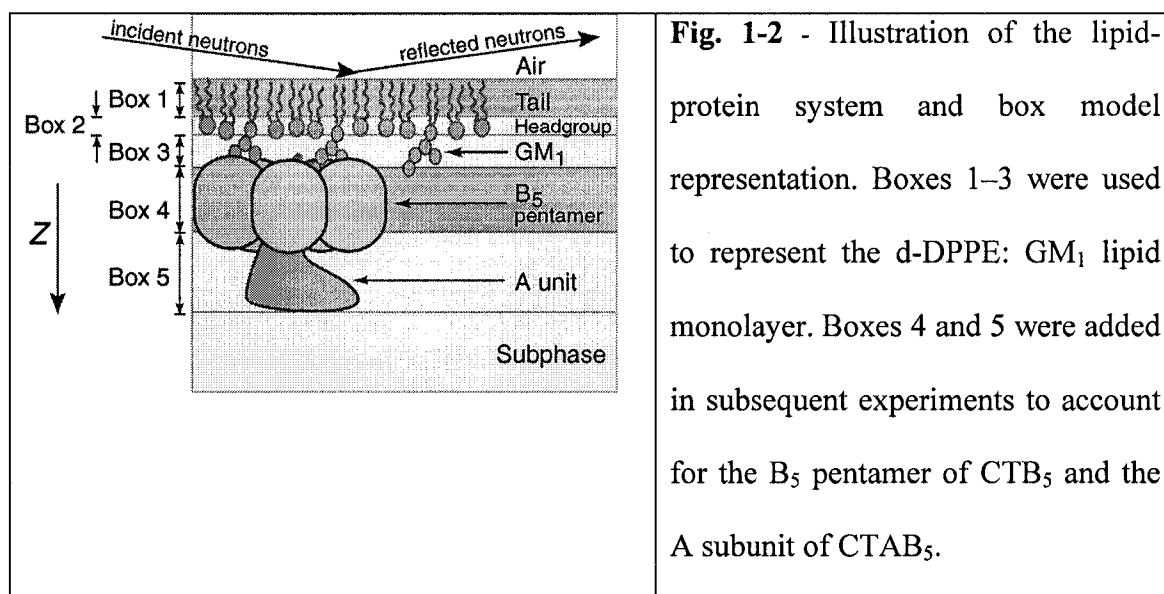
^{*}The difference in the $\beta(z)$ of the subphase is due to the small addition of H₂O used for solvating the protein prior to incubation with the monolayer.

[§]Because our Q_z range was limited to 0.24Å⁻¹, fitted parameters were not very sensitive to small changes in roughness. A minimum roughness of 3Å was assumed due to capillary waves [21].

^{*}Parameters that were fixed based on monolayer profile and not allowed to vary during the fitting procedure for CTAB₅ and CTB₅.

As shown in Fig. 1-1A, the box models fit well to the experimental reflectivity profiles in all three cases. In modeling the neutron scattering data, three boxes were used to account for structural features of the 80:20 d-DPPE:GM₁ lipid monolayer. The length and scattering length density of these boxes were based on the chemical units of the constituent molecules as shown in Fig. 1-2, e.g., one box for the lipid tail region, one for the predominately PE headgroup region, and a third box for the oligosaccharide region. Three boxes were required to reproduce the extension of the oligosaccharide groups away from the lipid layer into the water subphase. A two-box model, where the lipid headgroup and oligosaccharide regions were combined, yielded poorer fits to the NR profiles and

higher χ^2 values. The extension of the oligosaccharide group is consistent with previous x-ray scattering studies [22]. In the case of CTB₅, a fourth box was added to account for the protein layer, while two boxes were required for CTAB₅, one for the B pentamer and one for the A subunit. Values marked with an asterisk in **Table 1-1** identify parameters that were held constant during the box model fitting process to reduce the number of parameters.



In the box model fits for the lipid monolayer, regions for the tail, headgroup, and saccharide can each be clearly distinguished. From simple isotherm analysis at a surface pressure of 20mN/m the average area per lipid molecule, *Area*, is $45 \pm 3 \text{ \AA}^2$ for d-DPPE:GM₁ at a ratio of 80:20 mole %. The expected thickness can be calculated from the number of CH₂ groups, *n*, and their volume using the following equation [23].

$$T = [2(26.9 \times n) \text{ \AA}^3 / \text{Area}]^{1/2} = 17.9 \pm 1 \text{ \AA}$$

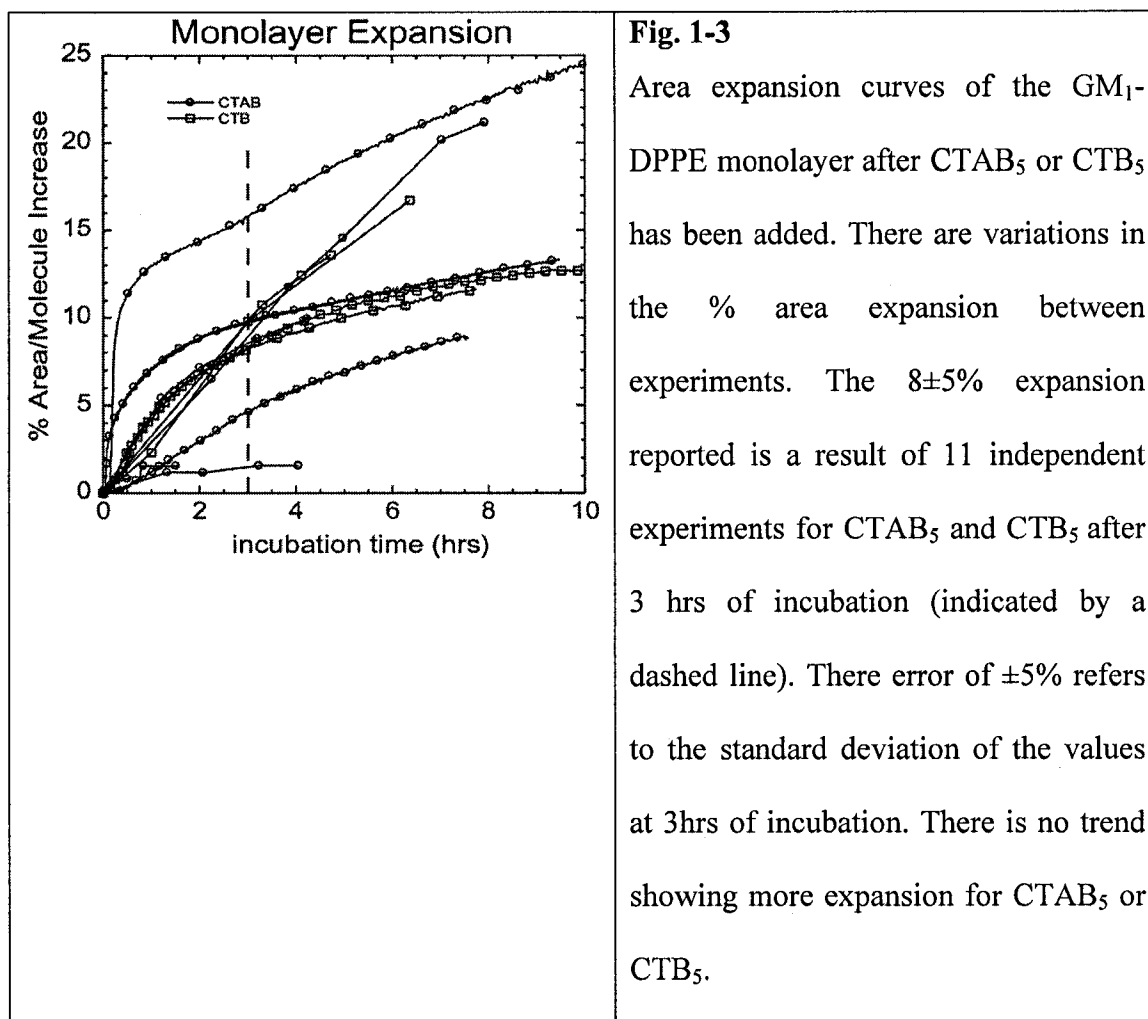
Both the $\beta(z) = 6.0 \times 10^{-6} \text{ \AA}^2$ for the tail region and thickness, $L = 17.8 \pm 2 \text{ \AA}$, match well to theoretical predictions for this packing density. Similarly, the thickness of the lipid

headgroup region, 7.5Å, and extension of the oligosaccharide groups, 13.5Å, match well to those previously reported [22, 24, 25].

When CTB₅ or CTAB₅ binds, it can be seen that the structure of the lipid portion of the monolayer is not significantly altered. From pressure area isotherm measurements under constant pressure conditions, toxin binding results in a small expansion of the monolayer commensurate with a decrease in lipid packing density. As a result of this expansion, there is more than one possible outcome. The thickness of the lipid tail region may decrease while the scattering length density remains constant, the scattering length density for the region may decrease while the thickness of the tail region remains constant, or some combination of both. We chose to hold the length of the tail region constant to reduce the number of fitting parameters based on the cubic beta spline fitting profiles. However, similar χ^2 values were obtained in box model fittings if the scattering length density was kept constant and the length was allowed to vary. Importantly, changes in the tail region of these two models had no effect on the B₅ and A regions of the toxin. Due to the invariance on the toxin portion of the model and the cubic beta spline fitting results, we chose to constrain the length of the tail region and allow the scattering length density to vary. Neutron reflectivity measurements alone cannot distinguish between these models due to the loss of phase information. With these constraints, the scattering length density of the lipid tails decreased slightly, 3%. Importantly, comparable area expansions of 8±5% are observed for either CTB₅ or CTAB₅ binding (results shown in Fig. 1-3). Due to large variation within the monolayer expansion data, there is no sufficient trend showing a difference between the effects of CTAB₅ and CTB₅ binding on the area per molecule of the monolayer. Because the

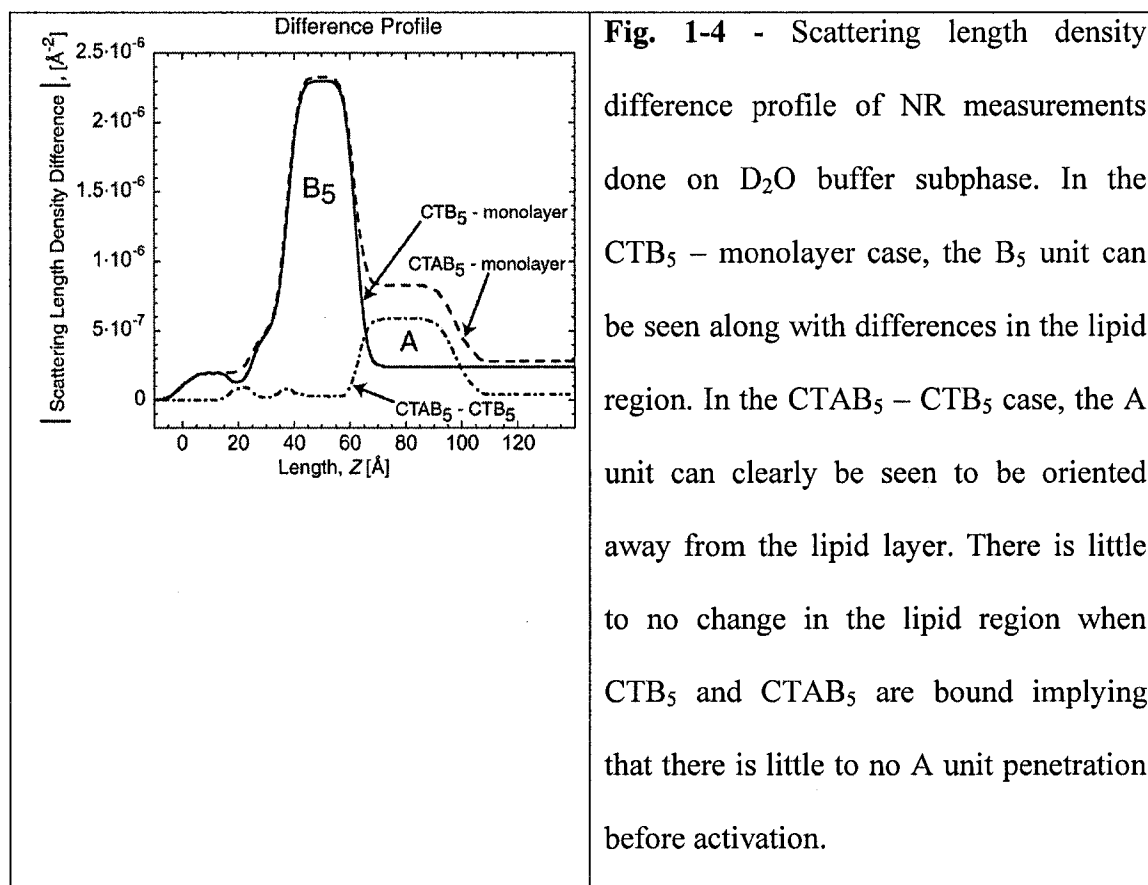
amount of area increase is the same regardless of the presence of the A subunit, these measurements demonstrate that A subunit penetration is not responsible for the area increase. Monte Carlo simulations (described later) suggest simple geometrical constraints imposed by toxin binding are responsible for the observed monolayer expansion. This hypothesis is also consistent with the calculated scattering length density profiles obtained with either box model or cubic beta spline fitting. The $\beta(z)$ of the protein is approximately $2 \times 10^{-6} \text{ \AA}^{-2}$ compared to $6 \times 10^{-6} \text{ \AA}^{-2}$ $\beta(z)$ for the deuterated lipid tails. A significant decrease in lipid tail $\beta(z)$ would be expected if protein penetrated the layer because the $\beta(z)$ for the protein is significantly less than that of the deuterated lipid tails. Another detail that does not support partial A subunit insertion is that the B₅ pentamer of CTAB₅ is 11 Å away from the lipid head group region. In other words, a distinct GM₁ saccharide region is still present.¹ The decrease in the thickness of the GM₁ saccharide region from 13.5 to 11.3 ± 2 Å when toxin is bound is consistent with the partial insertion of GM₁ oligosaccharides into the B₅ pentamer binding sites.

¹ Preliminary studies (results under preparation) show a complete collapse of the GM₁ saccharide region when the toxin is enzymatically activated bringing it directly into contact with the lipid layer.



Our NR results with CTAB₅ show that the A subunit is clearly facing away from the lipid layer and the majority of the subunit is below the B pentamer. This finding is consistent with previous electron microscopy, impedance spectroscopy, and surface plasmon resonance experiments [8, 11]. This positioning of the A unit further implies that the A unit may travel through the central pore of B₅ pentamer when the toxin is activated. In electron microscopy difference maps, approximately 60% of the A unit was missing after enzymatic activation. It was hypothesized that this unaccounted mass was embedded in the hydrophobic interior of the lipid membrane, inaccessible to the negative stain [8].

However, these measurements also implied that the A subunit penetrated the membrane before activation. Our studies using NR are not consistent with these finding and showed no difference in lipid structure between bound CTB₅ and CTAB₅. **Fig. 1-4** shows the fitted $\beta(z)$ profiles as difference profiles between the monolayer with and without toxin bound. The A unit orientation away from the monolayer is obvious from the difference profile between CTAB₅ and CTB₅. Conversely, the lipid region remains the same when either CTB₅ or CTAB₅ bind indicating that the A unit does not penetrate into the lipid monolayer before the toxin is enzymatically activated. A similar difference profile is obtained for CTB₅ and the monolayer. The B₅ unit can clearly be seen attached to the monolayer with small differences for the lipid region.



Reflectivity profiles from experiments conducted on H₂O subphase are shown in **Fig. 1-5** including box model fits and $\beta(z)$ profiles. Parameters used are listed in **Table 1-2**. The length scales of the lipid tail, lipid head group and CTB₅ (Box 4) components were held constant based on the D₂O fits and only the $\beta(z)$ of each region was allowed to change. Due to hydration, deuterium-hydrogen exchange, and the considerable difference between the $\beta(z)$ of D₂O ($6.33 \times 10^{-6} \text{ \AA}^{-2}$) and H₂O ($-5.6 \times 10^{-7} \text{ \AA}^{-2}$), there are significant differences in the $\beta(z)$ of all regions except the tails when comparing the D₂O and H₂O models. Length scales of the GM₁ saccharide region and the CTAB₅ (Box 5) region were slightly different due to less contrast between all layers involving H₂O hydration. This is because the $\beta(z)$ of the GM₁ saccharide and the protein are similar to that of H₂O. Importantly, the model obtained for D₂O and H₂O subphase are consistent with only minor variations. This consistency further supports that the models used in both cases are accurate.

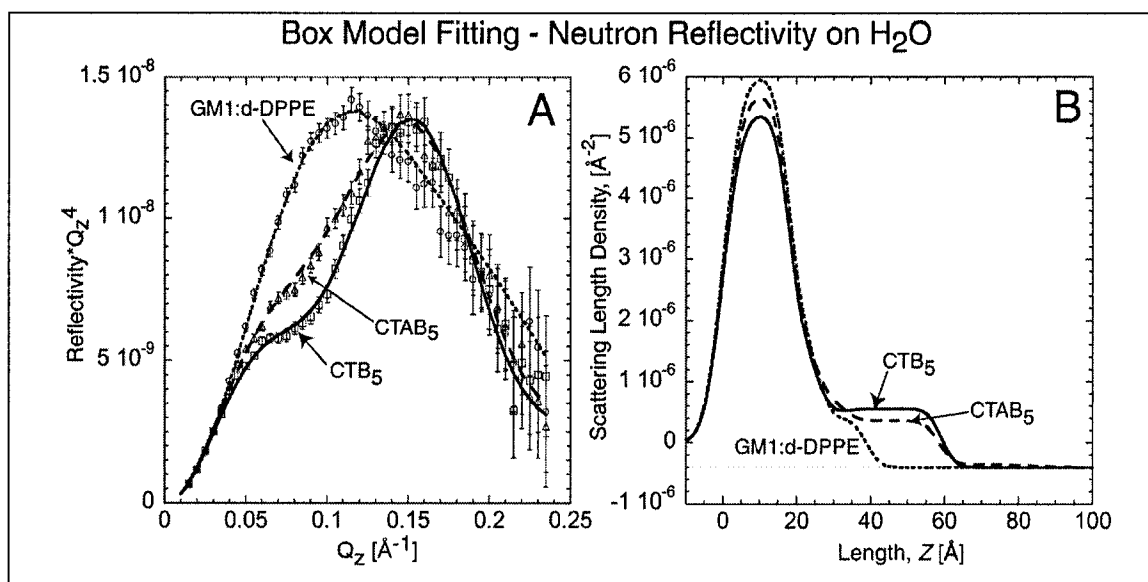


Fig. 1-5 - Neutron reflectivity with H₂O as the subphase instead of D₂O. **A** – Neutron reflectivity of the monolayer, monolayer with bound CTAB₅, and monolayer with bound CTB₅. Solid and dashed lines indicate the fit corresponding to the profile in **B**. Points with error bars correspond to measured data. **B** – Scattering Length Density Profile of fits shown in **A** obtained by box model fitting methods. The same features of lipid tails, lipid heads, and the B₅ subunit can be seen. The A unit of CTAB₅ is not very visible due to small contrast between the scattering length density of H₂O and the A unit layer. These results are consistent with that of NR done on D₂O. The difference in $\beta(z)$ of the lipid tail region for bound CTAB₅ and CTB₅ is most likely due to different protein coverage. The increased amount on CTB₅ coverage (indicated by a larger $\beta(z)$ for box4) is responsible for a larger decrease in lipid tail $\beta(z)$ due to a larger increase in area per molecule of the lipid layer

Table 1-2:
Box Model Fitting Scattering Length Densities for Monolayers on H₂O[#]

Region	DPPE:GM ₁ Monolayer			with CTB ₅			with CTAB ₅		
	Z (Å)	$\beta(z)$ x10 ⁻⁶	σ (Å) [§]	Z (Å)	$\beta(z)$ x10 ⁻⁶	σ (Å)	Z (Å)	$\beta(z)$ x10 ⁻⁶	σ (Å)
Lipid Tail	17.8*	6.0	4	17.8*	5.4	4*	17.8*	5.7	4*
Headgroup		±0.1	±1*						
GM ₁	7.5*	2.0	3*	7.5*	1.7	3*	7.5*	1.8	3*
CTB ₅	13.5*	0.4	3*	8.8	0.5	3*	8.1	0.68	3*
CTAB ₅				25*	0.56	3*	25*	0.36	3*
Subphase		-0.4	3*		-0.4*	3*	25	-0.35	3
								-0.4*	5

[#] χ^2 values were between 0.75 and 1.02 for box model fits reported in this table.

[§]Because our Q_z range was limited to 0.24Å^{-1} , fitted parameters were not very sensitive to small changes in roughness. Due to capillary waves, a minimum roughness of 3Å was assumed[21].

*Parameters that were fixed and not allowed to vary during the fitting procedure.

To assess the effects of CTAB₅ binding as a function of time, we scanned the same monolayer with bound CTAB₅ five consecutive times (Fig. 1-6). It can be seen that there are no significant changes and that toxin binding has stabilized after 3 hours of incubation. Studies done using ellipsometry showed CTB₅ adsorption to start immediately after injection and to be completed after one hour of incubation [6].

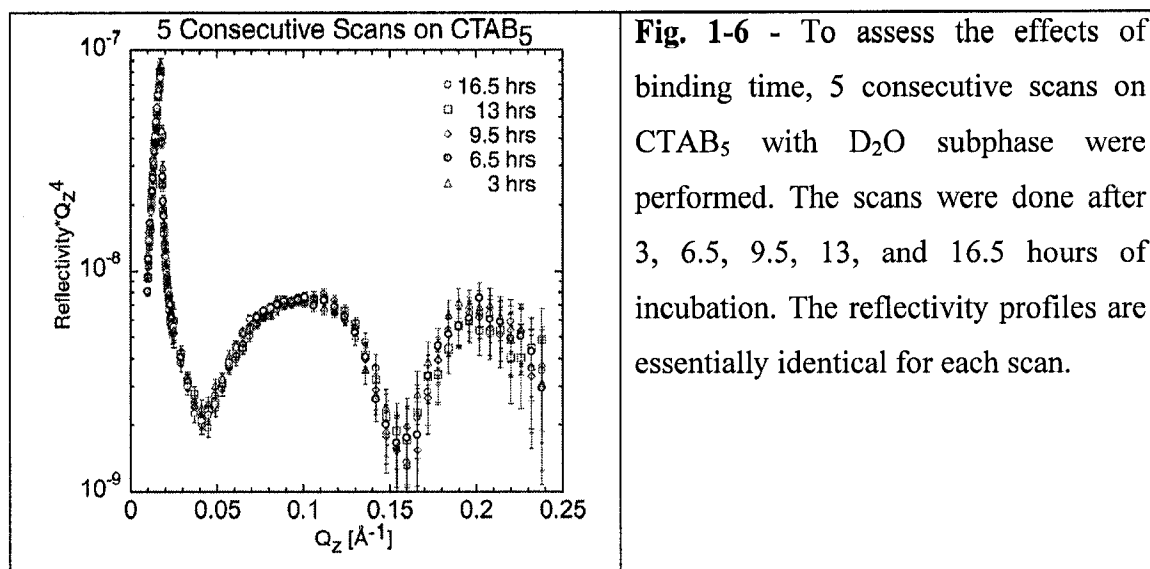


Fig. 1-6 - To assess the effects of binding time, 5 consecutive scans on CTAB₅ with D₂O subphase were performed. The scans were done after 3, 6.5, 9.5, 13, and 16.5 hours of incubation. The reflectivity profiles are essentially identical for each scan.

The individual atom scattering lengths for the 515 amino acids (103 residues per B subunit) which make up CTB₅ plus 204 water molecules and the molecular volume ($V=92030 \text{ \AA}^3$ calc) obtained from crystallographic data were used to calculate the scattering length density of CTB₅ [3]. Due to hydrogen-deuterium exchange and hydration changes, the $\beta(z)$ of CTB₅ in D₂O will be different than the $\beta(z)$ of CTB₅ in H₂O. A 1-dimensional NMR spectrum was run on a CTB₅ sample to determine the percentage of hydrogen exchange with deuterium. NMR analysis showed that $5 \pm 3\%$ of the total hydrogen exchanged on the CTB₅ molecule when dissolved in D₂O during an hourly time scale. Amide hydrogen on the interior of the protein and hydrogen involved in H-bonds will eventually exchange but on a time scale of days or even months. This exchange percentage was used to calculate the expected $\beta(z)$ of the CTB₅ molecule in D₂O and used to calculate the amount of toxin bound to the monolayer. The % coverage of CTB₅ was calculated to be $51 \pm 2\%$ for the D₂O case (5% hydrogen-deuterium exchange) and $51 \pm 2\%$ for the H₂O case using the following equation.

$$\beta(z)_{\text{measured}} = (1-X)(\beta(z)_{\text{subphase}}) + 0.953^{\&}(X)(^{\S}\beta(z)_{\text{CTB5}}) + 0.047^{\&}(X)(\beta(z)_{\text{subphase in pore}})$$

(Where X = % coverage of CTB₅, $\beta(z)_{\text{D2O}} = 6.1\text{e-}06 \text{ \AA}^{-2}$, $\beta(z)_{\text{H2O}} = -0.4\text{e-}06 \text{ \AA}^{-2}$, $\beta(z)_{\text{CTB5,D2O}} = 1.8\text{e-}06 \text{ \AA}^{-2}$, and $\beta(z)_{\text{CTB5,H2O}} = 1.6\text{e-}06 \text{ \AA}^{-2}$).

[&]Values obtained from the ratio of CTB₅ volume (92030 \AA^3) to central pore volume (4580 \AA^3).

[§]The scattering length of each atom was obtained from the NIST website <http://www.ncnr.nist.gov/resources/n-lengths> (C = 6.646fm, O = 5.803fm, N = 9.36fm, S = 2.85fm, H = -3.74fm, D = 6.671).

Finally, Monte Carlo simulations were performed on the lipid-cholera system to predict the amount of area expansion due to toxin binding [26]. All simulations assumed no protein insertion and calculated lipid packing using two-dimensional lipid layers at constant pressure. Hard disks were used to represent each lipid, GM₁ and DPPE, as shown in **Fig. 1-7B**. The Monte Carlo moves employed were standard translational moves, area changing and particle identity swap [27-29]. The simulations were performed on 200 GM₁ molecules and 800 DPPE molecules held within a two-dimensional square box. Pure DPPE at close packing has an area per molecule of 45 \AA^2 whereas monolayers of pure GM₁ attain close packing at 65 \AA^2 . However, GM₁ molecules at low to intermediate densities in mixed DPPE: GM₁ monolayers (up to 20 molar %) do not strongly change the overall area per molecule [22]. Therefore, GM₁ was modeled to be a hard disk with an area of 40 \AA^2 (this value was approximated from the

alkyl tail structure of GM₁) in the DPPE layer coupled to a 65 Å² disk below it (**Fig. 1-7B**) to represent the bulky saccharide headgroup. To imitate cholera binding, 55 GM₁ molecules were fixed in groups of pentagonal shapes to mimic the binding site positions of 11 CTB₅ molecules. The side length of each pentagon was 29.6 Å based on the distance between Trp88 residues within the binding site of each B unit of the CTB₅ pentamer [3]. The result of these simulations (**Fig. 1-7A**) showed a 7% increase in lipid area per molecule at a pressure of 20 mN/m solely due to packing inefficiencies caused by constraining GM₁ lipids at the cholera binding sites. **Fig. 1-8** shows an illustration describing how fixing GM₁ molecules can disturb the lipid packing efficiency. This outcome is consistent with our measured results for both CTB₅ and CTAB₅ suggesting that no protein penetrates into the monolayer before the toxin is activated. This is in contrast to previous results obtained by electron microscopy. Monte Carlo simulations also showed similar decreases in lipid packing efficiency when GM₁ lipids were constrained at random positions indicating that exact pentagonal geometries are not required for monolayer expansion.

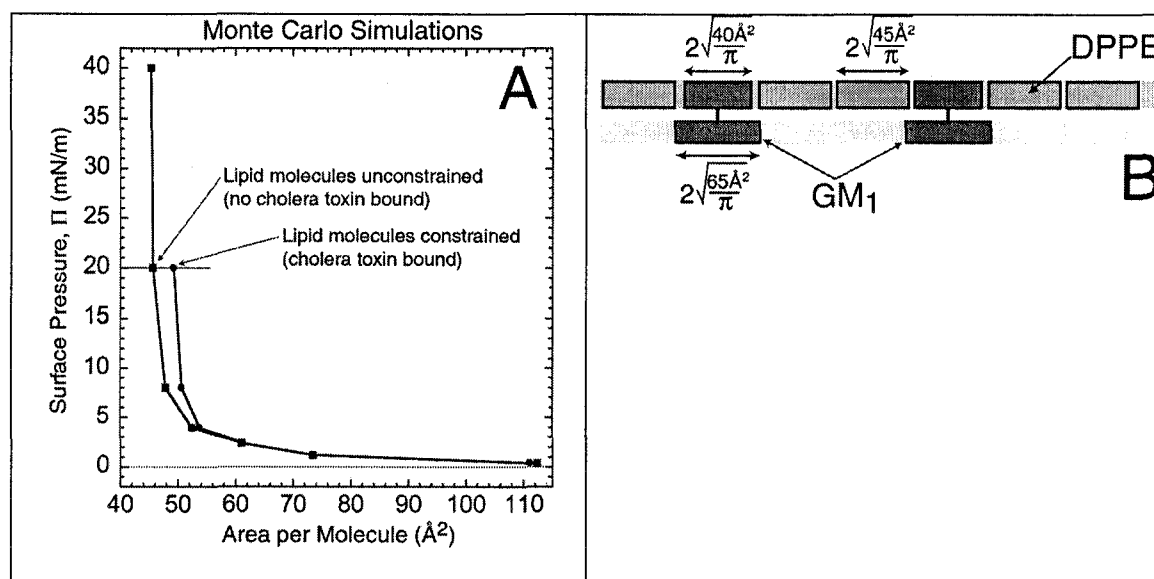
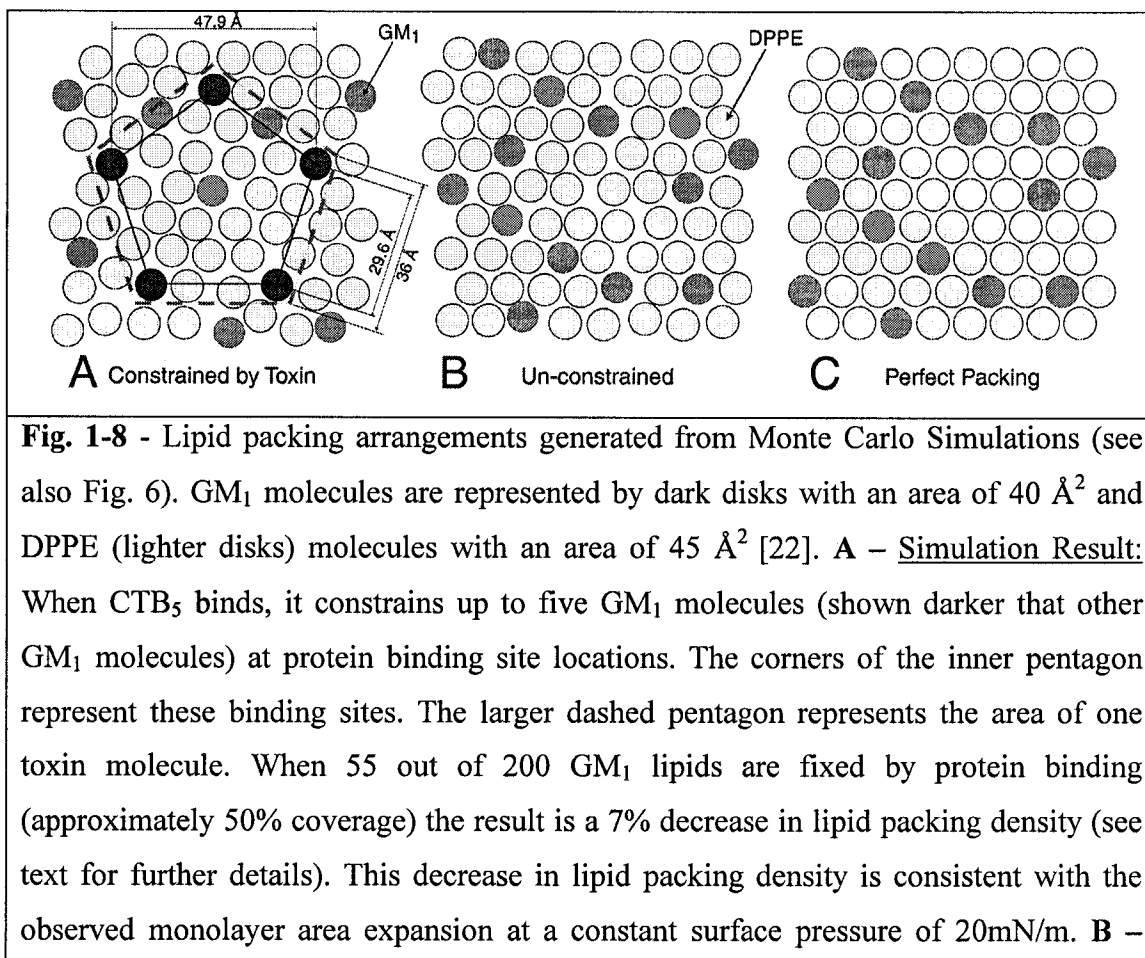


Fig. 1-7

A – Π -A isotherm generated from computer simulations. The area per molecule increases by 7% at 20mN/m due to lipid packing inefficiencies imposed by the pentagonal fixing of GM₁ lipids when CTB₅ or CTAB₅ bind. The surface pressures of the simulations have been rescaled to match results obtained from experimental isotherms of a monolayer with no bound toxin. **Fig. 1-8** shows an illustration demonstrating lipid packing under constrained and unconstrained conditions.

B – Description of the 2D, coupled Monte Carlo simulation model used for mixed DPPE: GM₁ monolayers.



Simulation Result: Shows an 80:20 DPPE: GM₁ monolayer at 20mN/m in the absence of protein binding (no constraints). C – Shows perfect packing of the monolayer for reference.

Conclusions

Using neutron reflectivity, we have characterized the structure of lipid monolayers presenting ganglioside GM₁ before and during the binding of cholera toxin (CTAB₅) or its B subunit (CTB₅). Structural parameters such as the density and thickness of the lipid layer, extension of the GM₁ oligosaccharide headgroup, orientation and position of the protein upon binding were reported. Upon protein binding, the density of the lipid layer decreases slightly, consistent with geometrical constraints imposed by multivalent binding of GM₁ to the toxin. The A subunit of the whole toxin is clearly located below the B pentameric ring, away from the monolayer, and does not penetrate into the lipid layer prior to enzymatic cleavage. Though the structure of the lipid layer is not significantly altered, neutron reflectivity and Monte Carlo simulation results support that geometrical constraints imposed by toxin binding lead to a decrease in lipid packing density. We hypothesize that this decrease in packing efficiency increases the amount of hydrophobic tail region exposed to the subphase and hence to the protein. After cleavage and toxin activation, the A1 unit is held in proximity to the interior of the membrane. Possible changes in protein conformation after activation may lead to further lipid perturbation and A1 membrane penetration.

Chapter 2: Cholera Toxin Assault on Lipid Membranes Containing Ganglioside GM1: An X-ray Reflectivity and Grazing Incidence Diffraction Study at the Air-Water Interface

Chapter Abstract

Cholera toxin is highly efficient in taking over host organisms. To reap its destructive effects on the cell, cholera toxin must bind to and infiltrate the cellular membrane, a specialized and controlled barrier. The mechanism by which cholera toxin crosses the membrane remains unresolved. Our studies using x-ray reflectivity and grazing incidence diffraction provide clues that membrane perturbation caused by cholera toxin's binding unit can initiate uptake into the cell and support the important role of low endosomal pH in the infection pathway. Our findings suggest that the B₅ pentamer plays a more active role in the membrane penetration mechanism than solely binding cholera toxin to its cell surface receptor.

Introduction

Many bacterial toxins bind to and gain entrance to target cells through specific interactions with membrane components. One such example is cholera toxin (CTAB₅), a pathologically active agent secreted by the bacterium *Vibrio cholerae* [1]. The toxin has an AB₅ arrangement of subunits. Five identical B subunits (CTB₅), each composed of 103 amino acids, form a pentameric ring with a vertical height of 32Å and a radius of 31Å [2, 3]. CTB₅ is responsible for binding the toxin to its cell-surface receptor, with highest affinity to ganglioside GM₁. The A-unit is a disulfide-linked dimer composed of an A1 and A2-subunit that is aligned through the pentameric ring "doughnut hole" of the B₅ subunit. After to binding to intestinal cells, CTAB₅ travels from the plasma

membrane to the endoplasmic reticulum (ER) [30]. It has been proposed that proteolytic cleavage (between residues 192 and 194) and reduction of the disulfide bond (cys187 = cys199) activates the A1 peptide enabling it to cross the cell membrane [4]. On the cytoplasmic side of the plasma membrane, the A1 peptide interacts with integral membrane proteins, disrupting their normal function, resulting in a large efflux of water and ions from the cell (severe diarrhea) [5]. Although much is known about the structure and catalytic activity of cholera toxin, the mechanism by which cholera toxin crosses the plasma membrane remains unresolved.

Because of its detrimental effect on health, cholera toxin has been the focus of many studies. Several different methods have shown that the B₅ portion of the toxin is responsible for binding to lipid membranes containing GM₁. Experiments involving electron microscopy, ellipsometry, and flow cytometry indicate that cholera toxin has minimal non-specific adsorption to lipid membranes in the absence of ganglioside lipids [6-8]. Because binding is multivalent (one GM₁ per B monomer), off-rates of the toxin are slow. If the concentration of GM₁ receptor is large enough, it is possible for macroscopic, two-dimensional cholera toxin crystals to be assembled with high coverage [6]. At the molecular level, AFM studies have shown that CTB₅ binds to GM₁ rich domains of lipid bilayers [9, 10]. Electron microscopy, impedance spectroscopy, and surface plasmon resonance have shown with reasonable confidence that the A unit faces away from the lipid layer when bound [8, 11]. We have confirmed this orientation with neutron reflectivity studies [31].

The high binding stability of CTB₅ may also be important for membrane penetration. Cholera toxin exhibits a highly conserved, exposed peptide loop (Glu51 –

Ile58) that faces the cell membrane [32]. Rodighiero and coworkers have recently demonstrated that mutation of His57 to Alanine produces a cholera toxin B-subunit variant that binds to GM₁ with high affinity but fails to induce toxicity. In wild type, H57 makes van der Waals contact with the terminal galactose of GM₁. Substitution of this residue removes this contact and suggests that stable formation of the full CTB₅-GM₁ complex is necessary for intercellular trafficking to the ER. Rodighiero *et al* propose that CT-H57A fails to induce toxicity because it dissociates from GM₁ before or after endocytosis.

It has also been proposed that cholera toxin is a cellular hijacker, using the natural transport mechanisms of the cell via a KDEL amino acid residue sequence at the C-terminal of the A2 subunit. This KDEL tail is tethered through the B₅ pore and is directly exposed to the membrane surface when cholera binds. The KDEL tail is a peptide sequence used for recognition by KDEL receptor located in the ER [33]. Haze and Read speculate that cholera toxin and other ADP-ribosylating toxins use the Sec61p retrotranslocation machinery, a cellular mechanism that transports misfolded proteins from the ER to the cytosol to be degraded.

Four independent experimental approaches are consistent with cholera toxin moving from the plasma membrane to the ER where the A1 subunit crosses the membrane [34]. After being released from the CTB₅-A2 molecule, the A1 peptide exhibits hydrophobic behavior which allows it to partition itself within the hydrophobic core of the membrane. However, only some membranes may be able to accept the A1 peptide. Thus, Golgi and ER membranes must exhibit unique lipid [35] and protein

structure permissive for membrane integration of the A1 peptide while plasma and endosome membranes may not.

To clarify, our studies show that cholera toxin may play an active role in initiating endocytosis through membrane perturbation events caused by the B₅ pentamer. In addition to binding and creating a site for membrane fusion, a crucial step of endocytosis, CTB₅ must remain attached to the membrane long enough to undergo endocytosis and survive trafficking to the ER. After cholera toxin has been engulfed by endocytosis, endosomes are known to lower pH to aid the degradation of cellular components such as lipids and proteins. Our results support the importance of low endosomal pH in the cholera toxin infection pathway.

Experimental Section

Materials

All lipid monolayers were composed of 80:20 mole % of DPPE: GM₁ [1, 2-Dipalmitoyl-*sn*-Glycero-3-Phosphoethanolamine: Galactosyl-N-Acetylgalactosaminyl (N-acetyl-neuraminyl) Galactosylglucosylceramide (GM₁ Ganglioside)]. GM₁ and DPPE were obtained from Avanti Polar Lipids and were used without further purification. Lipids were dissolved in chloroform: methanol 90:10 (~1.2mg/mL), mixed to obtain an 80:20 mole ratio, and deposited on an H₂O buffer subphase (pH=5 or pH=8). Buffer chemicals were purchased from Sigma and prepared using Millipore H₂O with 170 mM NaCl, 1.4 mM NaN₃, 0.3mM EDTA, 15mM Trizma-HCl (pH=5)/ Trizma-Base (pH=8). Cholera Toxin, CTAB₅, was purchased from BioMol Research Labs and CTB₅ was purchased from Sigma. Cholera toxin was solvated from powder with water to a

concentration of 1 mg/mL. Cholera was then injected into the subphase (under the monolayer) to a final concentration of ~ 4 mg/L and the subphase was continuously circulated by a peristaltic pump at the rate of ~ 8 ml/min. This procedure homogenized the concentration of the toxin throughout the volume of the trough (250 mL). Cholera toxin was allowed to incubate for 1 – 3 hours before scanning. Dithiothreitol (DT) was purchased from Sigma and injected into the subphase to a final concentration of ~ 4 mg/mL. Unless otherwise noted, the monolayer's molar composition, surface pressure of 20 mN/m, and temperature of 23°C were held constant throughout each experiment.

Grazing Incident X-Ray Diffraction

The theory of grazing incidence x-ray diffraction (GIXD) and x-ray reflectivity (XR) has been presented in great detail elsewhere [36] and only a short discussion will be given here. All synchrotron x-ray measurements were carried out using the liquid surface diffractometer at the BW1 (undulator) beam line at HASYLAB, DESY (Hamburg, Germany). A Langmuir trough equipped with a Wilhelmy balance for surface pressure measurements, a motorized barrier for surface pressure control, and temperature control was mounted on the diffractometer. The trough was enclosed in a sealed, helium-filled canister where the oxygen level was constantly monitored. The synchrotron x-ray beam was monochromated to a wavelength of $\lambda \sim 1.305$ Å by Laue reflection from a Be (200) monocrystal. By tilting the normal to the reflecting planes out of the horizontal plane, the monochromatic beam could be bent down to yield a glancing angle with the horizontal liquid surface. For the GIXD experiments, the x-ray beam was adjusted to strike the surface at an incident angle of 0.11° , which corresponds to the vertical momentum transfer vector $q_z = 0.85 q_c$, where $q_c = 0.02176$ Å⁻¹ is the critical scattering vector for

total external reflection. At this angle the incident wave is totally reflected, while the refracted wave becomes evanescent traveling along the liquid surface. Such a configuration maximizes surface sensitivity. The dimension of the incoming x-ray beam footprint on the liquid surface was approximately 2 mm X 50 mm. For x-ray reflectivity measurements, a set of slits was used to exclude diffuse scattered background around the reflected beam. These slits, along with a scintillation detector, were mounted on an elevator. The absolute reflectivity was derived by subtracting background followed by normalization to the incident beam flux. For in-plane diffraction measurements, a vertically placed Soller collimator giving a lateral resolution of $\Delta q_{xy} = 0.0075 \text{ \AA}^{-1}$ was placed before a vertical one-dimensional position sensitive detector (PSD) with vertical acceptance $0 < q_z < 1.2 \text{ \AA}^{-1}$, allowing Bragg rod measurements to be made.

In three-dimensional (3D) crystals, diffraction only takes place when the scattering vector, q , coincides with points of the reciprocal 3D lattice, giving rise to Bragg spots (h, k, l are the Miller indices). Strong diffraction from a set of crystal planes with an interplanar spacing d occurs only when the Bragg law is obeyed. In our two-dimensional (2D) systems and at surface pressures of interest, the monolayers are a mosaic of 2D crystals with random orientation about the direction normal to the subphase, and can therefore be described as 2D powders. Due to the lack of restriction on the scattering vector component q_z along the direction normal to the crystal, Bragg scattering from a 2D crystal extends as continuous Bragg rods through the reciprocal space [36].

The scattered intensity is measured by scanning over a range of horizontal scattering vectors $q_{xy} \sim (4\pi/\lambda) \sin(2\theta_{xy}/2)$, where $2\theta_{xy}$ is the angle between the incident

and diffracted beam. Bragg peaks are resolved in the q_{xy} -direction and obtained by integrating the scattered intensity over channels along the z -direction in the PSD. Conversely, the Bragg rod profiles are resolved in the q_z -direction and obtained by integrating the scattered intensity of a Bragg peak over each PSD channel. The angular positions of the Bragg peaks allow for the determination of the repeat distance d for the 2D lattice. From the line shapes of the peaks, it is possible to determine the 2D crystalline in-plane coherence length, L_{xy} (the average distance in the direction of the reciprocal lattice vector q_{xy} over which there is "near-perfect" crystallinity). The intensity distribution along the Bragg rod can be analyzed to determine the direction and magnitude of the molecular tilt, the out-of-plane coherence length L_c , and the magnitude of molecular motion or surface roughness of the crystallite (Debye-Waller factor).

X-ray Reflectivity

Reflectivity, R , is defined as the intensity ratio of x-rays specularly scattered from a surface relative to the incident x-ray beam intensity. When measured as a function of wave-vector transfer ($q_z = |\mathbf{k}_{out} - \mathbf{k}_{in}| = 4\pi \sin\alpha / \lambda$, where α is the angle of incidence and λ is the wavelength of the x-ray beam), the reflectivity curve contains information regarding the sample-normal profile of the in-plane average of the coherent electron densities. Detailed information on the electron density distribution in the direction normal to the interface, averaged laterally over both the ordered and disordered parts of the film, can be determined by modeling the deviation of the measured specular x-ray reflectivity from Fresnel's law for a perfect interface. Using a $\sim 1.305 \text{ \AA}$ wavelength x-ray beam, the reflectivity as a function of q_z values from 0.01 to 0.8 \AA^{-1} was determined with reasonable

statistics to values of $R \sim 10^{-10}$. Typical scanning times for this q_z range were 30 minutes. The reflected x-rays were counted using a NaI scintillation detector. The data was reduced and plotted as R/R_F versus the perpendicular scattering vector, q_z (the division by Fresnel reflectivity, R_F , increases the visibility of the reflectivity profile by accounting for a sharp q_z^{-4} decrease of the reflectivity due to the Fresnel's law). The error bars on the data represent the statistical errors in the measurements (standard deviation, σ_R). Analysis of the measured reflectivity curves was performed using a free form cubic beta spline fitting routine [19]. In this method, the electron density profile was parameterized using cubic splines. The coefficients in the series were determined by constrained nonlinear least-squares methods, in which the smoothest solution that agrees with the data was chosen.

Beam Damage

X-rays with a wavelength of 1.305 Å (9.5 keV) can cause significant beam damage to the monolayer/protein sample. Overexposure can “burn” the sample and cause a change in the real space structure over time. To mitigate damage to the film by x-rays, the sample was translated perpendicular to the beam and was only scanned once for all measurements reported. In addition to sample translation, repeat measurements were conducted a minimum of 3 times and averaged to minimize beam damage artifact. It should be noted that the authors spent two and a half years characterizing the effects of beam damage to the sample before conducting the experiments reported in this manuscript. To save space, this data is not presented here.

Results

Pressure – Area Isotherms

GM1 does not disturb lipid packing efficiency

Pressure–area isotherms for GM₁, DPPE, and their mixtures are shown in **Fig. 2-1a**. As can be seen in the 100% GM₁ isotherm, the large size of the GM₁ headgroup causes a non-zero surface pressure even at areas per molecule above 100 Å². This behavior is very typical for a fluid phase monolayer with a large bulky headgroup. A pure DPPE monolayer has a much more sharp pressure increase distinctive of a solid or gel phase monolayer. All DPPE: GM₁ lipid mixtures with 20% or less GM₁ content can be almost superimposed on the isotherm of pure DPPE. This indicates that GM₁ molecules, at a mole fraction of 20%, are incorporated into the DPPE matrix and do not disturb the packing of the DPPE molecules. No indication of domain formation, phase separation or non-homogeneous structuring within the mixed monolayer at the air–water interface at 20 mN/m was observed using fluorescence, *Brewster angle microscopy* (results not shown) or x-ray scattering methods [37].

Area Expansion Analysis

Toxin binding causes lipid packing inefficiencies

The binding of cholera toxin to the monolayer alters the lipid packing. At a constant surface pressure of 20 mN/m cholera toxin binding resulted in an increase in the area of the monolayer film. The relative increase in the area per lipid molecule as toxin binds at pH=5 is shown in **Fig. 2-1b**. Both CTB₅ and CTAB₅ were injected at t=0 sec, yielding similar increases in area upon protein binding. Toxin activation by the addition

of dithiothreitol (DT) dramatically amplifies the rate of area increase with CTAB₅ but not with CTB₅ (Control). This finding suggests that there is no A subunit penetration prior to enzymatic activation. Previously, we hypothesized and showed through Monte Carlo simulations that observed area expansion upon protein binding is due to packing inefficiencies caused by constraining GM₁ lipids at cholera's five binding sites [31, 38].

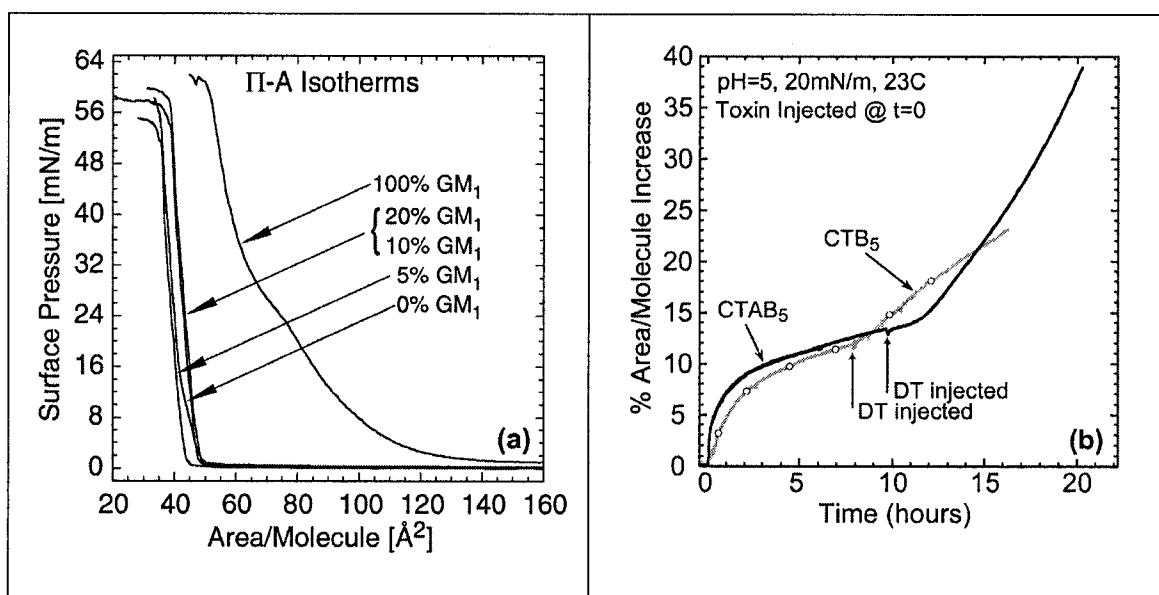


Figure 2-1: (a) Surface Pressure vs. Area Isotherms of various DPPE: GM₁ lipid mixtures. Up to a 20% mole fraction of GM₁ can be incorporated into the monolayer without a significant change to the isotherm. (b) Area expansion analysis at 20mN/m and pH=5 with injection of CTAB₅ and CTB₅ into the subphase at t=0 sec. The area expansion is similar for both proteins. After dithiothreitol (DT) is injected into the subphase and enzymatic cleavage is initiated, the rate of expansion is greatly increased for CTAB₅.

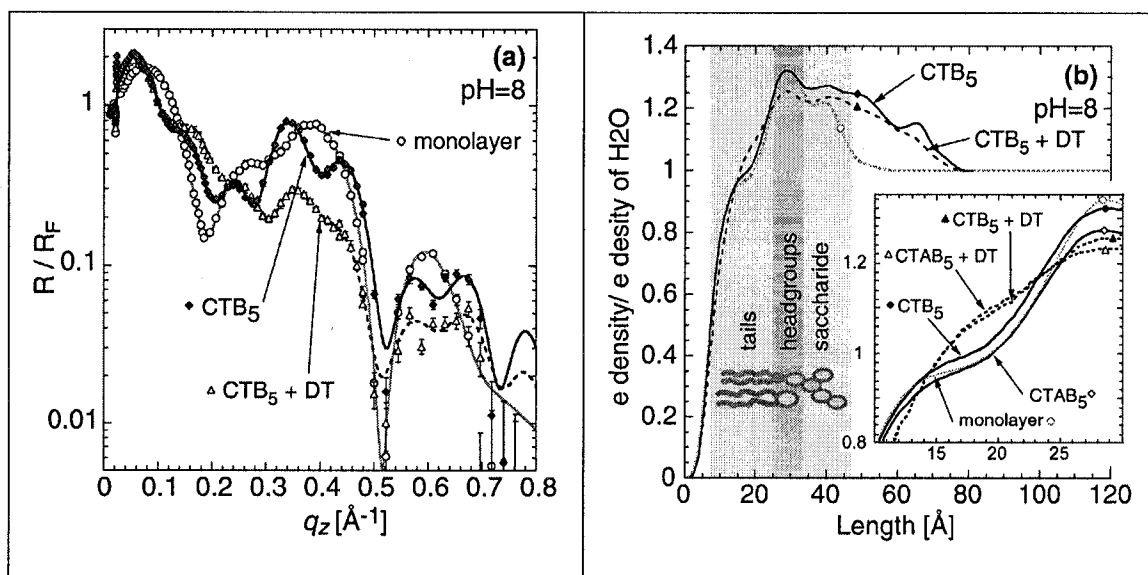
In earlier neutron reflectivity studies, we scanned a 80:20 DPPE: GM₁ monolayer with bound CTAB₅ consecutively over a 16 hour time period to monitor CTAB₅ binding as a function of time [31]. After 3 hours of incubation there were no significant changes in the film structure. Similarly, ellipsometry studies demonstrate CTB₅ adsorption starts immediately after injection and is complete about one hour after incubation [6]. When DT is injected onto the subphase and enzymatic cleavage is initiated, CTAB₅ has a larger percent increase on the area per molecule of the monolayer (**Fig 2-1b**). This is consistent with the A subunit being released and penetrating into the monolayer. Surprisingly, a noticeable increase in area was also observed with CTB₅. When DT was added to the subphase with no protein present (control), the area expansion of the monolayer was insignificant (1%). This may indicate that the CTB₅ pentamer plays a larger role in the membrane penetration mechanism rather solely binding to the membrane.

Reflectivity Analysis (pH=8)

Reflectivity measurements of the lipid-toxin system at the air-water interface enabled the average electron density profile normal to the interface to be determined. The experimentally measured reflectivity profiles at pH=8 for (1) the mixed DPPE: GM₁ monolayer, (2) the monolayer with CTB₅, and (3) the monolayer with CTB₅ + DT on an H₂O/buffer subphase are shown in **Fig. 2-2a**. **Figure 2-2c** shows the experimentally measured reflectivity profiles for (1) the mixed DPPE: GM₁ monolayer, (2) the monolayer with CTAB₅, and (3) the monolayer with CTAB₅ + DT on an H₂O/buffer subphase. A few qualitative observations can be made directly from the reflectivity profiles. When either CTB₅ or CTAB₅ binds to the monolayer, there is a shift in the first interference maximum ($q_z \sim 0.08 \text{ \AA}^{-1}$) to smaller q_z values. This is a result of an increase

in thickness at the interface as protein binds and forms a protein monolayer under the lipid monolayer. There is also a large difference to the reflectivity profile before and after activation for both CTB₅ and CTAB₅.

More quantitative details can be obtained using cubic beta spline fits to the data to obtain real space structures. The corresponding electron density profiles, $e^-(z)$, obtained from the cubic beta spline fits (solid and dashed curves) are shown in **Fig. 2-2b and 2-2d**. The presence of both CTB₅ and CTAB₅ can clearly be seen by a large electron density increase extending into the subphase from the GM₁ headgroup. In the case of CTAB₅, the B₅ pentamer can be distinguish from the A subunit which extends further into the subphase $\sim 40\text{\AA}$ for CTB₅ and $\sim 70\text{\AA}$ for CTAB₅. When CTB₅ or CTAB₅ binds, there is little change in the lipid monolayer density distribution. However, with activation (CTB₅+DT and CTAB₅+DT) there is a significant increase in density to the lipid tails and a decrease in intensity of the lipid headgroup region. In other words, CTB₅ and CTAB₅ cause the same effect on the lipid monolayer at pH=8. This result is not similar to pH=5.



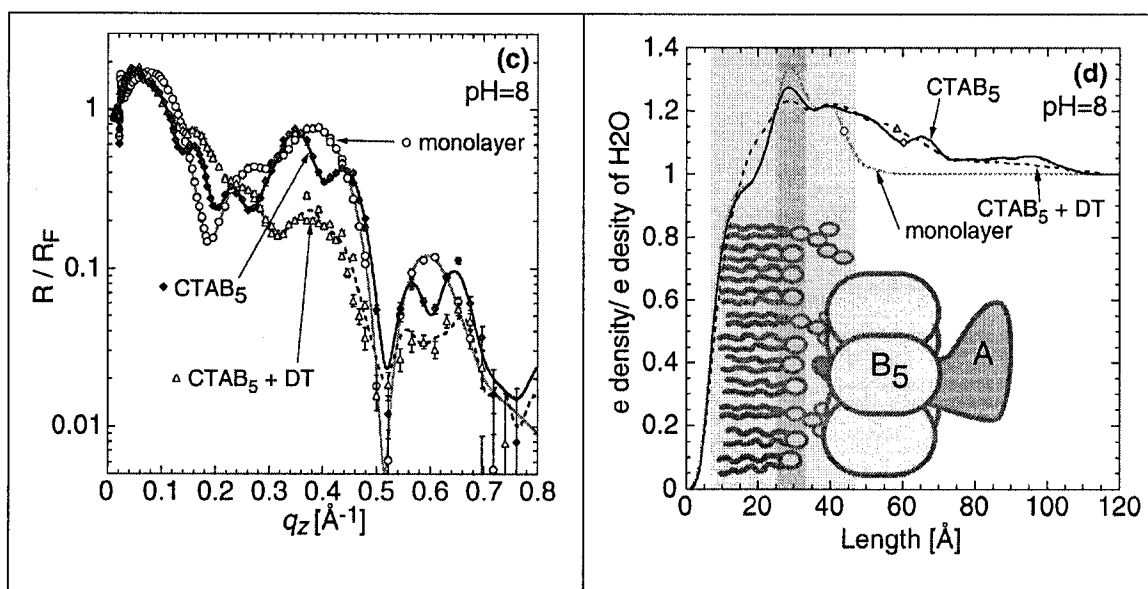


Figure 2-2: X-ray reflectivity results at pH=8. For clarity, we have separated the experiment set into two parts. (a) and (b) are for a DPPE: GM₁ monolayer with bound CTB₅ (before and after activation with dithiothreitol (DT)). (c) and (d) are for a DPPE: GM₁ monolayer with bound CTAB₅ (before and after activation with DT). (a) and (c) show the measured reflectivity plotted as R/R_{Fresnel} versus q_z . Error bars for the reflectivity data represent statistical errors in these measurements. Measured data is represented as symbols and lines (solid and dashed) represent fits corresponding to the electron density profiles shown in (b) and (d). In the electron density profiles the binding of both CTB₅ and CTAB₅ can clearly be seen by a large electron density increase extending into the subphase from the GM₁ headgroup. Binding of protein results in a decrease in electron density in the headgroup region and a small increase in density of the lipid tails. As discussed later, this is a different from what is observed at pH=5. After activation with DT, there is a large density increase of the lipid tails signifying that protein is entering the monolayer region. In other words, CTB₅ and CTAB₅ (before and after activation) cause the same effect on the lipid monolayer at pH=8. This result is not similar to results at pH=5. Note: the electron density of water $0.334 e^-/\text{\AA}^{-3}$

Protein is entering the monolayer region

When protein binds, there is a decrease in lipid thickness as expected due to the increase in area per molecule. CTB₅+DT and CTAB₅+DT cause a large increase in density of the hydrocarbon tail region suggesting that protein is entering this region. Again, this increase in tail electron density is not seen when CTAB₅ is bound and is relatively small when CTB₅ is bound. It is important to note that the density of the lipid tails is expected to decrease (or stay the same with a commensurate decrease in tail thickness) because the area per molecule increases in all cases. The only possible way for the electron density of the tails to increase is to have electron density contribution from the toxin. No density change is observed in the tail region for monolayers (with no protein present) at 20, 30 and 45 mN/m (data not shown) or with addition of DT (control). As pressure is increased (decreased area per molecule), the constant tail density is balanced by an increase in tail thickness due to a decrease in molecular tilt of the lipids.

Activation causes a decreased amount of protein outside the monolayer

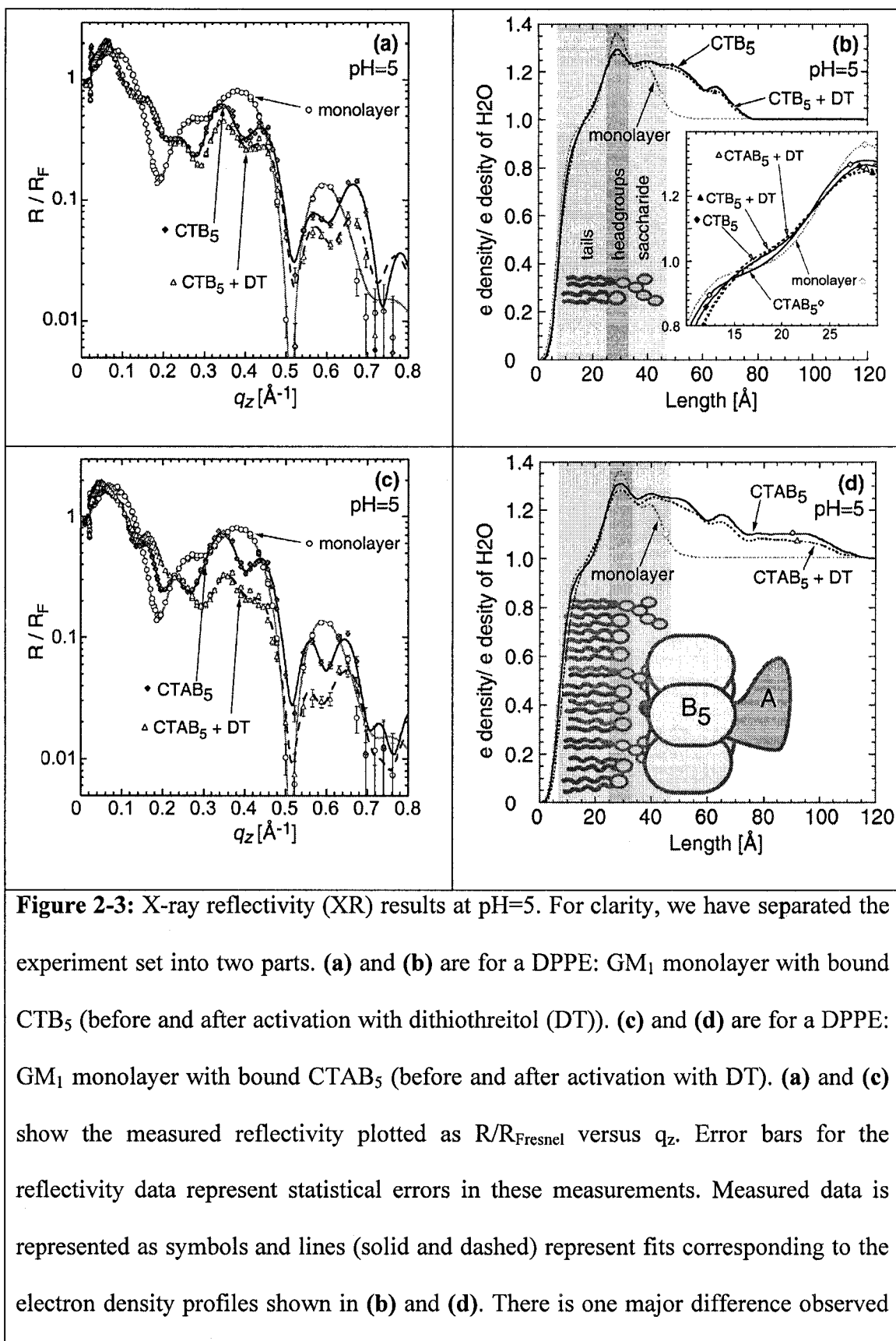
Similar to CTAB₅, CTAB₅+DT has a significant quantity of the A subunit facing away from the monolayer. This is unexpected since DT is supposed to cleave the A1 unit from the cholera molecule. However, there is a considerable decrease in the density of the A subunit after activation. We hypothesize that incubation with DT is only cleaving a portion of the CTAB₅ molecules. On the other hand, the amount of CTB₅ and CTAB₅ decreases after activation. This decrease is expected if protein is entering the monolayer region due to conservation of electron density.

Reflectivity Analysis (pH=5)

Low pH causes CTB₅ to perturb the monolayer

The experimentally measured reflectivity profiles at pH=5 for (1) the mixed DPPE: GM₁ monolayer, (2) the monolayer with CTB₅, and (3) the monolayer with CTB₅ + DT on an H₂O/buffer subphase are shown in **Fig. 2-3a**. **Figure 2-3c** shows the experimentally measured reflectivity profiles for (1) the mixed DPPE: GM₁ monolayer, (2) the monolayer with CTAB₅, and (3) the monolayer with CTAB₅ + DT on an H₂O/buffer subphase. Reflectivity at pH=5 shows one major difference from reflectivity results at pH=8. There is little qualitative difference between the reflectivity profiles of CTB₅ and CTB₅+DT. This can also be seen from the real space structures obtained from the cubic beta spline fits to the data.

Electron density profiles at pH=5 for CTB₅ and CTAB₅ are shown in **Fig. 2-3b** and **Fig. 2-3d** respectively. The monolayer region for bound CTAB₅ and CTAB₅+DT look very similar to the monolayer region at pH=8 where there is minimal perturbation to the monolayer before activation and a large increase in lipid tail density after activation. Conversely, CTB₅ behaves very differently at pH=5, causing significant effects on the monolayer before activation. In other words, CTB₅ and CTB₅+DT have similar electron density increases in the lipid tail region. These results are consistent between several independent scans. No CTAB₅ scans (4 independent scans) show significant perturbation (ie increase in tail density) to the monolayer before DT is added. All CTB₅ (3 independent) scans at pH=5 show an increase in the electron density of the lipid tails equivalent to CTB₅+DT.



when compared to XR results at pH=8. CTB₅ and CTB₅+DT have equivalent effect on the monolayer region. This similarity can be seen both in the measured reflectivity profiles **(a)** and the electron density profiles **(b)**. Electron density profiles were obtained by averaging between independent scans (4 for CTAB₅ and 3 for CTB₅) after aligning all head groups. Note: the electron density of water $0.334 e^{-}/\text{\AA}^3$

Summing up pH dependence, pH=5 causes CTB₅ to behave as if it is already activated. The absence of the A subunit (CTB₅) is similar to cleaving the A1 subunit from CTAB₅ (CTAB₅ + DT). It was previously believed that the mechanism of the B₅ pentamer portion of the cholera toxin molecule solely acts as the membrane-binding component. Membrane penetration of CTB₅ at low pH implies that the B₅ pentamer participates in a more active role of the membrane penetration mechanism. This further implies that low pH may be important for cholera intoxication. Previously, it has been shown that low pH causes CTB₅ and CTAB₅ to form ion channels in planar bilayer lipid membranes and suggest that the formation of the water pore of these channels is confined to the B-subunit of cholera toxin [39]. During endocytosis, an important cellular process that engulfs extra cellular material into the cell, the pH of the vesicle is lowered to aid protein degradation. Our reflectivity results suggest that this pH lowering step is important to the cholera's infection mechanism due to CTB₅ penetration into the lipid tails before being activated.

Lipid monolayer coverage of cholera toxin

Through reflectivity analysis, different quantities of protein coverage (%) can be observed between scans. This is shown in **Fig. 2-4a** for two cases of CTB₅ and CTAB₅ at

pH=5. The coverage ranges from approximately 50 – 65 % and can also be monitored by the percent increase in the area per molecule on the trough. The % coverage is calculated by the following equation:

$$e^-(z)^{\#}_{\text{measured}} = [1 - X][e^-(z)_{\text{subphase}}] + [X][(0.931^{\&})e^-(z)^{\S}_{\text{CTB}_5} + (0.069^{\&})e^-(z)_{\text{subphase in pore}}]$$

(Where $e^-(z)$ = electron density, X = % coverage of CTB₅, $e^-(z)_{\text{subphase}} = 0.334 e^-/\text{\AA}^{-3}$, $e^-(z)_{\text{CTB}_5} = 0.486 e^-/\text{\AA}^{-3}$).

[#] Measured electron density values were taken from both CTB₅ profiles in **Fig. 2-4a** at a length of ~50Å. 50% and 65% coverage corresponds to a measured electron densities of $0.405 e^-/\text{\AA}^{-3}$ and $0.425 e^-/\text{\AA}^{-3}$ respectively.

[&] Values obtained from the ratio of CTB₅ volume (66784\AA^3) to central pore volume (4580\AA^3). The volume of CTB₅ was approximated by a regular pentagon with sides of length 36Å and a height of 32Å. The central pore volume was approximated by a cylinder with a diameter of 13.5Å and a height of 32Å. The distances used were obtained from the 3D crystal structure.

[§] The theoretical electron density of CTB₅ was obtained by dividing the total number of electrons in CTB₅ by its volume (66784\AA^3).

There are small differences in the monolayer region when different amounts of protein are bound that are not sufficient to account for the different amounts of perturbation to the monolayer at different pH seen in **Fig. 2-2** and **Fig. 2-3**. We also explored the effects of DT on the monolayer. When no protein is present, DT had no

significant effect on area per molecule, electron density, or in-plane diffraction. This is shown by reflectivity and GIXD results in **Fig. 2-4b**. The electron density profiles of the monolayer before and after the addition of DT can be superimposed on each other. The inset of **Fig. 2-4b** shows no significant changes in the diffraction from the lipid tails when DT is present.

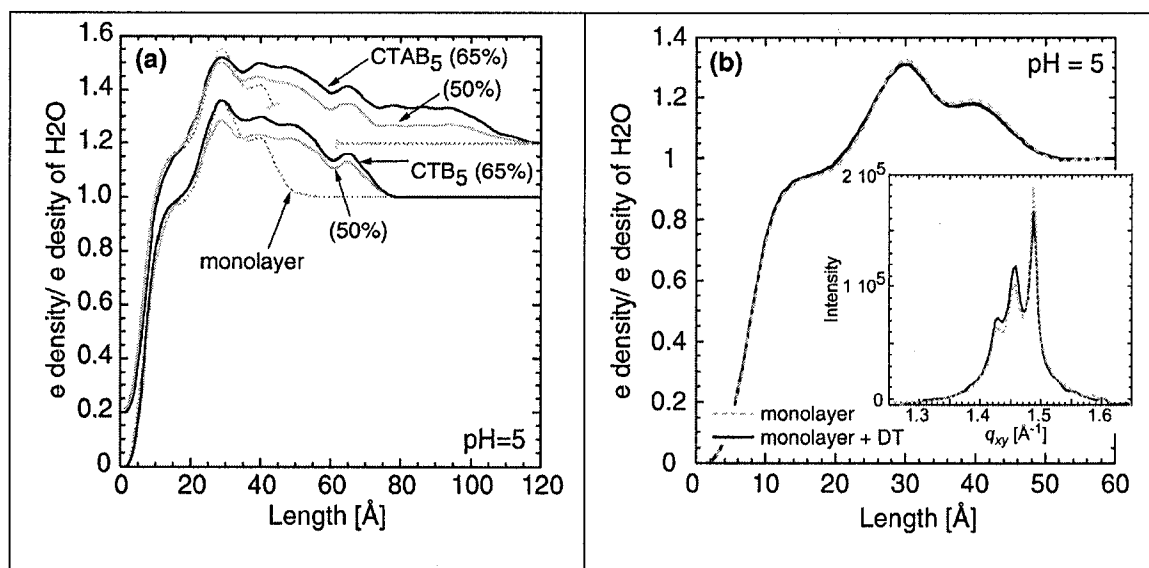


Figure 2-4: The electron density profile in (a) illustrates the possible variance in the amount of protein coverage between samples. Shown are two cases of CTB₅ and CTAB₅ at pH=5. Both CTAB₅ profiles have been shifted up 0.2 for clarity. The coverage ranges from approximately 50 – 65 % and can also be monitored by the percent increase in the area per molecule on the trough. Larger increases in area per molecule of the lipid monolayer are indicative of more protein being bound. There are small differences in the electron density of the monolayer region between cases when different amounts of protein are bound but these are not sufficient to account for the perturbation to the monolayer at different pH seen in **Fig. 2-2** and **Fig. 2-3**. (b) Reflectivity and GIXD results illustrate that addition of dithiothreitol (“activation

ingredient”) has no significant effect on the area per molecule, electron density, or in-plane diffraction of the monolayer when no protein is present. The electron density profiles of the monolayer before and after the addition of DT can be superimposed on each other. The inset of (b) shows no significant changes in the diffraction from the lipid tails when DT is present.

GIXD Analysis (pH=8)

GIXD measurements provide in-plane structural information of the crystalline, diffracting portion of the monolayer. In general, the diffraction from the lipid-protein system is observed in two regions. First, is the low q_{xy} region from 0.08\AA^{-1} to 0.35\AA^{-1} corresponding to d -spacings of ~ 80 to ~ 18 Å. In this first zone, diffraction from the 2-D ordering of the cholera layer can be seen. Second, is the q_{xy} region from ~ 1.3 to ~ 1.6 \AA^{-1} corresponding to d -spacings of ~ 4.4 to ~ 4.2 Å, where diffraction from the alkyl tails is visible.

Diffraction from the protein layer

We observed diffraction from the cholera protein layer bound to the lipid monolayer in the form of macroscopic, two-dimensional cholera toxin crystals assembled with high coverage. This is only the fourth protein to be crystallized in 2-D in a fully hydrated state and studied with GIXD. The amount of coverage varied between 50% and 65% as shown earlier in the reflectivity results. The diffraction pattern obtained for the cholera protein layer at pH=8 and 20 mN/m is shown in **Fig. 2-5** and summarized in **Table 2-1**. For each scan, one strong peak and 3 weak peaks can be distinguished. The observed GIXD Bragg peaks indicate the packing of the toxins is a hexagonal 2-D unit cell. The Miller indices $\{h, k\}$ of the observed peaks are indicated in **Fig. 2-5a**. The Bragg

peaks were integrated over the region $(-0.05 \text{ \AA}^{-1} \leq q_z \leq 0.4 \text{ \AA}^{-1})$. For a hexagonal unit cell with dimension a_{hex} , the spacing between $\{h, k\}$ planes are described by the following formula:

$$1/d_{hk}^2 = 4(h^2 + hk + k^2) / 3a_{\text{hex}}^2,$$

$$d_{10} = a_{\text{hex}} \sqrt{3}/2,$$

$$d_{11} = a_{\text{hex}}/2,$$

$$d_{20} = a_{\text{hex}} \sqrt{3}/4,$$

$$d_{21} = 3a_{\text{hex}}/2\sqrt{7}.$$

The consequent hexagonal unit cell is $74.1 \pm 1 \text{ \AA}$ for CTB₅, $71.5 \pm 1 \text{ \AA}$ for CTB₅+DT, $72.0 \pm 2.0 \text{ \AA}$ for CTAB₅, and $70.8 \pm 1 \text{ \AA}$ for CTAB₅+DT. There is a more prominent decrease in a_{hex} after activation of CTB₅. There is no significant change in a_{hex} after activation of CTAB₅. There is a significant change in the observed d -spacings for the $\{2,0\}$ peak for CTB₅ and the $\{1,1\}$ peak for CTAB₅ after activation. Many of the individual Bragg peaks become more pronounced after activation. This result will be discussed further in the pH=5 section.

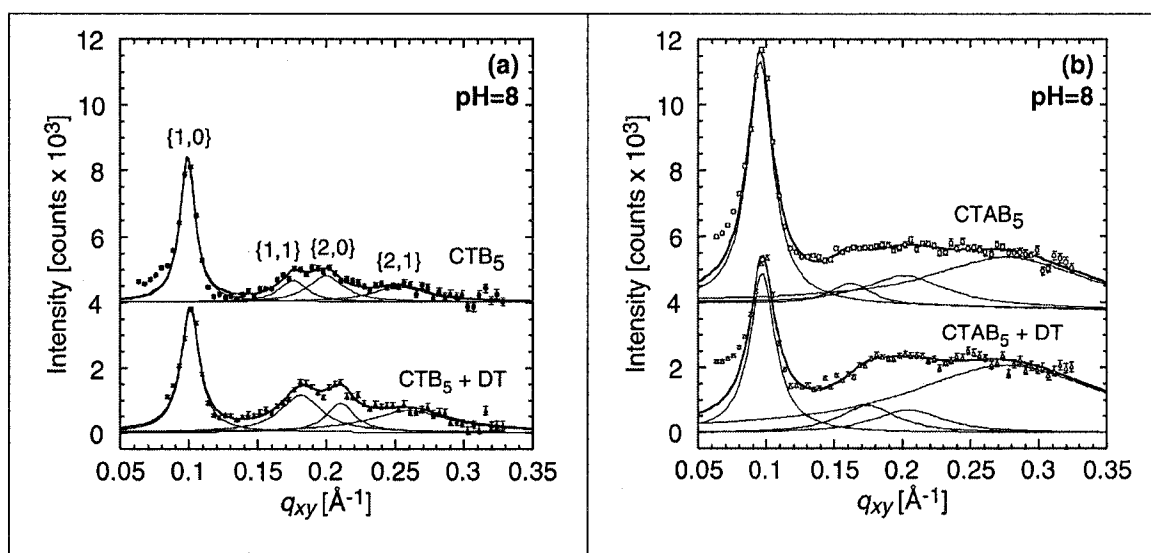


Figure 2-5: Grazing incidence x-ray diffraction (GIXD) Bragg peaks obtained for layers of CTB₅ and CTAB₅ with a subphase at pH=8, surface pressure = 20 mN/m, and temperature = 23°C. The toxins were nucleated under the DPPE: GM1 monolayer forming a 2-D crystal monolayer. For clarity, Bragg peaks have been offset vertically by 4×10^3 counts. The observed GIXD Bragg peaks indicate packing of the toxins in a hexagonal 2-D unit cell. **(a)** Bragg peaks from the protein layer corresponding to CTB₅ and CTB₅+DT. Miller indices $\{h, k\}$ of the observed peaks are indicated in panel (a). Bragg peaks were integrated over the q_z region from -0.05 to 0.4 \AA^{-1} . Peaks were fitted (solid lines) using Lorentzian curves (see **Table 2-1** for details). **(b)** Bragg peaks from the protein layer corresponding to CTAB₅ and CTAB₅+DT. Intensities and positions of the Bragg peaks (especially higher order) in the case of CTAB₅ are obtained with larger uncertainties due to weaker in-plane ordering and higher incoherent background contribution.

Bragg rod profiles corresponding to scattering from the cholera molecules (**Fig. 2-6**) at pH=8 were produced by integrating through the $0.075 \text{ \AA}^{-1} \leq q_{xy} \leq 0.12 \text{ \AA}^{-1}$ region of the $\{1,0\}$ peak. The q_{xy} positions of these Bragg rods are determined by the packing of the cholera molecules. Bragg rods are extended in q_z space and the scattered intensity along q_z is modulated by the form factor of the scattering units. Cylindrical objects were used to approximate the scattering units and the cylindrical form factor was used to calculate Bragg rod profiles. Parameters corresponding to the cylinder's height, radius, tilt angle and tilt direction relative to the unit cell were adjusted using a Levenberg-

Marquardt least-squares fitting algorithm to attain the best possible fit. All structural parameters of the cholera layer obtained from this analysis are reported in **Table 2-2**.

The CTB₅ Bragg rod can be modeled using the form factor of a single tilted cylinder with its tilt aligned to the CTB₅ hexagonal packing. The radius of the cylinder is 35.5 Å and matches well with a radius of 31 Å reported from the 3-D crystal structure. The 3-D crystal structure shows that the height of the B₅ pentamer is 32 Å but the height of the scattering cylinder used by our models was 54 Å. We hypothesize that these scattering cylinders represent the CTB₅ molecule and a portion of the lipids constrained to its binding sites. This interpretation matches the thickness measured by reflectivity and the tilt of the cylinder, 45°, is consistent with the tilt of the lipid layer obtained from GIXD analysis (**Table 2-3**). However, since the height of the cylinder is roughly double the height of the crystal structure, we cannot rule out the possibility of a double layer of stacked CTB₅ molecules. In the case of CTB₅+DT, the parameters of the cylinder do not significantly change. For pH8, the CTB₅ portion of the electron density profile does not notably change, consistent with the out-of-plane results before and after DT is injected. The drastic changes that take place after DT is introduced are in the lipid tail electron density (**Fig. 2-2**) and can also be seen in the diffraction from the lipid tails. After activation, the height of the cylinder slightly decreases which is consistent with a few angstrom decrease in the thickness of the lipid tails seen in the reflectivity results. The same trend is seen after activation of CTAB₅.

The Bragg rod scattering from CTAB₅ could not be modeled using a single population of tilted cylinders. Instead, 2 populations of tilted cylinders were used. Population 1 has a vertical height of 52 Å and population 2 has a height of 83 Å. The

short cylinder (population 1) represents scattering from B₅ pentamer and a portion of the lipid molecules, equivalent to the single population in the case of CTB₅. We hypothesize that the A unit has significant freedom of motion relative to the B₅ unit. In population 1, the A unit is oriented in a way which does not contribute to the coherent scattering from the CTB₅ pentamer and attached lipid molecules. On the other hand, the taller cylinders used to model population 2 represent scattering from CTAB₅ molecules whose A units are more rigidly bound to CTB and oriented in a way that coherently contributes to the overall scattering from the remainder of the molecule and lipids. Before addition of DT, our models indicate 29% occupancy of population 1 and 71% occupancy of population 2. After activation with DT, the occupancy is 50% for population 1 and 50% for population 2. This change is consistent with a significant fraction of the A1 units being cleaved and losing their rigidity or being released from the B₅:A1 molecule.

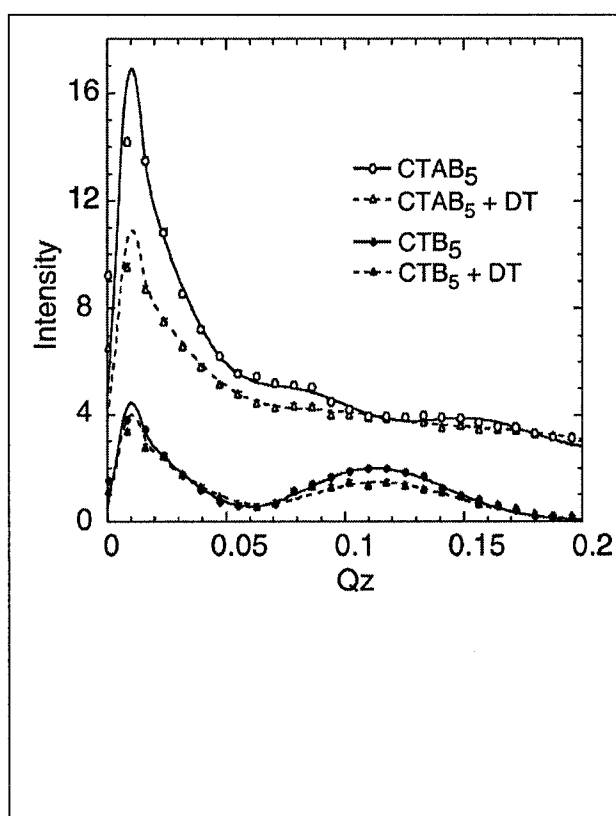


Figure 2-6: Bragg rod profiles corresponding to scattering from the cholera protein layer at pH=8. Rods were produced by integrating through the $0.075 \text{ \AA}^{-1} \leq q_{xy} \leq 0.12 \text{ \AA}^{-1}$ region of the $\{1,0\}$ Bragg peaks in Fig. 2-5. Cylindrical objects were used to approximate the scattering units and structural parameters such as the cylinder's height, radius, tilt angle and tilt direction relative to the unit cell of the cholera layer are reported in Table 2-2.

Diffraction from the lipid monolayer

As mentioned earlier, we also observed diffraction from the alkyl tails of the lipid monolayer. The diffraction pattern obtained for pure DPPE: GM₁ monolayers at pH=8 and 20 mN/m is shown in **Fig. 2-7a** and summarized in **Table 2-3**. Three Bragg peaks are observed at $q_{xy} = 1.43 \text{ \AA}^{-1}$, $q_{xy} = 1.45 \text{ \AA}^{-1}$ and $q_{xy} = 1.49 \text{ \AA}^{-1}$. The existence of three Bragg peaks is indicative of an oblique cell. The integrated intensities of the Bragg peaks ($-0.05 \text{ \AA}^{-1} \leq q_z \leq 0.9 \text{ \AA}^{-1}$) are approximately the same in agreement with the multiplicity rule. The calculated d -spacings, $d_{10} = 4.41 \text{ \AA}$ ($d_{xy} = 2\pi/q_{xy}$), $d_{01} = 4.33 \text{ \AA}$, and $d_{1-1} = 4.23 \text{ \AA}$, gives rise to a primitive unit cell with dimensions of $|a| = 4.99 \text{ \AA}$, $|b| = 4.89 \text{ \AA}$, and $\gamma = 117.8$ degrees and an area per two alkyl chains, A_{20} , of 43.19 \AA^2 .

The corresponding full width at half maximum height (FWHM) of the three peaks exceeds the instrumental resolution of $FWHM_{resol}(q_{xy}) = 0.0084 \text{ \AA}^{-1}$. The intrinsic FWHM can be obtained using the equation:

$$FWHM_{intrinsic}(q_{xy}) = [FWHM_{meas}(q_{xy})^2 - FWHM_{resol}(q_{xy})^2]^{1/2}$$

A simple model assumes that the monolayer consists of 2D crystallites that are perfect and have a finite average size L_{xy} , the *coherence length*. Using the Scherrer formula [40], we can calculate the coherence length in the three crystallographic directions by

$$L_{xy} \approx 0.9[2\pi / FWHM_{intrinsic}(q_{xy})] \{h, k\}.$$

We find the corresponding coherence lengths for the three peaks to be $L_{10} = 223 \text{ \AA}$, $L_{01} = 227 \text{ \AA}$, and $L_{1-1} = 474 \text{ \AA}$. A distance of 474 \AA is approximately 65 lipids across.

The Bragg rod profiles, shown in **Fig. 2-7b**, were produced by integrating through the $1.38 \text{ \AA}^{-1} \leq q_{xy} \leq 1.55 \text{ \AA}^{-1}$ region of the three peaks. Analysis of the Bragg rod profiles

was done by approximating the lipid alkyl tails as cylinders with constant electron density [36]. Lipid monolayer Bragg rods were fitted using a model of low tilt (model *I*) and a model of high tilt (model *II*). See **Table 2-3** for details. For a DPPE: GM₁ monolayer at pH=8, 20 mN/m, and with no protein present our analysis showed that the molecules have a tilt angle of $22 \pm 2.0^\circ$ from the surface normal and an azimuthal angle of $13.7 \pm 2.0^\circ$. The effective thickness of the coherently scattering part of the molecule is $20 \pm 1.0 \text{ \AA}$.

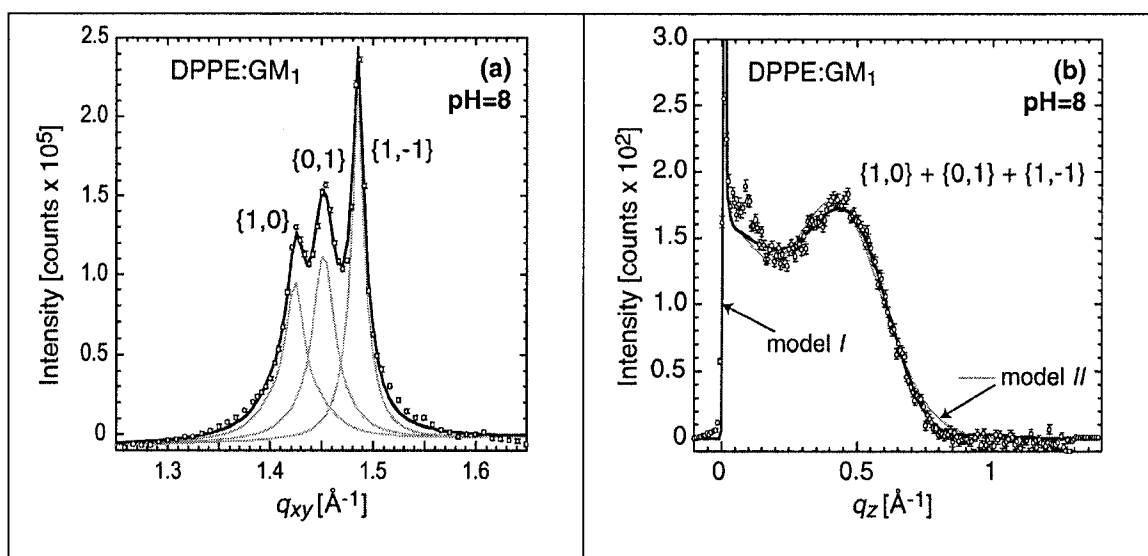


Figure 2-7: Grazing incidence x-ray diffraction (GIXD) from the alkyl tails (water subphase at pH=8, surface pressure = 20 mN/m, T = 23°C) for a DPPE: GM₁ monolayer. Bragg peaks from the lipid tails are shown in (a) and Bragg rods are shown in (b). The observed three GIXD Bragg peaks indicate packing of the lipid tails in an oblique 2-D unit cell. The Miller indices $\{h, k\}$ are indicated for each peak: $\{1,0\}$ for the right, $\{0,1\}$ for the middle and $\{1,-1\}$ for the left. The molecular packing parameters used in the fitting are listed in **Table 2-3**. Bragg peaks in (a) were obtained by integrating over the $(-0.05 \text{ \AA}^{-1} \leq q_z \leq 0.9 \text{ \AA}^{-1})$ region and fit individually (gray solid lines). By integrating over the $(1.38 \text{ \AA}^{-1} \leq q_{xy} \leq 1.55 \text{ \AA}^{-1})$ region, Bragg rods (b) were fitted (solid line) by approximating the coherently scattering part of the acyl chain by a cylinder of constant electron density. The sharp peak at $q_z = 0.01 \text{ \AA}^{-1}$ is the so-called *Yoneda - Vineyard* peak [41], which arises from the interference between x-rays diffracted up into the Bragg rod and x-rays diffracted down and then reflected up by the interface. The rods were fitted using two different models (*I* and *II*) -see **Table 2-3** for details.

Binding CTB₅ and CTAB₅ decreases the crystallinity of the lipid monolayer

GIXD diffraction from the lipid tails with bound CTB₅ and CTAB₅ at pH=8 is shown in **Figure 2-8** with structural parameters summarized in **Table 2-3**. When cholera is injected into the subphase of the trough it has considerable effects on the in-plane diffraction of the lipid tails. Before cholera is present there is a 22° tilt to the lipid tails. After CTB₅ and CTAB₅ bind there is an increase in tilt to 53° and 44° respectively. This is commensurate with the area per molecule expansion measured by the trough area.

After activation, there is an additional increase in the tilt angle of the lipid tails due to further expansion of the trough. Increased molecular tilt corresponds to a decrease in the thickness of the lipid tail region. Results from reflectivity analysis are consistent with a decrease in the thickness of the lipid tail region. It can be seen in **Fig. 2-8a** that diffraction from the monolayer when CTB₅ binds is very similar to diffraction from the monolayer before protein binds (dashed line). This is consistent with reflectivity results at pH=8. However, CTAB₅ has a more dramatic effect on monolayer diffraction even though reflectivity shows no significant increase to the lipid tail density.

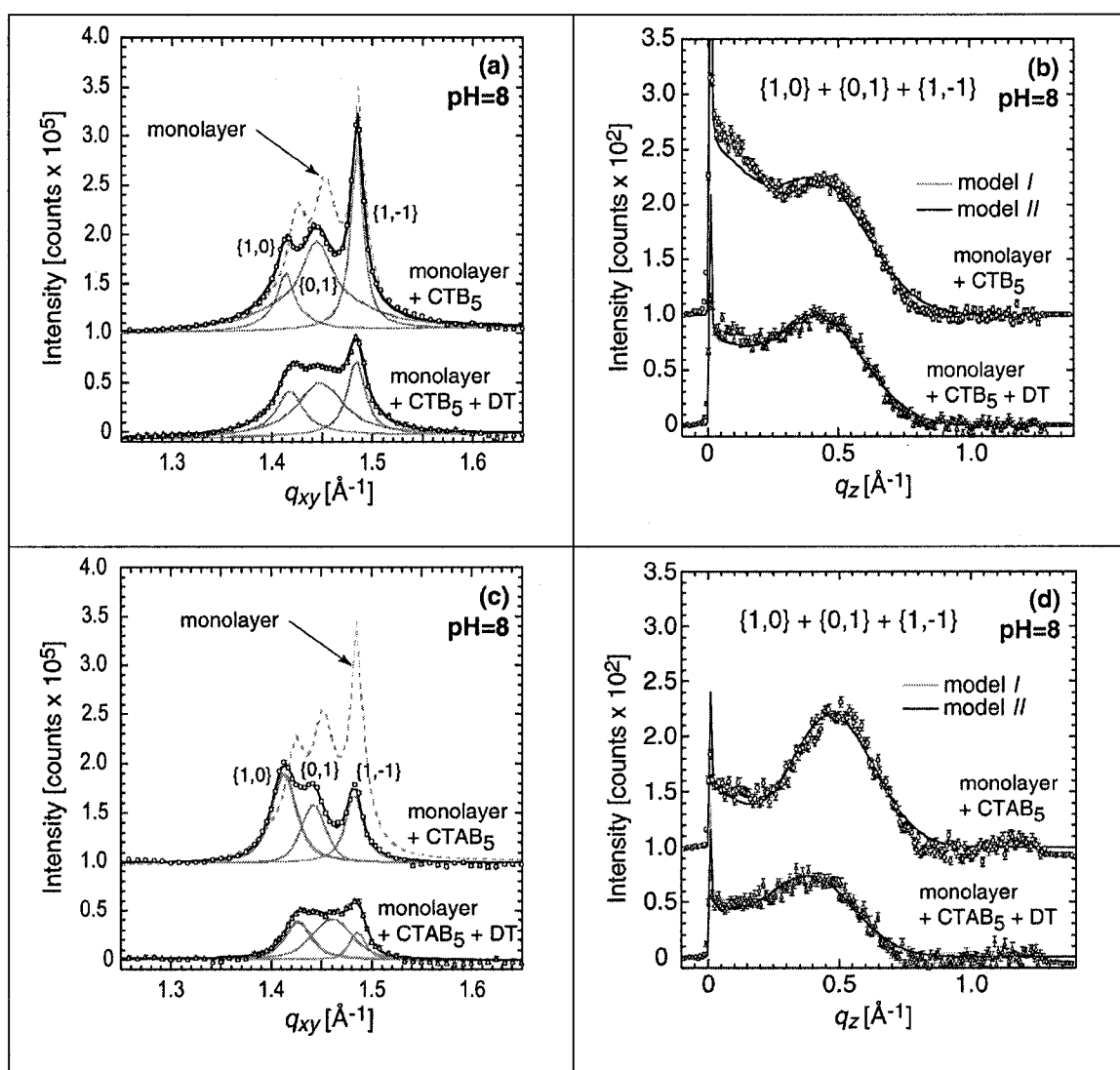


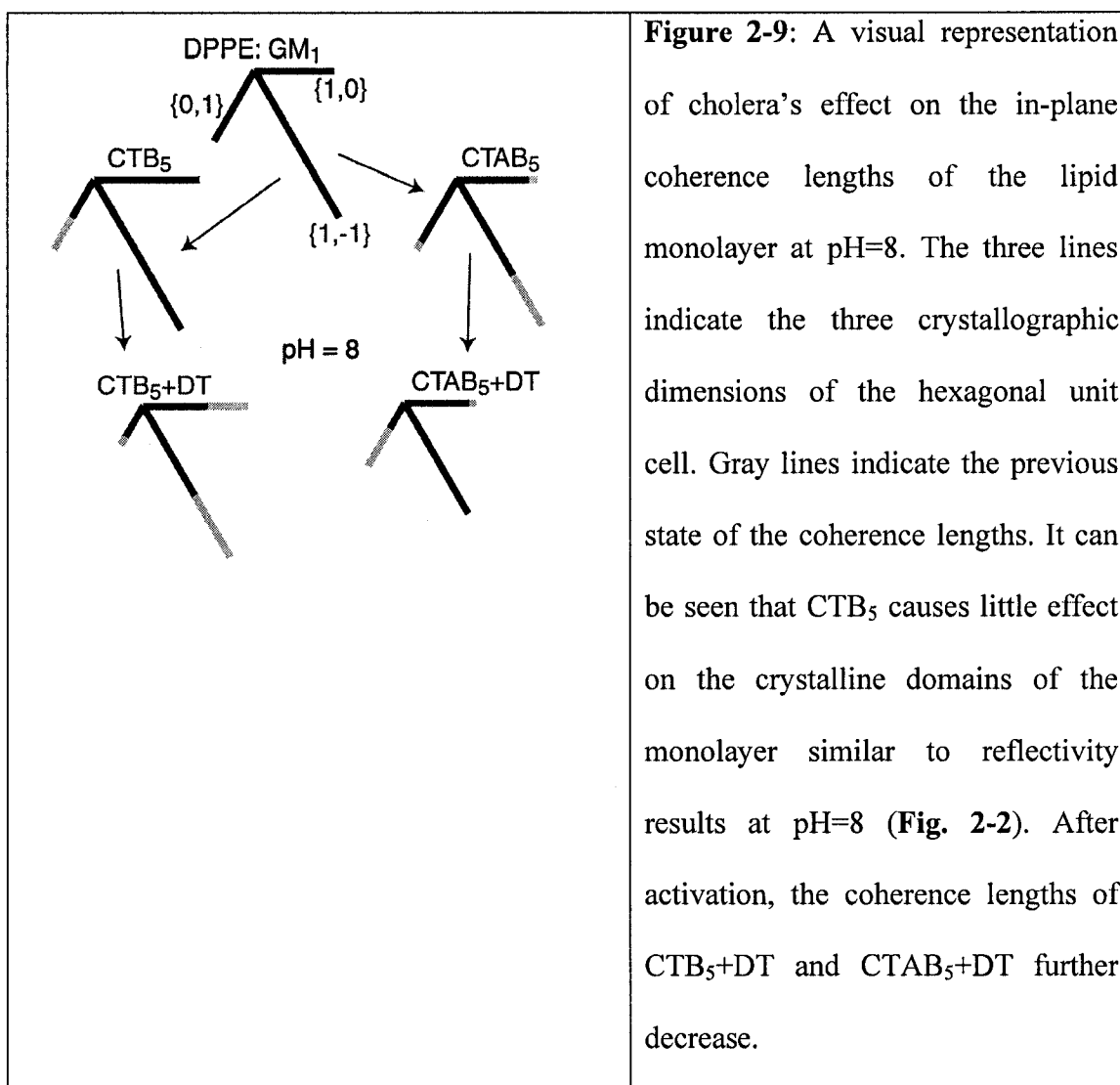
Figure 2-8: Bragg peaks and rods from GIXD measurements (water subphase at pH=8, surface pressure 20 mN/m, temperature 23°C). (a) and (b) show Bragg peaks and Bragg rods respectively for a DPPE: GM₁ monolayer with bound CTB₅ and CTB₅+DT. (c) and (d) show Bragg peaks and Bragg rods respectively for a DPPE: GM₁ monolayer with bound CTAB₅ and CTAB₅+DT. For clarity, the Bragg peaks data in (a) and (c) have been offset vertically by 10⁵ counts and the Bragg rods in (b) and (d) by 100 counts. The observed three GIXD Bragg peaks indicate packing of the lipid tails in an oblique 2-D unit cell. The Miller indices $\{h, k\}$ are indicated for each peak ($\{1,0\}$ for the left, $\{0,1\}$ for the middle, and $\{1,-1\}$ for the right). The molecular packing parameters used in the fitting are listed in **Table 2-3**. Integrated over the $(q_{xy}, q_z)=(1.38-1.55 \text{ \AA}^{-1}, -0.05-0.9 \text{ \AA}^{-1})$ region, Bragg rods were fitted (solid lines) by approximating the coherently scattering part of the acyl chain by a cylinder of constant electron density. The sharp peak at $q_z = 0.01 \text{ \AA}^{-1}$ is the so-called *Yoneda - Vineyard* peak (Vineyard 1982), which arises from the interference between X-rays diffracted up into the Bragg rod and X-rays diffracted down and then reflected up by the interface. The rods were fitted using two different models (*I* and *II*) -see **Table 2-3** for details.

The change in the observed diffraction of the lipid tail Bragg peaks is not exclusively due to an increase in area/molecule (trough expansion). Proof of this comes from comparing GIXD scans from a DPPE: GM₁ monolayer at 20mN/m to scan of the same monolayer composition at 5, 30, and 45 mN/m. At lower pressure, the peaks shift to lower q_{xy} and at higher pressure, the peaks shift to higher q_{xy} (data not shown). These shifts are consistent with an increase and decrease in the packing area for the respective

surface pressures. This is very different than what is observed when CTB₅/CTAB₅ bind at a constant pressure of 20mN/m because the peak positions do not shift significantly. More notably, the integrated intensities of the peaks are greatly affected by the binding of cholera. When CTB₅ binds, the integrated Bragg peak intensity decreases by 17%. There is a 47% decrease in intensity when CTAB₅ binds. After activation of both CTB₅ and CTAB₅, there is considerable amount of further decrease.

In-plane coherence lengths

Disturbance of the crystallinity also has a large effect on the in-plane coherence lengths (L_{xy}) of the lipid tails (shown in **Table 2-3**). These changes in coherence length are depicted in **Fig. 2-9**. Before and after activation, CTB₅ and CTAB₅ had similar effects on the crystalline domains of the monolayer. After CTB₅ binds, L_{10} increased by 31% and L_{01} decreased by 46%. After activation (CTB₅ + DT), there is a 38%, 19%, and 41% further decrease to L_{10} , L_{01} , and L_{1-1} respectively. This is consistent with degradation of the monolayer crystallinity. When CTAB₅ binds to the monolayer all coherence lengths are affected with the largest decrease to L_{1-1} . After activation (CTAB₅ + DT), there is an 11%, and 60% further decrease to L_{10} , and L_{1-1} respectively. Therefore, both CTB₅ and CTAB₅ (before and after activation) exhibit similar perturbations on the monolayer. There are no significant changes in diffraction pattern of lipid tail peaks when DT is added to monolayer with no protein present (**Fig. 2-4b** inset). This demonstrates that protein binding and activation are the cause of these monolayer perturbations.



GIXD Analysis (pH=5)

Diffraction from the protein layer

The diffraction pattern obtained for the cholera protein layer at pH=5 and 20 mN/m is shown in Fig. 2-10 and summarized in Table 2-1. For each scan, one strong peak and 3 weak peaks can be distinguished. The observed GIXD Bragg peaks indicate the packing of the toxins is a hexagonal 2-D unit cell. The Miller indices $\{h, k\}$ of the observed peaks are indicated in Fig. 2-10a. The Bragg peaks were integrated over the region $(-0.05 \text{ \AA}^{-1} \leq q_z \leq 0.4 \text{ \AA}^{-1})$. The consequent hexagonal unit cell is $72.2 \pm 1 \text{ \AA}$ for

CTB₅, $71.0 \pm 1 \text{ \AA}$ for CTB₅+DT, $73.2 \pm 1.5 \text{ \AA}$ for CTAB₅, and $70.7 \pm 1 \text{ \AA}$ for CTAB₅+DT. At pH =5, CTB₅ has a unit cell dimension similar to CTAB₅+DT and there is no prominent decrease in a_{hex} after activation of CTB₅ like in the pH=8 results. This is consistent with the large monolayer perturbation caused by CTB₅ at pH=5 seen in the reflectivity results. There is a more significant change in a_{hex} after activation of CTAB₅ when compared to pH=8. There is a significant change in the observed d -spacings for the {2,0} and the {1,1} peak for CTAB₅ after activation. Many of the individual Bragg peaks become more pronounced after activation, especially in the case of CTAB₅. Before activation, CTAB₅ has very weak, broad Bragg peaks but the CTAB₅+DT peaks are more intense indicating that the protein layer is becoming more crystalline. The same effect can be seen by an increase in the in-plane coherence lengths (**Table 2-1**). In fact, the Bragg peaks of CTAB₅+DT look very similar to that of CTB₅ suggesting that the A1 subunit has been release from the CTB₅ molecule. This outcome is more prevalent at pH=5, another piece of evidence that suggests that low pH is necessary for the membrane penetration mechanism. Bragg rod profiles of the {1,0} Bragg peak are extremely similar the Bragg rod profiles for the pH=5 results (**Fig. 2-6**).

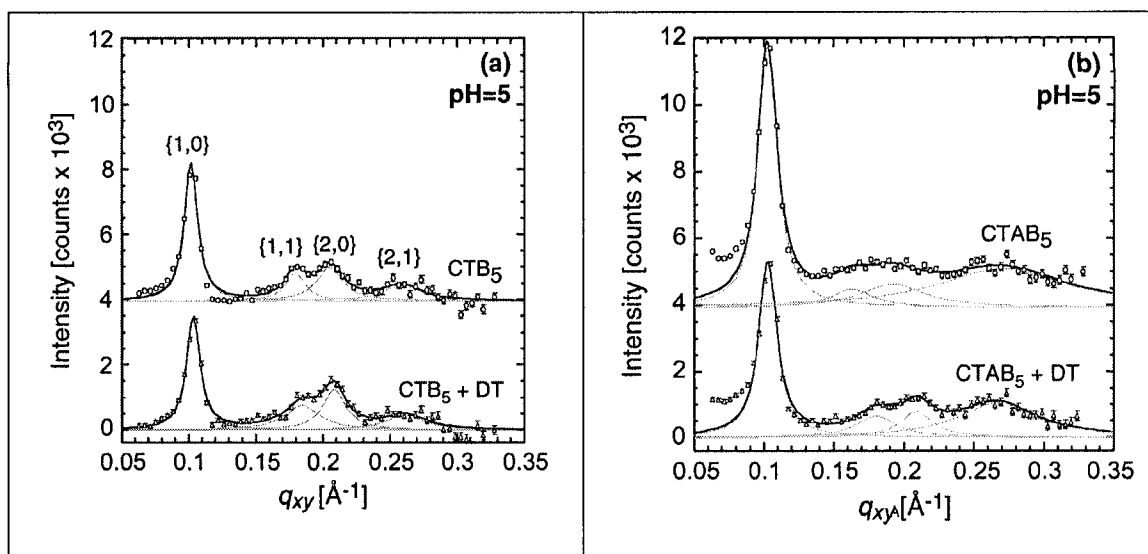


Figure 2-10: Grazing incidence x-ray diffraction (GIXD) Bragg peaks obtained for layers of CTB₅ and CTAB₅ with a subphase at pH=5, surface pressure = 20 mN/m, and temperature = 23°C. The toxins were nucleated under the DPPE: GM1 monolayer forming a 2-D crystal monolayer. For clarity, Bragg peaks have been offset vertically by 4×10^3 counts. The observed GIXD Bragg peaks indicate packing of the toxins in a hexagonal 2-D unit cell. **(a)** Bragg peaks from the protein layer corresponding to CTB₅ and CTB₅+DT. Miller indices $\{h, k\}$ of the observed peaks are indicated in panel (a). Bragg peaks were integrated over the q_z region from -0.05 to 0.4 \AA^{-1} . Peaks were fitted (solid lines) using Lorentzian curves (see **Table 2-1** for details). **(b)** Bragg peaks from the protein layer corresponding to CTAB₅ and CTAB₅+DT. Intensities and positions of the Bragg peaks (especially higher order) in the case of CTAB₅ are obtained with larger uncertainties due to weaker in-plane ordering and higher incoherent background contribution. Different from pH=8, diffraction from CTAB₅+DT is very similar to CTB₅.

Diffraction from the lipid monolayer

The diffraction pattern obtained for pure DPPE: GM₁ monolayers at pH=5 and 20 mN/m is shown in **Fig. 2-11a** and summarized in **Table 2-4**. Three Bragg peaks are observed at $q_{xy} = 1.43 \text{ \AA}^{-1}$, $q_{xy} = 1.45 \text{ \AA}^{-1}$ and $q_{xy} = 1.49 \text{ \AA}^{-1}$. The existence of three Bragg peaks is indicative of an oblique cell. The integrated intensities of the Bragg peaks ($-0.05 \text{ \AA}^{-1} \leq q_z \leq 0.9 \text{ \AA}^{-1}$) are approximately the same in agreement with the multiplicity rule. The calculated d -spacings, $d_{10} = 4.39 \text{ \AA}$ ($d_{xy} = 2\pi/q_{xy}$), $d_{01} = 4.31 \text{ \AA}$, and $d_{1-1} = 4.23 \text{ \AA}$, gives rise to a primitive unit cell with dimensions of $|a| = 4.98 \text{ \AA}$, $|b| = 4.88 \text{ \AA}$, and $\gamma = 118.1$ degrees and an area per two alkyl chains, A_{20} , of 42.86 \AA^2 .

The Bragg rod profiles, shown in **Fig. 2-11b**, were produced by integrating through the $1.38 \text{ \AA}^{-1} \leq q_{xy} \leq 1.55 \text{ \AA}^{-1}$ region of the three peaks. Lipid monolayer Bragg rods were fitted using a model of low tilt (model *I*) and a model of high tilt (model *II*). See **Table 2-4** for details. For DPPE: GM₁ monolayers at 20 mN/m with no protein present our analysis shows that the molecules have a tilt angle of $24 \pm 2.0^\circ$ from the surface normal and the azimuthal angle of $13.0 \pm 2.0^\circ$. The effective thickness of the coherently scattering part of the molecule is $20 \pm 1.0 \text{ \AA}$.

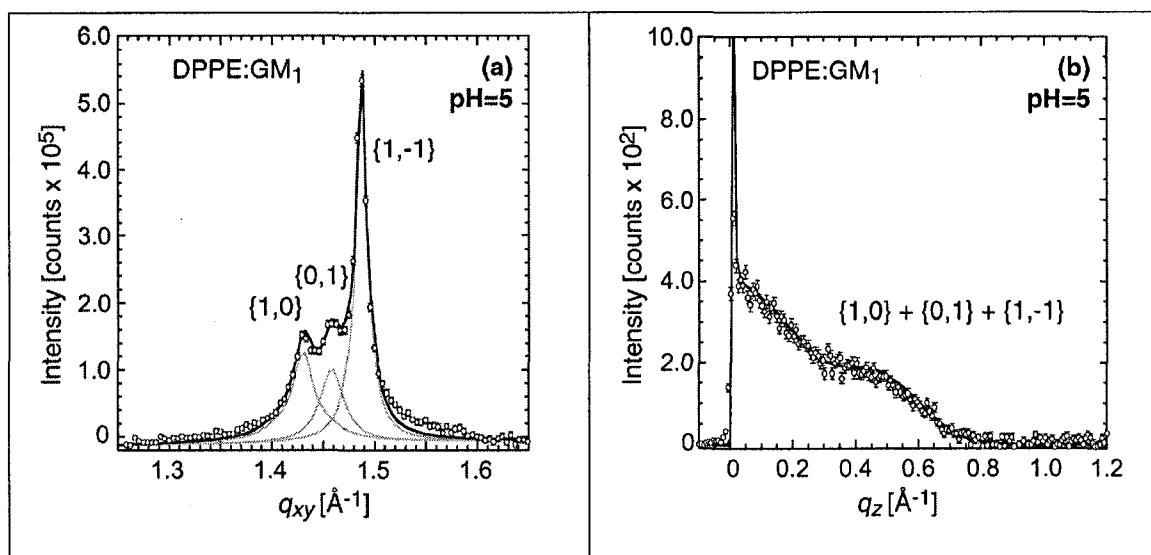
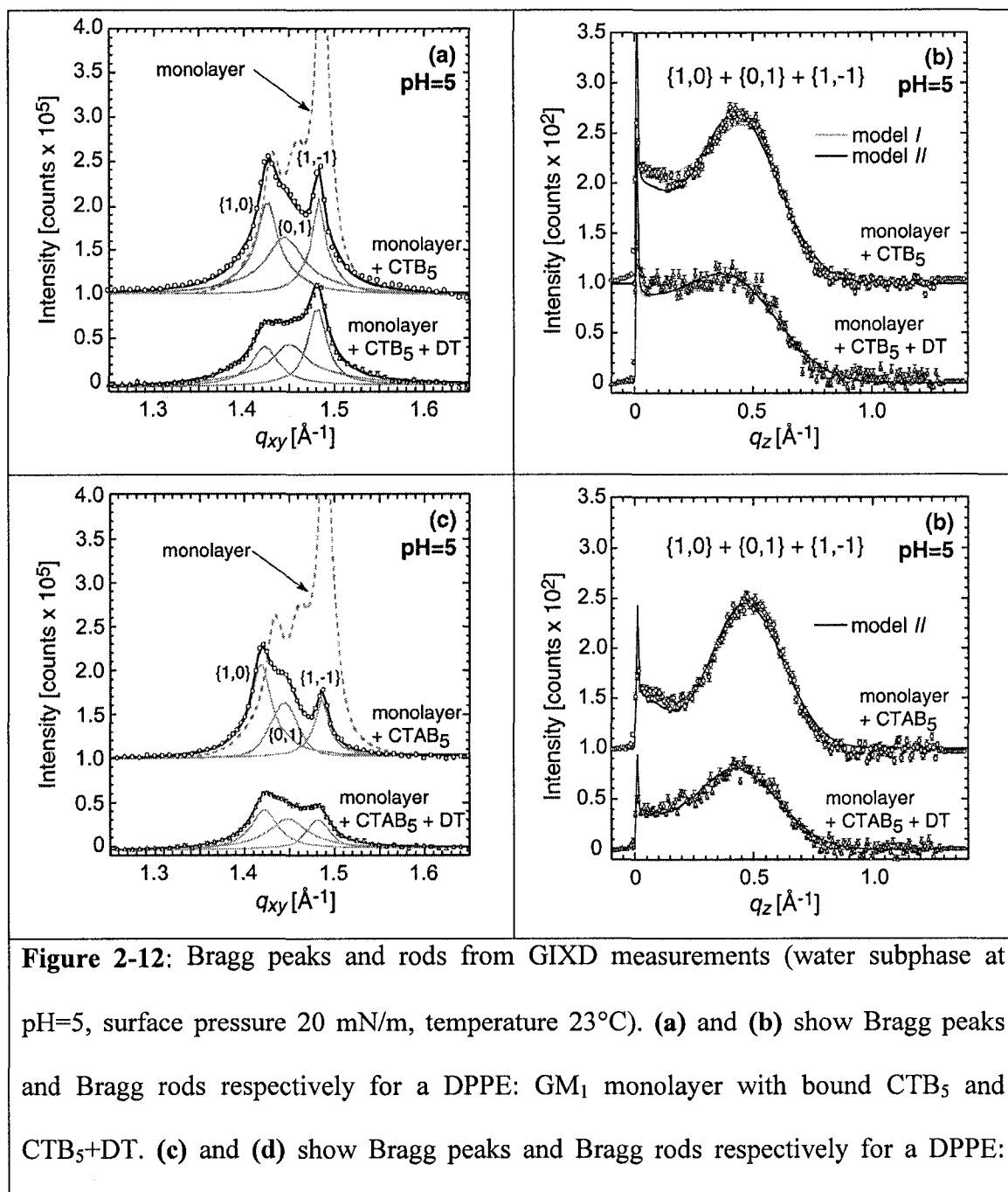


Figure 2-11: Bragg peaks and rods of DPPE:GM₁ monolayer, pH5, 20 mN/m, 23°C.

The observed three GIXD Bragg peaks indicate packing of the lipid tails in an oblique 2-D unit cell. The Miller indices $\{h, k\}$ are indicated for each peak $\{1,0\}$ for the right, $\{0,1\}$ for the middle and $\{1,-1\}$ for the left). The molecular packing parameters used in the fitting are listed in **Table 2-4**. The integrated over the $(q_{xy}, q_z) = (1.3-1.6 \text{ \AA}^{-1}, 0.0-1.0 \text{ \AA}^{-1})$ region, Bragg rods were fitted (solid line) by approximating the coherently scattering part of the acyl chain by a cylinder of constant electron density. The sharp peak at $q_z = 0.01 \text{ \AA}^{-1}$ is the so-called *Yoneda - Vineyard* peak [41].

GIXD from the lipid tails after protein binding at pH=5 is shown in **Fig. 2-12** and reported in **Table 2-4**. At first glance, there are no significant differences in the observed GIXD before protein binding when compared to that observed at pH=8. For example, there is little to no difference in the peak positions of the lipid tail diffraction profile. After analysis, subtle differences are observed. For instance, at pH=5 the L_{10} , L_{01} , and $L_{1,-1}$ coherence lengths for CTB₅ before activation are smaller than at pH=8 (**Fig. 2-7**, **Table 2-3**). After activation, they are equivalent to what is observed at pH=8. In other words,

CTB₅ has a larger effect on the coherence lengths of the monolayer at pH=5 when compared to pH=8. After activation, the effect on the monolayer is the same between pH values. As discussed above, this is the same result observed in the electron density profiles obtained from reflectivity.

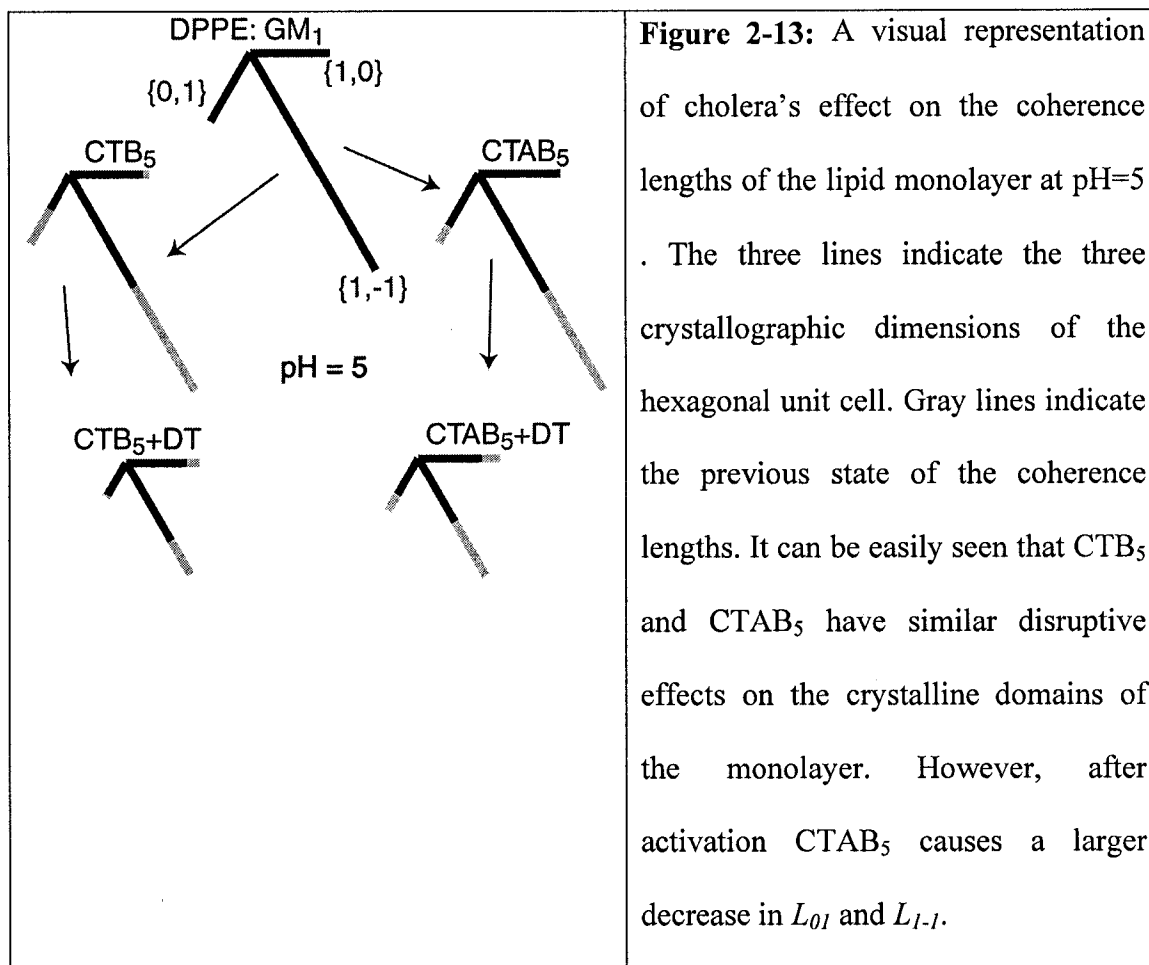


GM₁ monolayer with bound CTAB₅ and CTAB₅+DT. For clarity, the Bragg peaks data in (a) and (c) have been offset vertically by 10^5 counts and the Bragg rods in (b) and (d) by 100 counts. The observed three GIXD Bragg peaks indicate packing of the lipid tails in an oblique 2-D unit cell. The Miller indices $\{h, k\}$ are indicated for each peak ($\{1,0\}$ for the left, $\{0,1\}$ for the middle, and $\{1,-1\}$ for the right). The molecular packing parameters used in the fitting are listed in **Table 2-4**. Integrated over the $(q_x, q_z)=(1.38-1.55 \text{ \AA}^{-1}, -0.05-0.9 \text{ \AA}^{-1})$ region, Bragg rods were fitted (solid lines) by approximating the coherently scattering part of the acyl chain by a cylinder of constant electron density. The sharp peak at $q_z = 0.01 \text{ \AA}^{-1}$ is the so-called *Yoneda - Vineyard* peak [41], which arises from the interference between X-rays diffracted up into the Bragg rod and X-rays diffracted down and then reflected up by the interface. The rods were fitted using two different models (*I* and *II*) -see **Table 2-4** for details.

In-plane coherence lengths

Changes in coherence length are depicted in **Fig. 2-13** and shown in Table 4. Before activation, CTB₅ had a larger effect on the crystalline domains of the monolayer when compared to pH=8. After CTB₅ binds, L_{10} decreased by 8%, L_{01} decreased by 50%, and L_{1-1} decreased by 48%. After activation (CTB₅ + DT), there is a 18%, 7%, and 30% further decrease to L_{10} , L_{01} , and L_{1-1} respectively. This is also consistent with degradation of the monolayer crystallinity. When CTAB₅ binds to the monolayer all coherence lengths are affected with the largest decrease to L_{1-1} . After activation (CTAB₅ + DT), there is a 23%, 31%, and 46% further decrease to L_{10} , L_{01} and L_{1-1} respectively. The

largest effect on the crystallinity of the monolayer between both pH values is seen at pH=5 for CTAB₅+DT, further evidence that low pH is important.



Discussion/Conclusions

Protein entry into the lipid tail region can easily be monitored by an increase in electron density seen in the electron density profiles obtained from the measured reflectivity data. Protein enters the lipid tail region in the case of CTB₅ (pH=5), CTB₅+DT (pH=5 and pH=8), and CTAB₅+DT (pH=5 and pH=8). It has also been shown that at pH8.2, CTB₅ does not deeply penetrate into the bilayer [42].

As protein binds, the crystallinity of the monolayer is degraded. The least amount of crystalline destruction occurs for CTB₅ at pH=8 and the largest effect to the lipid monolayer occurs in the case of CTAB₅+DT at pH=5. This result is seen from the reflectivity, changes in the in-plane coherence lengths, and the area expansion results supporting the importance of low pH in the infection mechanism. It should be noted that the decrease in integrated intensity of the lipid monolayer Bragg peaks is not purely due to protein binding causing a decrease in the amount of monolayer that diffracts x-rays. In a non-rigorous Bragg rod model test we observed that solely increasing the tilt of the lipid molecule causes a decrease in integrated intensity.

Several results suggest that CTB₅ plays a more active role than solely binding the cholera molecule to the lipid membrane. Most notably is the penetration of CTB₅ into the monolayer at low pH. Other studies have shown that low pH causes the B₅ pentamer to insert into biological membranes. Voltage clamp experiments showed that low pH caused CTB₅ to form ion channels in bilayer lipid membranes [39]. Fluorescence resonance energy transfer experiments have shown that low pH causes CTB₅ to penetrate into membrane before activation [43]. These fluorescence experiments provide alternative evidence that low pH induces conformational changes in CTB₅ that directly influence membrane structure at the site of CTB₅ binding. This pH dependence most likely is attributed to CTB₅ having several His groups (neutral at 8) that become positively charged at pH values below 7.

A different study that supports CTB₅ playing a more active role than binding was conducted by Merritt and coworkers which produced a crystal structure of CTB₅ with bound GM₁ oligosaccharide molecules. Their findings show that binding of 5 GM₁

molecules per CTB₅ molecule causes peptide backbone strain between Thr92 = Pro93 and Gln49 = Val 50 [44]. They stated that this strained conformation of the backbone is required in order to form the optimal receptor-binding surface. It is possible that this strain is increased when GM₁ molecules are anchored within the membrane. An increased strain after 5-fold binding could initiate a conformational change in the B₅ pentamer that could be responsible for membrane penetration and ion channel formation.

Through our analysis, it remains unknown how the addition of DT is able to “activate” CTB₅ at both pH values even though the A subunit that contains the cleavage site is not present. DT is known to reduce disulfide bonds may cleave peptide bonds. Each B unit within the B₅ pentamer contains one disulfide bond but they are interior and not exposed to DT. Since we see no effects to the monolayer through reflectivity and GIXD we hypothesize that DT attacks other cleavage sites on the CTB₅ molecule.

The hexagonal unit cell dimensions derived from diffraction of the protein layer do not support the idea of the B₅ pentamer opening up its “doughnut hole” so that the A1 subunit can move through it to the membrane. After activation at both pH values there is a reduction in the hexagonal unit cell dimension suggesting that the B₅ pentamer is not expanding. It is possible that the A1 peptide unfolds and is “threaded” through the “doughnut hole” but the A2 unit is already there. After DT is added to CTB₅ and CTAB₅, the protein layer Bragg peaks become more pronounced. In other words, it is becoming more crystalline which is not consistent with the expansion of the B₅ pentamer.

Table 2-1.

Composition	In-Plane Bragg Peaks of CTB and CTAB Proteins (pH=5, 20 mN/m, 20°C)													
	Observed <i>d</i> -spacings ± 0.5 (Å)				Integrated Intensity** ± 1.0				Area per molecule ± 100 (Å ²)	Hex. Unit Cell <i>a</i> _{hex} (Å) ± (1.0)	In-Plane Coherence Length, <i>L</i> (Å) ± 50 Å			
	{1,0}	{1,1}	{2,0}	{2,1}	{1,0}	{1,1}	{2,0}	{2,1}			{1,0}	{1,1}	{2,0}	{2,1}
CTB	61.7	35.0	30.6	24.3	72	22	34	22	4515	72.2	650	360	250	160
CTB+DT	60.7	34.0	30.1	24.0	60	29	36	20	4366	71.0	630	180	290	160
CTAB	61.1	38.5	32.7	23.2	177	*	*	*	4640	73.2 ± 1.5	390	*	*	*
CTAB+DT	61.0	34.8	30.0	23.6	112	27	28	*	4330	70.7	415	160	210	*
	In-Plane Bragg Peaks of CTB and CTAB Proteins (pH=8, 20 mN/m, 20°C)													
CTB	63.6	35.8	31.5	24.9	80	21	32	28	4755	74.1	560	250	190	120
CTB+DT	62.4	34.7	29.9	24.2	80	42	22	39	4430	71.5	420	160	240	80
CTAB	65.7	38.8	31.2	22.7	218	*	*	*	4490	72.0 ± 2.0	270	*	*	*
CTAB+DT	64.6	36.0	30.7	22.8	139	51	49	*	4340	70.8	250	110	10	*

*impossible to get reliable data, ** intensities in arbitrary units

Table 2-2.

Out-of-Plane Bragg Rods of CTB, and CTAB, Proteins (pH=8, 20 mN/m, 20°C)					
	Height (Å)	Radius (Å)	Tilt (degrees)	Tilt dir. (degrees from NN)	Debye factor
CTB	53.9	35.5	45.1	0.14	2 Å
CTB+DT	50.4	35.4	46.3	0.03	5 Å
CTAB (population 1) 29.4%	51.6	30.0	43.9	29.9	5 Å
(population 2) 70.6%	82.6	35.0	36.1	29.9	5 Å
CTAB+DT (population 1) 50%	46.1	31.5	33.0	29.6	5 Å
(population 2) 50%	71.7	33.9	44.8	29.9	5 Å

Table 2-3.

Compo- sition	In-Plane Bragg Peaks (pH=8, 20 mN/m, 20°C)											Out-of-Plane Bragg Rods (pH=8, 20 mN/m, 20°C)									
	observed <i>d</i> -spacings ± 0.01 (Å)			Integr. Intensity ± 0.01 **	Area per molecule ± 0.02 (Å ²)	Primitive Unit Cell <i>a</i> , <i>b</i> , <i>γ</i> ± (0.01, 0.01, 0.2) (Å, Å, degrees)			Coherence Length, <i>L</i> (Å) ± 5 Å			Coherence Length, <i>L_c</i> (Å) ± 1.0		tilt angle, <i>t</i> (°) ± 2.0		tilt dir. from NN, non- symmetry (°) ± 2.0		<i>σ</i> (Å) ± 0.2		<i>χ</i> ²	
	<i>d</i> ₁₀	<i>d</i> ₀₁	<i>d</i> ₁₋₁			<i>L</i> ₁₀	<i>L</i> ₀₁	<i>L</i> ₁₋₁	<i>I</i>	<i>II</i>	<i>I</i>	<i>II</i>	<i>I</i>	<i>II</i>	<i>I</i>	<i>II</i>	<i>I</i>	<i>II</i>	<i>I</i>	<i>II</i>	
DPPE:GM ₁	4.41	4.33	4.23	1.00	43.19	4.99	4.89	117.8	223	227	474	20.0	17.4	22.0	48.8	13.7	23.6	1.1	2.8	20	22
DPPE:GM ₁ +CTB	4.45	4.35	4.23	0.83	43.56	5.01	4.90	117.4	292	123	486	20.0	16.3	24.2	53.0	13.5	23.5	1.6	2.8	15	18
DPPE:GM ₁ +CTB+DT	4.43	4.34	4.24	0.55	43.42	5.00	4.90	117.7	180	100	287	20.0	17.2	21.8	49.0	14.4	23.4	0.9	2.8	6	8
DPPE:GM ₁ +CTAB	4.45	4.36	4.24	0.53	43.68	5.01	4.91	117.4	202	205	309	*	19.3	*	43.9	*	24.1	*	2.4	*	36
DPPE:GM ₁ +CTAB+DT	4.41	4.31	4.23	0.32	43.05	5.00	4.88	118.1	180	81	356	20	18.1	20.0	45.8	14.0	23.2	0.2	2.9	26	18

Some of the Bragg rods can be fitted using two competing models depicted as *I* (low molecular tilt *t* and small root mean-square molecular displacement, *σ*) and *II* (high molecular tilt *t* and large root mean-square molecular displacement, *σ*).

*no second model exists.

** Integration of the Bragg peaks was performed through the (*q_{xy}*, *q_z*) = (1.3 -1.6 Å⁻¹, 0.0 -1.0 Å⁻¹) region and the intensities were normalized to that of pure DPPE:GM₁ (pH=8) monolayer.

L is the in-plane coherence length; an average size of the 2-D “crystalline” islands.

L_c is the length of the coherently scattering part of the alkyl tail measured along its backbone.

Table 2-4.

Compo- sition	In-Plane Bragg Peaks (pH=5, 20 mN/m, 20°C)									Out-of-Plane Bragg Rods (pH=5, 20 mN/m, 20°C)											
	observed <i>d</i> -spacings ± 0.01 (Å)			Integr. Intensity ± 0.01 **	Area per molecule ± 0.02 (Å ²)	Primitive Unit Cell <i>a</i> , <i>b</i> , <i>γ</i> ± (0.01, 0.01, 0.2) (Å, Å, degrees)			Coherence Length, <i>L</i> (Å), ± 5 Å			Coherence Length, <i>L_c</i> (Å) ± 1.0		tilt angle, <i>t</i> (°) ± 2.0		tilt dir. from NN, non- symmetry (°) ± 2.0		<i>σ_z</i> (Å) ± 0.2		<i>χ</i> ²	
	<i>d</i> ₁₀	<i>d</i> ₀₁	<i>d</i> ₁₋₁			<i>L</i> ₁₀	<i>L</i> ₀₁	<i>L</i> ₁₋₁	<i>I</i>	<i>II</i>	<i>I</i>	<i>II</i>	<i>I</i>	<i>II</i>	<i>I</i>	<i>II</i>	<i>I</i>	<i>II</i>	<i>I</i>	<i>II</i>	
DPPE:GM ₁	4.39	4.31	4.23	1.00	42.86	4.98	4.88	118.1	210	210	660	20.0	*	24.0	*	13.0	*	2.2	*		*
DPPE:GM ₁ +CTB	4.40	4.34	4.23	0.63	43.20	4.97	4.91	117.8	194	105	340	20.2	18.0	21.6	46.6	14.6	23.5	0.2	2.7	22	33
DPPE:GM ₁ +CTB+DT	4.41	4.33	4.24	0.42	43.20	4.99	4.90	118.0	160	98	237	20.5	14.2	22.6	53.1	15.3	22.8	1.2	2.6	8	9
DPPE:GM ₁ +CTAB	4.43	4.35	4.23	0.43	43.45	4.99	4.90	117.5	217	159	357	*	20.1	*	42.4	*	24.2	*	2.4	*	13
DPPE:GM ₁ +CTAB+DT	4.42	4.34	4.24	0.27	43.36	5.00	4.91	117.8	168	110	193	*	18.2	*	45.4	*	23.2	*	2.6	*	4

Some of the Bragg rods can be fitted using two competing models depicted as *I* (low molecular tilt *t* and small root mean-square molecular displacement, *σ*) and *II* (high molecular tilt *t* and large root mean-square molecular displacement, *σ*).

*no second model exists.

** Integration of the Bragg peaks was performed through the (*q_{xy}*, *q_z*) = (1.3 -1.6 Å⁻¹, 0.0 -1.0 Å⁻¹) region and the intensities were normalized to that of pure DPPE:GM₁ (pH=5) monolayer.

L is the in-plane coherence length; an average size of the 2-D “crystalline” islands.

L_c is the length of the coherently scattering part of the alkyl tail measured along its backbone.

Chapter 3: Characterization of Single Biological Membranes at the Solid-Liquid Interface by X-Ray Reflectivity

Chapter Abstract

We demonstrate that 18 keV x-rays can be used to perform reflectometry on single, phospholipid bio-membranes at the solid-liquid interface. Two different membrane systems were investigated; a single component, fluid phase membrane of 1,2-Dioleoyl-*sn*-Glycero-3-Phosphocholine (DOPC) and a two component, predominantly gel phase membrane composed of 1:9 1,2-Dilauryl-*sn*-Glycero-3-Phosphocholine (DLPC): 1,2-Distearyl-*sn*-Glycero-3-Phosphocholine (DSPC). The increased dynamic range of x-ray reflectivity over comparable neutron reflectivity measurements enabled the density distribution of the membranes to be determined with much greater precision. The increased resolution allowed subtle features in membrane structure and leaflet segregation to be revealed. Previously, characterization of biomimetic structures normal to a “buried” interface was the domain of neutron reflectivity.

Introduction:

Similar to neutron reflectivity (NR), specular x-ray reflectivity (XR) using synchrotron radiation is a powerful method for determining the structure of thin films. Because the interaction strength of neutrons with matter is typically an order of magnitude less than that for x-rays, neutrons have been considered the ideal particle for performing reflectivity measurements on samples where the beam must pass through several centimeters of material to reach a buried interface. Conversely, the usual incident energy in XR is ~10 keV, making it very surface sensitive but lacking penetration power.

As a result, XR studies have been generally limited to thin-films at the solid-air or liquid-air interface. Recently, there have been several reports on x-ray investigation of buried interfaces using high energy synchrotron radiation [45-54]. These include x-ray reflectivity and x-ray standing wave studies of thin layers at the solid-liquid interface. However, these investigations lack biological relevance.

Here, we report novel results characterizing single phospholipid bilayer membranes at the solid-water interface using 18 keV photons. Due to the great complexity of cellular membranes, their study demands simplification without losing the structure, properties and function of the bilayer. This can be accomplished by using model membranes that are designed to mimic the structure and function of cellular membranes under physiological conditions [12]. For example, investigation of lipid membranes at the solid-liquid interface enables the use of high-resolution surface science techniques including atomic force microscopy, ellipsometry, surface plasmon resonance, and neutron reflectivity. In particular, NR, where the neutron beam penetrates through the solid support, has been used to study the structure of hybrid bilayer membranes [13, 55], and polymer cushioned bilayers [56, 57]. Krueger's review provides an excellent summary of recent work in the field [12]. Utilizing the advantages of XR (described below) in tandem with the benefits of NR (*i.e.* contrast variation and little beam damage) will be extremely influential in the study of soft condensed matter systems. Fragneto and coworkers have recently discussed the use of these complementary techniques [58, 59].

In this work, we demonstrate the use of high-energy photons to characterize the structure of a 1,2-Dioleoyl-*sn*-Glycero-3-Phosphocholine (DOPC) fluid-phase bilayer and a 1:9 1,2-Dilauryl-*sn*-Glycero-3-Phosphocholine (DLPC): 1,2-Distearyl-*sn*-Glycero-3-

Phosphocholine (DSPC) predominantly gel-phase bilayer at the solid-liquid interface in bulk water. DOPC is a simple, fluid phase lipid that readily forms continuous bilayers at room temperature on solid supports, making it ideal for proof of principle experiments. Conversely, DLPC: DSPC mixtures strongly phase separate at room temperature due to a six-carbon difference in acyl chain length, making this an ideal system for probing lipid segregation and membrane in-homogeneities [60, 61].

3rd generation synchrotron x-ray source intensities are typically 10 orders of magnitude more intense than current neutron sources. Because of low incident fluxes, neutron reflectivity experiments of thin layers at the solid-liquid interface typically utilize a probed substrate area of at least 500 mm² with a length of the sample along the beam of ~50mm to maximize the signal of the reflected beam. Still, reflectivity measurements out to momentum transfer vector Q_z values of $\sim 0.2\text{--}0.3 \text{ \AA}^{-1}$ require 3-4 hours of acquisition time [13, 57, 62, 63]. This Q_z range limits the real space resolution [64]. Sample lengths of this magnitude are not tenable for x-ray reflectivity utilizing wavelengths of $\sim 1.5 \text{ \AA}$, due to beam attenuation by the liquid layer or solid-support. To overcome this, we decreased the path length of the x-rays through the liquid (water) and increased their energy. Specifically, we used single crystal quartz substrates with dimensions 10 x 50 mm² as the solid support. The substrate was placed in a water filled, stainless steel cell (with Kapton windows) (**Fig. 3-1a**) and oriented so that the 10 mm dimension was along the x-ray beam. To increase the transmission, we used high energy x-rays (18 keV, $\lambda \approx 0.65 \text{ \AA}$). These much more energetic photons penetrate through the thick water layer with a transmission of approximately 40% [65]. For comparison, the transmission is less than 1% at 10 keV. The small sample size and need for the beam to strike at very low angles

of incidence ($0.05^\circ < \theta < 2.3^\circ$) required high precision, uniformly polished, fixed slits (170 μm molybdenum) to define the vertical dimension of the x-ray beam. The horizontal slit opening was 1 mm.

At the CMC-CAT beamline at the APS synchrotron source, we measured the reflectivity from substrate-supported bilayers out to a momentum transfer of 0.5 \AA^{-1} covering 8 orders in dynamic range of intensity. This was done without the extraordinary efforts and specific circumstances needed for acquiring higher-resolution NR data [14]. We were thus able to probe electron density differences on a length scale almost two times smaller (e.g. $Q_z = 0.5$ vs 0.3 \AA^{-1}) [64]. Two bilayer compositions were investigated; fluid DOPC and 1:9 DLPC: DSPC gel-phase membranes formed by vesicle fusion [66] on single crystal quartz substrates. X-ray reflectivity scans were completed in approximately 30 minutes. Further refinements, such as an increased vertical slit size at higher angles, should allow reflectivity data collection out to Q_z values of $\sim 1.0 \text{ \AA}^{-1}$ with a commiserate increase in resolution.

Experimental Section

1,2-Dioleoyl-*sn*-Glycero-3-Phosphocholine (DOPC), 1,2-Dilauryl-*sn*-Glycero-3-Phosphocholine (DLPC), and 1,2-Distearyl-*sn*-Glycero-3-Phosphocholine (DSPC), were purchased from Avanti Polar Lipids (Birmingham, AL) and used without further purification. Lipid bilayers were prepared by conventional vesicle fusion. Lipids were dissolved and mixed in chloroform ($\sim 10 \text{ mg/mL}$) and dried using nitrogen while vortexing to create thin layers on the walls of the vial. The lipids were then hydrated to a lipid concentration of 0.5 mg/mL using Millipore water and heated above the lipid phase transition temperature. The vesicle solution was then tip probe sonicated at low power for

30 seconds to produce small unilamellar vesicles of diameter ~ 50 nm. The lipid solutions ($T > T_{\text{melt}}$) were then deposited on room temperature polished substrates made of single-crystal quartz (dimensions $10 \times 50 \text{ mm}^2$). Before deposition, the substrates were submerged in a freshly made piranha acid bath (70% sulfuric acid, 30% H_2O_2 , $T \sim 55^\circ\text{C}$) for 15 minutes and then cleaned with UV ozone for 10 minutes.

All synchrotron x-ray measurements were carried out using the 6-circle diffractometer at the ID-9 (undulator) CMC-cat beam line at the Advanced Photon Source (APS), Argonne National Laboratory (ANL) (Argonne, IL). The synchrotron x-ray beam was monochromated to a wavelength of 0.69 \AA (18 keV) by a cryogenic Kohzu double crystal monochromator containing a feedback loop with a position sensitive ion-chamber in front of the sample for beam position stability. The error bars on the data represent the statistical errors in the measurements (standard deviation, σ_R) where the uncertainty in the Q_z resolution, $\sigma_{Q_z}/Q_z \approx 2\%$, was nearly constant over this scattering vector range. At low angles, the beam footprint was larger than the sample length. Therefore, the intensity of the incident beam intercepted by the sample was not constant over the entire Q_z range. This effect of increasing intensity with angle was clearly seen in the reflectivity measurement of a bare quartz substrate in H_2O (data not shown). To account for this difference, the data [67] was renormalized by dividing the specular reflectivity by $\sin\theta$ up to the angle where the size of the beam footprint equaled the sample length along the beam. The high precision, fixed slit defined the angle at which the correction ended. After applying this renormalization procedure to the bare quartz substrate, the data closely followed the theoretical reflection for a quartz substrate with a 4 \AA roughness, as expected. This renormalization procedure was applied to all data

reported. The scattering length density of x-rays is defined by multiplying the electron density [$e^{-}/\text{\AA}^3$] of the material by $2.82E^{-5}$ \AA .

Neutron reflectivity measurements were performed on the time-of-flight SPEAR beamline at the Manuel Lujan Neutron Scattering Center, Los Alamos National Laboratory. The beam footprint was fixed at 10 mm x 50 mm. As the neutron flux was low, radiation damage to the sample was negligible. Incoherent scattering from the sample was a significant contribution to the background, which limited the q_z range over which reflectivity data could be collected. Neutron reflectivities down to $R \sim 1 \times 10^{-7}$, and momentum transfers out to $q_z \sim 0.3 \text{\AA}^{-1}$, could be measured in 3 hrs. The uncertainty of the qz resolution, σ_{qz}/qz , including instrumental resolution, was approximately 3% for the entire range of scattering vectors.

Results and Discussion

The results from a fluid DOPC bilayer deposited by vesicle fusion are shown in **Fig. 3-1**. A simple 4-slab XR model, based on the Parratt algorithm [20], fits the data with a reduced χ^2 value of 5.3 with only small deviation in the scattering length density (SLD) profile from the free form, model independent, cubic beta spline approach [19]. Sigma, σ , is the RMS roughness of the interface with the error function defined as a normalized Gaussian. The thickness of the hydrocarbon region was 23.2 \AA . This value is in excellent agreement with the theoretical calculation of 24 \AA for a fluid phase bilayer (80 \AA^2 /lipid) with 18 carbons per lipid tail [68, 69]. From the model, it can also be seen that the outer headgroup region has a lower scattering length density than the inner headgroup region, indicative of higher water content. In addition, the thickness of the outer headgroup region was 10 \AA with a 6 \AA roughness, while the inner headgroup

thickness was 8Å with a 3.8Å roughness. This finding is consistent with a reduction in motion of the inner leaflet lipids due to interactions with the solid support and a concomitant reduction of fluctuations [70, 71]. The bilayer was separated from the quartz substrate by a thin 4Å water layer. For comparison, we also measured this sample using neutron reflectivity. In both cases, the length scales of the four slabs were consistent between NR and XR (**Table 3-1**). These findings for the DOPC bilayer are also in agreement with work published by Johnson *et al* of neutron reflectivity done on a DMPC lipid bilayer at the quartz-water interface [72].

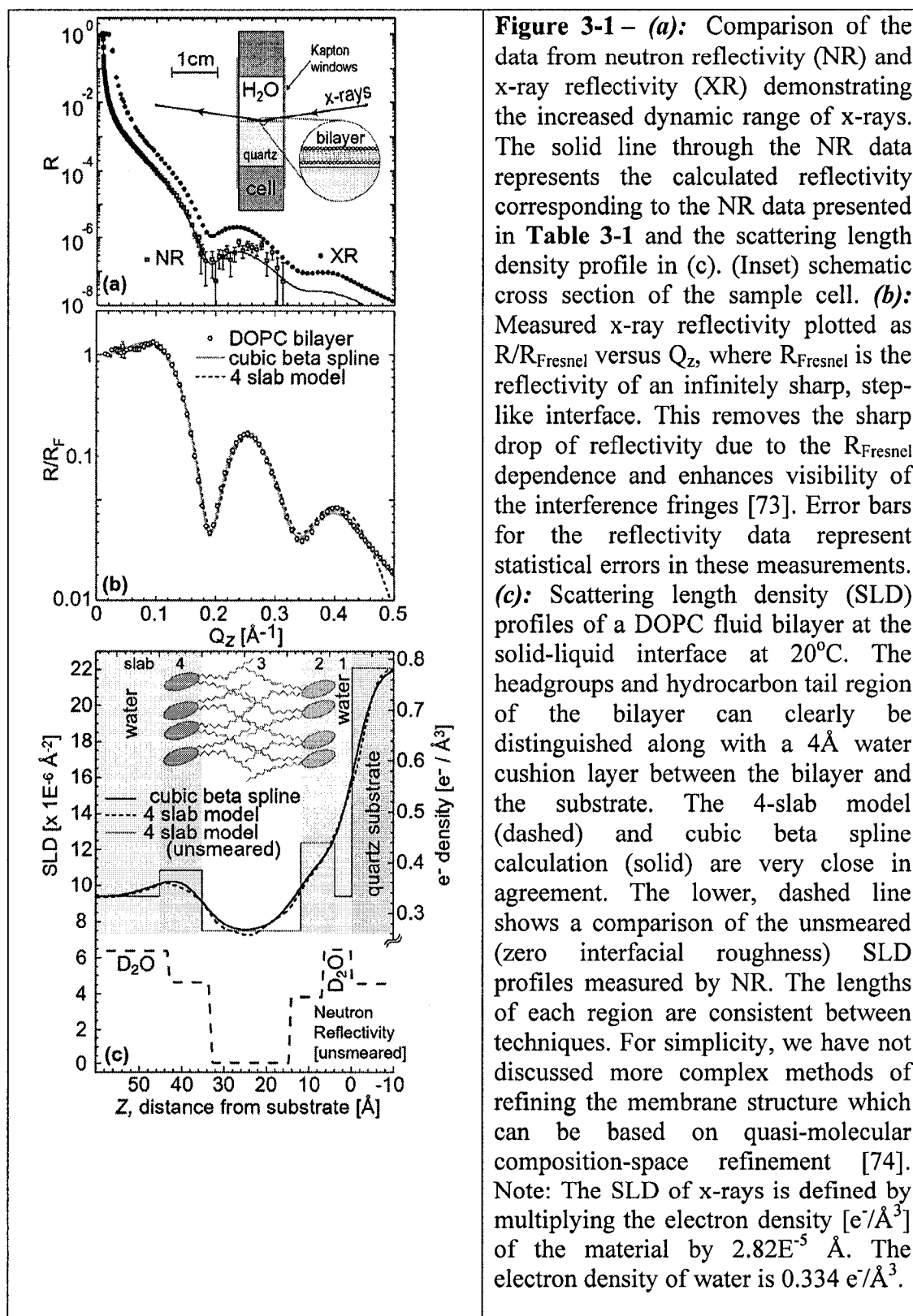


Table 3-1:

DOPC 4-Slab Model Fitting Parameters

	$\chi^2 = 5.3$	XR 4-Slab Model			NR
Slab	Region	Z [Å] ±0.5	SLD [$\times 10^{-6} \text{Å}^{-2}$] ±0.3	σ [Å] ±0.5	Z [Å] ±2
	Bulk H ₂ O		9.4 _F		
4	PC head	10.0	10.9	6.0	9.7
3	Tails	23.2	7.5	4.4	19.2
2	PC head	8.0	12.4	5.5	8.0
1	H ₂ O layer	4.0	9.4 _F	3.8	5.9
0	Quartz		22.1 _F	4.2	

_F – signifies parameters fixed during refinement.

σ – refers to interfacial roughness. Errors bars were estimated by the change in the parameter needed to increase the reduced χ^2 by 1.

The reflectivity profile from a 1:9 DLPC: DSPC bilayer deposited by vesicle fusion is shown in **Fig. 3-2**. At room temperature, these lipids phase separate due to their large difference in tail length (18 carbons for DSPC and 12 carbons for DLPC). The phase transition temperature (T_{melt}) of DLPC is -2°C , and T_{melt} for DSPC is 55°C [69]. There are several possible arrangements of the two lipid components. For example, previous studies using atomic force microscopy (AFM), determined that DSPC and DLPC phase separated into coupled domains with an 18Å height difference [61].

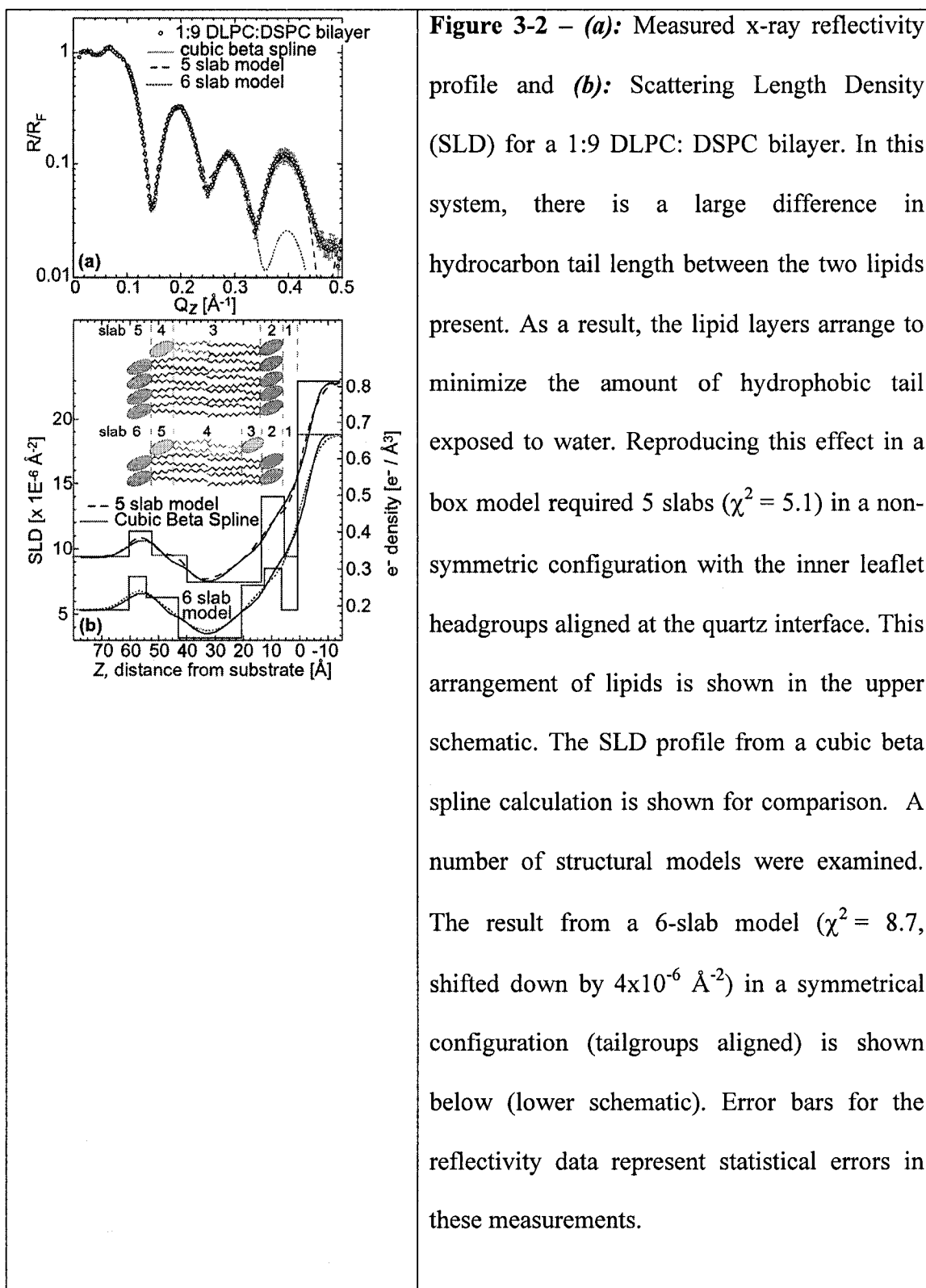


Table 3-2:

DLPC: DSPC (1:9) Box Model Fitting Parameters

Slab	Region	$\chi^2 = 5.1$ 5-Slab Model			Slab	Region	$\chi^2 = 8.7$ 6-Slab Model		
		Z [Å] ±0.5	SLD [$\times 10^{-6} \text{Å}^{-2}$] ± 0.3	σ [Å] ±0.5			Z [Å] ±0.5	SLD [$\times 10^{-6} \text{Å}^{-2}$] ± 0.3	σ [Å] ±0.5
	Bulk H ₂ O		9.4 _F			Bulk H ₂ O		9.4 _F	
5	DSPC head	8.1	11.3	3.9	6	DSPC head	6.1	11.9	5.0
4	DLPC head	12.5	9.5	3.3	5	DLPC head	11.3	10.3	4.0
3	Tails	26.4	7.4	3.0	4	Tails	22.4	7.2	7.5
2	DSPC head	8.1	14.0	10.7	3	DLPC head	8.1	11.2	7.8
1	H ₂ O layer	4.7	9.4 _F	4.7	2	DSPC head	6.0	12.5	4.6
0	Quartz		22.9	5.7	1	H ₂ O layer	5.7	9.4 _F	4.8
					0	Quartz		22.8 _F	5.7

Refer to **Table 3-1** for symbol definitions. High values of some roughness parameters may suggest a need to divide the profile into more slabs or to use a quasi-molecular distribution function approach to account for a more diffused electron density profile [74].

Our modeling took into account several membrane structures including phase separation, preferential leaflet segregation and leaflet coupling with either inner leaflet headgroups aligned or tailgroups aligned between leaflets. Two specific models are depicted schematically in **Fig. 3-2b**. Although the lipid components in the mixture are expected to phase separate, the composite membrane must be relatively flat (low variation in film thickness) due to coupling with the substrate and the absence of significant off-specular scattering in the reflectivity data. Overall, we found that the best fit to the data (lowest χ^2) required 5 slabs (upper schematic). As summarized in **Table 3-2**, the best fit was consistent with (1) a water cushion, (2) a pure DSPC headgroup region, (3) a tail region consisting of an inner DSPC leaflet and outer mixed leaflet of DSPC and DLPC tails, (4) a mixed DSPC tail/DLPC headgroup, and (5) an outer DSPC headgroup/water region. In all cases, 5-slab models drove the hydrocarbon tail region (slab 3) to a thickness of $26 \pm 2 \text{Å}$, which is significantly larger than the expected thickness

of two fully stretched C₁₂ chains for DLPC (e.g. 19Å), a strong indication of preferential leaflet segregation. The inner leaflet headgroup SLD of $14.0 \times 10^{-6} \pm 0.3 \times 10^{-6} \text{Å}^{-2}$ also matches well to the expected SLD for gel-phase DSPC. Because the interaction of the membrane with the substrate suppresses fluctuations [70, 71], it is entropically less costly for the gel-phase DSPC to preferentially segregate to the inner leaflet compared to fluid-phase DLPC. We hypothesize that this is the driving force for the observed leaflet segregation. However, because the difference in SLD between gel-phase and fluid-phase tails is small, we cannot unequivocally rule out the inverse of this model - preferential segregation of DLPC to the inner leaflet. Again, a 5-6Å water “cushion” layer between the bilayer and the substrate was required in good agreement with our results for DOPC. We also tested various 6-slab models [75] including a symmetric profile (about the plane where the alkyl tails meet) that contained four headgroup regions (two for the DLPC headgroup and two for the DSPC headgroup) as shown in **Fig. 3-2b** (bottom schematic). This more complicated model resulted in a larger χ^2 value (8.7 vs. 5.1), demonstrating that XR provides adequate resolution to distinguish between these various models.

In conclusion, x-ray reflectivity has the resolution increase needed to distinguish between these real-space structures. In all our studies extreme care was used to minimize damage caused by the high flux x-ray beam by frequently moving the sample perpendicular to the beam during specular scans. As can be seen from our results, there is high correspondence of the SLD profiles between the cubic spline and slab model fits. The differences at high Q_z regions between the model fits and the data may be due to the following factors: errors in renormalization procedure, simplicity of the slab models, a need for more sophisticated fitting procedures to describe the SLD of the membranes

[74], and possible beam damage. A natural extension of these studies is to probe in-plane membrane/bilayer structure using grazing incidence diffraction (work in progress), a technique inaccessible to neutrons and previously limited to lipid monolayers at the liquid-air interface.

The ability to do x-ray reflectivity measurements at the solid-solution interface enabled the density distribution of lipid membranes to be measured in a previously inaccessible manner. The increased resolution allowed subtle features in membrane structure and leaflet segregation to be revealed. The advantages of using x-rays over neutrons are higher flux (increased resolution), smaller sample sizes, faster measurements using more accessible synchrotron sources, no requirements of using expensive deuterated molecules, and the opportunity of exploiting grazing incidence diffraction. We have been successful in measuring the grazing incidence diffraction of 12.5 bilayers of cadmium arachidate at the solid-liquid interface that have been deposited by the Langmuir-Blodgett technique (results not shown) [76]. The cadmium ion complex with arachidic acid headgroups forms a highly crystalline structure that gives clear in-plane diffraction peaks. This demonstrates the feasibility of achieving in-plane diffraction of a lipid bilayer. These successful measurements of bilayers at the solid-liquid interface will lead to a new arsenal of x-ray experiments on other biological systems and thin films.

Chapter 4: Grazing Incidence Diffraction of Cadmium Arachidate Multilayers at the Solid-Liquid Interface

Chapter Abstract

Using complementary x-ray reflectivity (XR) and grazing incidence x-ray diffraction (GIXD), we report structural studies of supported thin-organic layers in contact with water and air. Using a monochromatic synchrotron beam to penetrate 10 mm of liquid, we have characterized buried films composed of 12.5 repeating bilayers of arachidic acid ($C_{20}H_{40}O_2$) complexed with cadmium ions (cadmium arachidate, $CdAr_2$). We found that the layered structure of the $CdAr_2$ multilayers do not exhibit rearrangement after exposure to water with negligible water penetration into the inner layers when compared to their dry state. These findings are consistent with the formation of extremely robust $CdAr_2$ multilayers that can withstand multiple rinses in strong organic solvents, acid, and mechanical wear. The second goal was to demonstrate the feasibility of similar experiments to study much thinner single bilayer bio-membranes. These studies are the first successful GIXD experiments of ultra thin-organic film composed of a few layers at the solid-liquid interface.

Introduction

A current trend in interfacial science is the utilization of ultra thin organic films, including single bio-membranes, which are structurally ordered on the molecular level. These films usually involve molecules that assemble into ordered films at the solid-air or solid-liquid interface. Potentially, ordered organic films may have applications in nonlinear optics [77, 78], molecular electronics, chemical/biochemical sensors, and surface patterning [79]. Maintaining the structural integrity of these ordered films when

exposed to bulk solvents or wet environments will further enhance their utility. As a result, understanding their physical properties under various conditions is vital.

A great deal of work has been done to characterize such ordered films at the solid-air or air-liquid interfaces [24, 31]. In particular, x-ray reflectivity (XR) and grazing incidence diffraction (GIXD) using synchrotron x-ray radiation have unique capabilities for determining the spatial organization of organic thin films with almost angstrom resolution [36]. Unfortunately, due to absorption and diffuse scattering by water, it is not clear that the GIXD signal would be sufficient to characterize the structure of ordered films composed of only a few multilayers in contact with liquid. In this work, we report the first successful GIXD experiments of a thin-organic film composed of 12.5 repeating CdAr₂ bilayers at the solid-liquid interface in water.

These successful investigations of 12.5 CdAr₂ bilayers allude to the feasibility of using GIXD to study solid-supported single bilayer membranes at the solid-liquid interface. Recent work has shown that GIXD can be used to study highly-oriented, phospholipid multilayers composed of thousands of bilayers in humid environments [80, 81]. It is known that stacked lipid membrane lamella have different structural characteristics than single membranes in contact with a solid support. Therefore, it is imperative to study the in-plane structure of single bilayers due to their more relevant application in biomembrane sensors.

Experimental Section

Cadmium arachidate multilayers were prepared by conventional Langmuir-Blodgett (LB) deposition [82]. Arachidic acid (C₂₀H₄₀O₂) dissolved in chloroform (1 mg/mL) was spread on a subphase consisting of Millipore water with 1 mM CdCl₂ and

10 mM ACES buffer (pH 6.8). The dipping process was performed at a constant surface pressure (30 mN/m) and dipping speed (5 mm/min). The monolayers were deposited on polished substrates made of single-crystal quartz. Before deposition, the substrates were submerged in a freshly made piranha acid bath (70% sulfuric acid, 30% H₂O₂) for 15 minutes and then cleaned with UV ozone for 10 minutes. The substrates were pulled through the interface 25 times, starting in the subphase and ending in air. The transfer ratio was equivalent for all 25 depositions, confirming uniform stacking of monolayers. When measuring at the solid-liquid interface, the samples were submerged in water or buffer on a time scale of 1-2 hours prior to exposure to x-rays.

X-ray Reflectivity

All synchrotron x-ray measurements were carried out using the 6-circle diffractometer at the ID-9 (undulator) CMC-cat beam line at the Advanced Photon Source (APS), Argonne National Laboratory (ANL) (Argonne, IL). The synchrotron x-ray beam was monochromated to a wavelength of 0.69 Å (18keV) by a cryogenic Kohzu double crystal monochromator containing a feedback loop with a position sensitive ion-chamber in front of the sample for beam position stability. We used single crystal quartz substrates with dimensions 10 x 50 mm² as the solid support. After CdAr₂ deposition the substrate was placed in a water filled, stainless steel cell (with Kapton windows) and oriented so that the 10 mm dimension was along the x-ray beam. The 18keV photons penetrated through the 10mm thick water layer with a transmission of approximately 40%. The small sample size (along the dimension of the beam) and need for the beam to strike at very low angles required ultra high precision, fixed slits (170 μm molybdenum) to define the vertical dimension of the x-ray beam. The horizontal slit opening was 1 mm.

Using the above setup, we measured the reflectivity from substrate-supported CdAr₂ multilayers out to a momentum transfer of about 0.8 Å⁻¹ covering almost 10 orders in dynamic range of intensity with reasonable statistics. Typical scanning times for this qz range were 10 minutes. The reflected x-rays were counted using a NaI scintillation detector. Error bars on the data represent the statistical errors in the measurements (standard deviation, σR). Since at low angles the footprint of the beam is bigger than the size of the quartz substrate the measured reflectivities have been corrected for this effect.

Reflectivity, R , is defined as the intensity ratio of x-rays specularly scattered from the surface relative to the incident x-ray beam intensity. When measured as a function of wave-vector transfer ($qz = |\mathbf{k}_{\text{out}} - \mathbf{k}_{\text{in}}| = 4\pi \sin \theta / \lambda$, where θ is the angle of incidence and λ is the wavelength of the x-ray beam, see **Fig. 4-1**), the reflectivity curve contains information regarding the sample-normal profile of the in-plane average of the coherent scattering length densities. By modeling the deviation of the measured specular x-ray reflectivity from Fresnel's law for a perfect interface, detailed information on the average electron density distribution in the direction normal to the interface can be determined. Analysis of the measured reflectivity curves was performed by dividing the structural components of the system (along the substrate normal) into homogeneous slabs or boxes of constant electron density. These boxes, which physically represent different portions of the cadmium arachidate layers (hydrocarbon tails and CO₂⁻-Cd-CO₂⁻ headgroups), were then refined using the Parratt formalism [20] and least-squared minimization method. The uncertainty in the momentum transfer vector, $\Delta qz = 0.003 \text{ \AA}^{-1}$, was included in the data fitting. This analysis provides the thickness of each layer (box), electron density ($e(z)$), and adjacent interfacial Gaussian roughness (σ), to account for roughening

at the boundary due to static or thermal roughness. Consequently, the structural components perpendicular to the interface can be resolved.

Grazing Incidence Diffraction

At the air-water interface, prior to LB deposition onto the solid substrate, each of the deposited CdAr₂ monolayers is composed of 2D ordered domains with random orientation about the direction normal to the subphase surface, and can therefore be described as a 2D powder [83, 84]. Due to the nature of the LB procedure and the presence of the quartz support, the deposited CdAr₂ layers orient into lamellas parallel to the substrate. For the GIXD experiments (**Fig. 4-1**), the x-ray beam was adjusted to strike the surface at an incident angle of 0.05°, which corresponds to the vertical momentum transfer vector $q_z = 0.625 q_c$, where $q_c = 0.0254 \text{ \AA}^{-1}$ is the critical scattering vector for total external reflection for quartz submerged in water (e -densities of quartz and water are $0.84 \text{ e}^{-}/\text{\AA}^3$ and $0.33 \text{ e}^{-}/\text{\AA}^3$, respectively). At this angle the incident wave is totally reflected, while the refracted wave becomes evanescent traveling along the substrate surface. Such a configuration maximizes surface sensitivity. GIXD geometry is shown **Fig. 4-1**. The dimension of the incoming x-ray beam footprint on the quartz surface was approximately 1 mm x 10 mm. For in-plane diffraction measurements, a NaI scintillation counter was placed behind adjustable slits on a translational stage (moving in-plane with the substrate interface along the $2\theta_{\text{hor}}$ angle) covering a q_{xy} range of 1.3 \AA^{-1} to 1.9 \AA^{-1} . For rod scans (scans along q_z vector), the in-plane scattering angle was kept fixed at the position of maximal Bragg intensity and the height of the NaI detector above the surface was varied. The vertical slit opening of 1mm in front of the detector determined the q_z resolution of 0.013 \AA^{-1} .

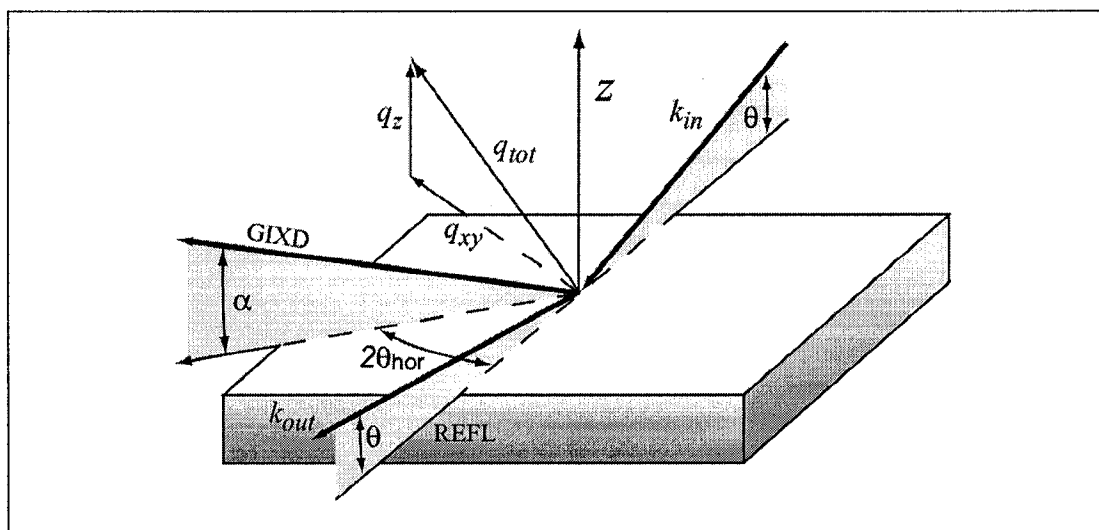


Fig. 4-1: Scattering geometry for grazing incidence diffraction (GIXD) and X-ray Reflectivity (XR). For GIXD, the angle of incidence, θ , of the x-ray beam is less than the angle of total external reflection from the substrate in contact with the superstrate (water or air). k_{in} and k_{out} are the wave vectors of the incident and reflected beams. The scattering vector $q_{xy} \approx 4\pi\sin\theta_{hor}/\lambda$ is parallel to the substrate plane and $q_z = 2\pi\sin\alpha/\lambda$ is perpendicular to it. For reflectivity measurements, $2\theta_{hor}$ is equal to zero and the intensity is recorded as a function of angle θ in specular geometry.

For the collection of diffracted intensities, a scintillation NaI detector with slits in front of it was used. The slits were adjusted to give the horizontal resolution of the measurement (along the quartz surface), $FWHM_{resol}(q_{xy}) = 0.0084 \text{ \AA}^{-1}$. The scattered intensity was measured by scanning over a range of the horizontal scattering vector component, q_{xy} (or $q_{||}$) $\cong (4\pi/\lambda)\sin(2\theta_{hor}/2)$, where $2\theta_{hor}$ is the angle between the incident and diffracted beam projected onto the horizontal quartz plane. Such a scan, integrated over the vertical acceptance of the slit (0.042 \AA^{-1}) along the q_z direction, yields in-plane

Bragg peaks (Fig. 4-3a). Conversely, the scattered intensity recorded with narrow vertical slits of the resolution $FWHM_{resol}(q_z) = 0.013 \text{ \AA}^{-1}$ along q_z ($q_z = q_{\perp} = (2\pi/\lambda)\sin(\alpha)$), where α is the exit angle measured from the surface of the substrate) produced q_z -resolved scans called *rod scans* (Fig. 4-3b, 4-3c). *Rod scans* were measured at the scattering vector q_{xy} corresponding to maximum intensity of the in-plane Bragg peak and background subtracted. The scattering of x-rays along rods perpendicular to the quartz substrate reflects the presence of well-oriented (textured) lamellas of CdAr_2 . The intensity distribution along the in- and out-of-plane Bragg peaks can be analyzed to yield information on the packing of the cadmium arachidate molecules. The positions $q_{tot} = (q_{xy}^2 + q_z^2)^{1/2}$ of the Bragg peaks allow the determination of the d -spacings, $d = 2\pi/q_{tot}$, for the 3D lattice and calculation of the 3-D unit cell dimensions. The width of the Bragg peaks corrected for the instrumental resolutions, give the finite size of the crystalline domains in the direction of the reciprocal scattering vector q_{xy} (the 2D in-plane crystalline coherence length, L_{xy}) and in the direction perpendicular to it (out-of-plane crystalline coherence length, L_z) according to the Scherrer formula:

$$L_{xy,z} \cong 0.9 [2\pi / FWHM_{intrinsic}(q_{xy,z})]$$

where FWHM are the corresponding full width at half maximum heights of the peaks [40]. The intrinsic FWHM can be obtained using the equation:

$$FWHM_{intrinsic}(q_{xy,z}) = [FWHM_{meas}(q_{xy,z})^2 - FWHM_{resol}(q_{xy,z})^2]^{1/2}$$

Beam Damage

As a precaution against beam damage, in XR the sample was frequently translated by 2mm, in the horizontal plane, perpendicular to the incoming beam. Re-recording part of the reflectivity curve before and after translation afforded a check of the

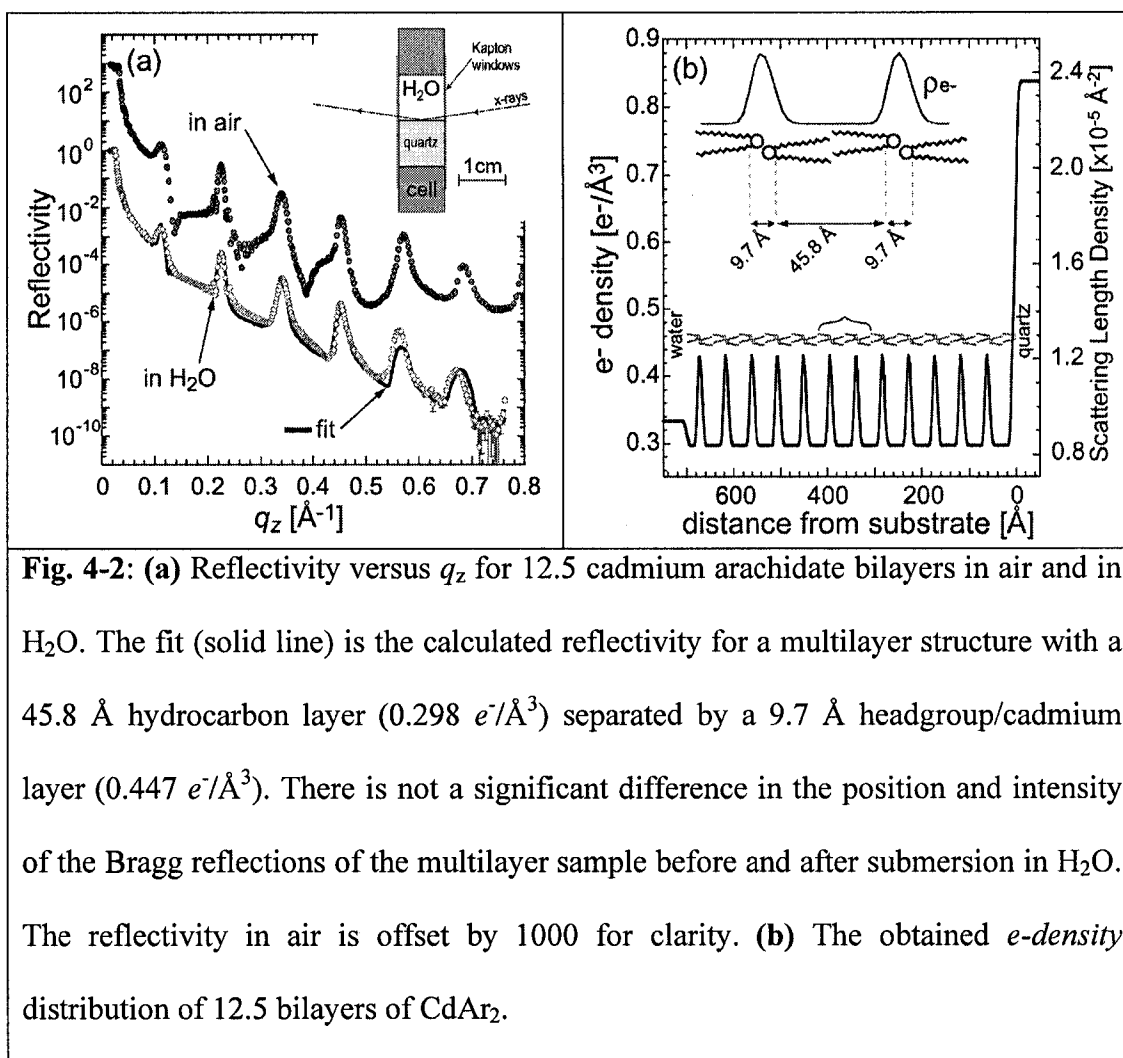
reproducibility. During reflectivity, the maximum dose of x-rays was estimated by the equivalent number of seconds exposed to the direct, un-attenuated beam. Similarly, translation of the sample by 2mm was performed between GIXD scans. The total scan time for a single GIXD scan was approximately 2 minutes.

Results

Reflectivity

Comparison of reflectivity profiles of supported CdAr₂ multilayers in air and water (Fig. 4-2) demonstrates no significant change in the position or intensity of the peaks. The same box model, adjusted only for differences in the electron density of the superstrate, air vs. water, fits both reflectivity profiles. This finding demonstrates that the multilayer structure is not significantly altered by submersion in water. The solid line (Fig. 4-2a) is the calculated reflectivity for a multilayer structure composed of 45.8 Å thick hydrocarbon bilayers (22.9Å per monolayer, $\rho_e=0.298 e^-/\text{Å}^3$) separated by 9.7 Å thick headgroup/cadmium/headgroup layers (CO₂⁻-Cd-CO₂⁻, $\rho_e=0.447 e^-/\text{Å}^3$). The hydrocarbon layer represents two arachidic acid chains in a tail-to-tail configuration (Fig. 4-2b). A fully stretched 19-carbon chain extends approximately 24 Å (1.26 Å/Carbon). As reflectivity is sensitive to the density distribution normal to the surface the model thickness of 22.9Å suggests that the hydrocarbon tails are tilted ~17° with respect to the surface normal. The obtained *e-density* (0.298 e⁻/Å³) and thickness for the hydrocarbon tail region corresponds to an average area per molecule of 22.4 Å². Based on this number and the fitted *e-density* of the headgroup region (0.447 e⁻/Å³) we can estimate that on average there are 1.1 - 1.2 Cd²⁺ ions per two CO₂⁻ headgroups. The consistency in the *e-*

density of the tails in air and water indicates that there is no water penetration into the interior of the hydrocarbon bilayers. Based on the reflectivity data we can calculate the volume fraction averaged e -density of CdAr₂ multilayers. The obtained value of $0.324 e^-/\text{\AA}^3$ is less than the electron density of water ($0.33 e^-/\text{\AA}^3$).



Grazing Incidence Diffraction

The GIXD from 12.5 bilayers of cadmium arachidate (CdAr₂) at the solid-water interface is shown in **Fig. 4-3a**. Two peaks with Miller indices of $(1, 1, l)$ and $(0, 2, l)$ are clearly resolved along the q_{xy} vector. Analysis of the Bragg peak positions are summarized in **Table 4-1 and 4-2** and reveal an orthorhombic unit cell of dimensions:

$a=4.86 \text{ \AA}$, $b=7.45 \text{ \AA}$, $c= 48.82 \text{ \AA}$. These values are in agreement with previous work in air [85, 86]. There are four molecules per unit cell where the projection of the area on the a, b plane occupied by one molecule is equal to 18.2 \AA^2 . This is in contrast to an overall average molecular area of 22.4 \AA^2 from reflectivity measurements and shows that the crystalline (diffracting) domains pack more efficiently. Moreover, the volume fraction of disordered CdAr₂ phase is significant. The in-plane coherence lengths, L_{xy} , were 260 \AA and 230 \AA for the $(1, 1, l)$ and $(0, 2, l)$ Bragg peaks, respectively. These in-plane coherence lengths correspond to approximately 45 to 50 molecules in positional, in-plane, registry.

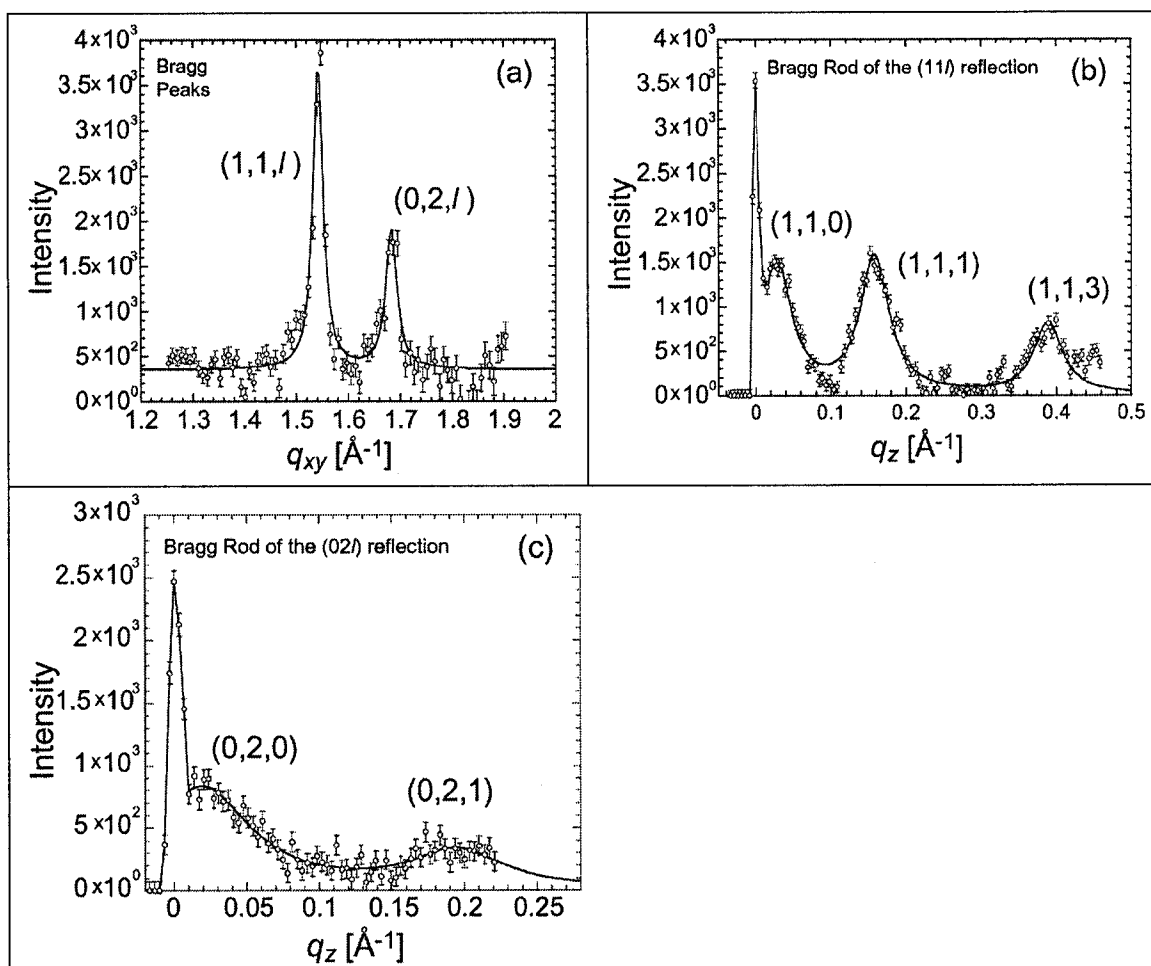


Fig. 4-3: Grazing incidence diffraction (GIXD) of 12.5 bilayers of cadmium arachidate (CdAr₂) at the quartz-water interface. (a) Bragg peak positions are in excellent agreement with those obtained at the solid-air interface showing that there is no significant rearrangement of the layers when exposed to water. (b) and (c) show the (1, 1, *l*) and (0, 2, *l*) rod scans, respectively, of the peaks in (a).

Table 4-1.

Parameters obtained from in-plane GIXD scans.

Cd-arachidate	q_{xy} positions (Å ⁻¹)	<i>d</i> -spacing (Å)	peak FWHM (Å ⁻¹)	Coherence length, L_{xy} (Å)
(1,1, <i>l</i>)	1.542	4.08	0.023	260
(0,2, <i>l</i>)	1.683	3.73	0.026	230

The (1, 1, l) rod scan is shown in **Fig. 4-3b**. The (1, 1, 0), (1, 1, 1), and (1, 1, 3) Bragg reflections can be clearly resolved along the q_z vector. The (0, 2, l) rod scan is shown in **Fig. 4-3c**. Analysis of the all measured Bragg rods is summarized in **Table 4-2**. The out-of-plane coherence lengths, L_z , for the (1,1,0) (1,1,1) (1,1,3), (0,2,0) and (0,2,1) reflections are much smaller than the depth of penetration of the x-ray beam (**Fig. 4-4b**) and smaller than the corresponding in-plane coherence lengths. Along the (1,1, l) rod, the coherence length (L_z) is equal to 130Å, which, on average, is equivalent to approximately 2.7 CdAr₂ bilayers of the multi-lamellar film in positional registry. Along (0,2, l) rod this number ($L_z = 70$ Å) decreases even further to approximately 1.4 bilayers. The difference in the L_z of the (1, 1, l) and (0, 2, l) rod scans is most likely due to more disorder of the CdAr₂ molecules perpendicular to the (0, 2, 0) plane. Since the maximum of the (1, 1, 0) reflection is slightly off from $q_z \approx 0$ Å⁻¹ and the maximum of the (0, 2, 0) reflection coincides with $q_z \approx 0$ Å⁻¹, the molecules are slightly tilted towards the a -axis of the unit cell in the plane spanned by the a and c vectors. These off horizon reflections are consistent with the molecular tilt observed by the reflectivity data.

Table 4-2.

Parameters obtained from out-of-plane GIXD scans.

Cd-arachidate	q_z position (Å ⁻¹)	peak FWHM (Å ⁻¹)	Coherence length, L_z (Å)
(1,1, l)			
(1,1,0)	0.028	0.046	130
(1,1,1)	0.158	0.046	130
(1,1,3)	0.389	0.046	130
(0,2, l)			
(0,2,0)	0.019	0.081	70
(0,2, 1)	0.195	0.078	70

Our results for CdAr₂ multilayers at the solid liquid interface compare very well to GIXD measurements of 21 monolayers of CdAr₂ at the solid-air interface performed by Tippman-Krayer *et al* [86]. Both Bragg peaks and Bragg rods match, showing that there is no significant rearrangement of the CdAr₂ layers when exposed to water. This finding is also consistent with our reflectivity results showing no water penetration into inner layers. The intensity distribution between the (1, 1, *l*) and (0, 2, *l*) rod scans also compare favorably with the work of Tippman-Krayer *et al*, suggesting that there is a ¼ of a unit cell displacement of the consecutive layers along the *a*-axis of the bilayers.

In our case the *c*-dimension of the unit cell is smaller than that reported by Tippman-Krayer *et al*. This indicates that the molecular tilt is bigger in our case, perhaps due to the difference in the LB deposition protocol. Since the averaged electron density of CdAr₂ is less than the electron density of water there is no total reflection when the x-ray beam passes from liquid into the multilayers. An incident angle of 0.05° guarantees almost full illumination of the structure normal to the interface. However, in order to understand the exact distribution of the electric field as a function of depth inside the CdAr₂ multilayer structure, we recursively calculated the electric field using Parratt's method [20, 87]. This calculation was based on the electron density distribution obtained from reflectivity measurements. Due to the interference between transmitted and reflected beams within the film, standing waves are present as function of incident angle and the distance along the sample normal (**Fig. 4-4a**).

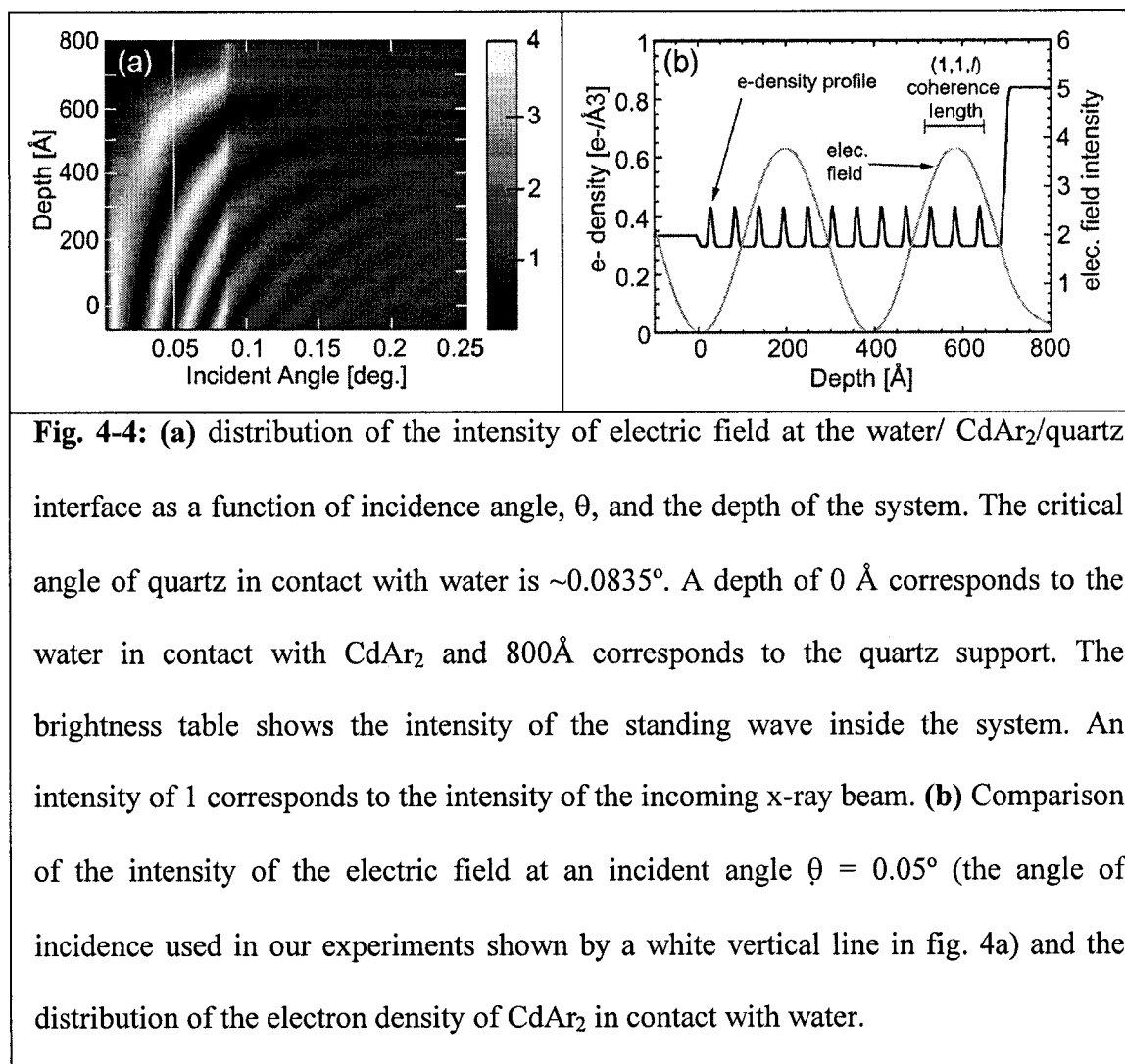


Fig. 4-4: (a) distribution of the intensity of electric field at the water/ CdAr₂/quartz interface as a function of incidence angle, θ , and the depth of the system. The critical angle of quartz in contact with water is $\sim 0.0835^\circ$. A depth of 0 Å corresponds to the water in contact with CdAr₂ and 800 Å corresponds to the quartz support. The brightness table shows the intensity of the standing wave inside the system. An intensity of 1 corresponds to the intensity of the incoming x-ray beam. (b) Comparison of the intensity of the electric field at an incident angle $\theta = 0.05^\circ$ (the angle of incidence used in our experiments shown by a white vertical line in fig. 4a) and the distribution of the electron density of CdAr₂ in contact with water.

Below the critical angle of quartz in contact with water ($\sim 0.0835^\circ$), strong interference leads to large oscillations of the electric field intensity – *i.e.* the standing wave. **Fig. 4-4b** shows the real space comparison of the electron distribution of the CdAr₂ multilayers and the calculated intensity of x-ray electric field. Approximately 70% of the total thickness of the CdAr₂ multilayers ($\sim 500\text{Å}$) experiences x-ray electric field intensities greater than the intensity of the incoming beam. **Fig. 4-4b** also illustrates that the maximum out-of-plane coherence length (130 Å) obtained in the experiment is less than the depth of the illuminated portion of the structure.

Discussion/Conclusions

Many biological applications require the structure of assembled layers to be maintained when exposed to an aqueous phase. This necessitates the ability to characterize these thin-films at the solid-liquid interface since layers may have different properties when in contact with water. We have shown that the structure of 12.5 CdAr₂ bilayers is preserved after submersion in water with no water penetration into the interior of the layers.

According to our knowledge, this is the first GIXD measurement at the solid-liquid interface of a sample that wasn't composed of "thousands" of layers. Several studies pursuing the GIXD of these much thicker multilayer systems have been successful in very humid environments [80, 81]. With careful improvements to our studies, 12.5 bilayers will be decreased to a single bilayer, enabling the measurement of single biomembranes on a solid support in contact with water. A thorough working knowledge of the lateral organization of solid-supported single bilayers will aid the development of biomembranes sensors.

Acknowledgments

This work was supported under the auspices of the United States Department of Energy through collaborative UC/Los Alamos Research (CULAR) Grant No. 9853 and DOE PECASE Award 05419-0099-2K. The Manuel Lujan Jr., Neutron Scattering Center is a national user facility funded by the United States Department of Energy, Office of Basic Energy Sciences-Materials Science, under contract W-7405-ENG-36 with the University of California. We acknowledge the support of the National Institute of

Standards and Technology, U.S. Department of Commerce, in providing the neutron research facilities used in this work. We gratefully thank Thorsten Dieckmann at the Chemistry Department, University of California at Davis for NMR spectrometer time and analysis. This work was also supported by the Searle Scholars Program/the Chicago Community Trust (01-L-108), University of California directed research. Work at the CMC Beamline is supported in part by the Office of Basic Energy Sciences of the U.S. Dept. of Energy and by the National Science Foundation Division of Materials Research. Use of the Advanced Photon Source is supported by the Office of Basic Energy Sciences of the U.S. Department of Energy under Contract No. W-31-109-Eng-38. We thank Zhang Jiang, graduate student at UCSD (Prof. Sunil K. Sinha's group), for calculating the distribution of the electric field inside the CdAr₂ multilayer sample and Dr. C. Braun (HMI-Berlin, Germany) for the Parratt32 reflectivity program. We would also like to thank Dawn Y. Takamoto for her advice pertaining to cadmium arachidate deposition and Dennis J. Mulder, graduate student at UCD (Prof. Tonya L. Kuhl's group), for his assistance with the beamline measurements.

References

1. Middlebrook JL, et al., *Bacterial Toxins - Cellular Mechanisms of Action*. Microbiological Reviews, 1984. **48**(3): p. 199-221.
2. Zhang RG, et al., *The Three-Dimensional Crystal Structure of Cholera Toxin*. Journal of Molecular Biology, 1995. **251**(4): p. 563-573.
3. Zhang RG, et al., *The 2.4 Angstrom Crystal Structure of Cholera Toxin B Subunit Pentamer - Choleraegenoid*. Journal of Molecular Biology, 1995. **251**(4): p. 550-562.
4. Mekalanos JJ, et al., *Enzymic Activity of Cholera Toxin .2. Relationships to Proteolytic Processing, Disulfide Bond Reduction, and Subunit Composition*. Journal of Biological Chemistry, 1979. **254**(13): p. 5855-5861.
5. Holmgren J, *Actions of Cholera-Toxin and the Prevention and Treatment of Cholera*. Nature, 1981. **292**(5822): p. 413-417.

6. Venienbryan C, et al., *Characterization of the Growth of 2d Protein Crystals on a Lipid Monolayer by Ellipsometry and Rigidity Measurements Coupled to Electron Microscopy*. Biophysical Journal, 1998. **74**(5): p. 2649-2657.
7. Lauer S, et al., *Analysis of cholera toxin-ganglioside interactions by flow cytometry*. Biochemistry, 2002. **41**(6): p. 1742-1751.
8. Ribic HO, et al., *3-Dimensional Structure of Cholera-Toxin Penetrating a Lipid-Membrane*. Science, 1988. **239**(4845): p. 1272-1276.
9. Yuan CB, et al., *Distribution of ganglioside GM1 in L-alpha-dipalmitoylphosphatidylcholine/cholesterol monolayers: A model for lipid rafts*. Biophysical Journal, 2000. **79**(5): p. 2768-2781.
10. Yuan CB, et al., *Atomic force microscopy studies of ganglioside GM1 domains in phosphatidylcholine and phosphatidylcholine/cholesterol bilayers*. Biophysical Journal, 2001. **81**(2): p. 1059-1069.
11. Terrettaz S, et al., *Protein-Binding to Supported Lipid-Membranes - Investigation of the Cholera-Toxin Ganglioside Interaction by Simultaneous Impedance Spectroscopy and Surface-Plasmon Resonance*. Langmuir, 1993. **9**(5): p. 1361-1369.
12. Krueger S, *Neutron reflection from interfaces with biological and biomimetic materials [Review]*. Current Opinion in Colloid & Interface Science, 2001. **6**(2): p. 111-117.
13. Majkrzak CF, et al., *First-principles determination of hybrid bilayer membrane structure by phase-sensitive neutron reflectometry*. Biophysical Journal, 2000. **79**(6): p. 3330-3340.
14. Krueger S, et al., *Investigation of hybrid bilayer membranes with neutron reflectometry: Probing the interactions of melittin*. Langmuir, 2001. **17**(2): p. 511-521.
15. Kent MS, et al., *Segment concentration profile of myoglobin adsorbed to metal ion chelating lipid monolayers at the air-water interface by neutron reflection*. Langmuir, 2002. **18**(9): p. 3754-3757.
16. Weygand M, et al., *Structural reorganization of phospholipid headgroups upon recrystallization of an S-layer lattice*. Journal of Physical Chemistry B, 2002. **106**(22): p. 5793-5799.
17. Weygand M, et al., *Bacterial S-layer protein coupling to lipids: X-ray reflectivity and grazing incidence diffraction studies*. Biophysical Journal, 1999. **76**(1 Part 1): p. 458-468.
18. Naumann C, et al., *Hydration of DPPC Monolayers at the Air/Water Interface and Its Modulation by the Nonionic Surfactant C(12)E(4) - a Neutron Reflection Study*. Langmuir, 1995. **11**(10): p. 3948-3952.
19. Pedersen JS, et al., *Analysis of Neutron and X-Ray Reflectivity Data by Constrained Least-Squares Methods*. Physica B, 1994. **198**(1-3): p. 16-23.
20. Parratt LG, *Surface Studies of Solids by Total Reflection of X-Rays*. Physical Review, 1954. **95**(2): p. 359-369.
21. Braslau A, et al., *Capillary Waves on the Surface of Simple Liquids Measured by X-Ray Reflectivity*. Physical Review A, 1988. **38**(5): p. 2457-2470.
22. Majewski J, et al., *Packing of ganglioside-phospholipid monolayers: An X-ray diffraction and reflectivity study*. Biophysical Journal, 2001. **81**(5): p. 2707-2715.

23. Small DM, *Phase Equilibria and Structure of Dry and Hydrated Egg Lecithin*. Journal of Lipid Research, 1967. **8**: p. 551-557.
24. Helm CA, et al., *Phospholipid Monolayers between Fluid and Solid States*. Biophysical Journal, 1987. **52**(3): p. 381-390.
25. Helm CA, et al., *Phases of Phosphatidyl Ethanolamine Monolayers Studied by Synchrotron X-Ray-Scattering*. Biophysical Journal, 1991. **60**(6): p. 1457-1476.
26. Faller R, et al., *Modeling the binding of cholera-toxin to a lipid membrane by a non-additive two-dimensional hard disk model*. Soft Materials, 2003. **in press**.
27. Grigera TS, et al., *Fast Monte Carlo algorithm for supercooled soft spheres - art. no. 045102*. Physical Review E, 2001. **63**04(4 Part 2): p. 5102-+.
28. Faller R, et al., *Density of states of a binary Lennard-Jones glass*. Journal of Chemical Physics, 2003. **119**(8): p. 4405-4408.
29. Faller R, et al., *Constant pressure hybrid molecular dynamics-Monte Carlo simulations*. Journal of Chemical Physics, 2002. **116**(1): p. 55-59.
30. Feng Y, et al., *Retrograde transport of cholera toxin from the plasma membrane to the endoplasmic reticulum requires the trans-Golgi network but not the Golgi apparatus in Exo2-treated cells*. Embo Reports, 2004. **5**(6): p. 596-601.
31. Miller CE, et al., *Cholera toxin assault on lipid monolayers containing ganglioside GM(1)*. Biophysical Journal, 2004. **86**(6): p. 3700-3708.
32. Rodighiero C, et al., *A cholera toxin B-subunit variant that binds ganglioside G(M1) but fails to induce toxicity*. Journal of Biological Chemistry, 2001. **276**(40): p. 36939-36945.
33. Hazes B, et al., *Accumulating evidence suggests that several AB-toxins subvert the endoplasmic reticulum-associated protein degradation pathway to enter target cells*. Biochemistry, 1997. **36**(37): p. 11051-11054.
34. Lencer WI, et al., *Membrane traffic and the cellular uptake of cholera toxin*. Biochimica Et Biophysica Acta-Molecular Cell Research, 1999. **1450**(3): p. 177-190.
35. Bretscher MS, et al., *Cholesterol and the Golgi-Apparatus*. Science, 1993. **261**(5126): p. 1280-1281.
36. Als-Nielsen J, et al., *Principles and applications of grazing incidence x-ray and neutron scattering from ordered molecular monolayers at the air-water interface [review]*. Physics Reports-Review Section of Physics Letters, 1994. **246**(5): p. 252-313.
37. Majewski J, et al., *Packing of ganglioside-phospholipid monolayers: An X-ray diffraction and reflectivity study*. Biophysical Journal, 2001. **81**(5): p. 2707-2715.
38. Faller R, et al., *Modeling the binding of cholera toxin to a lipid membrane by a non-additive two-dimensional hard-disk model*. Soft Materials, 2003. **1**(3): p. 343-352.
39. Krasilnikov OV, et al., *The Ionic Channels Formed by Cholera-Toxin in Planar Bilayer Lipid-Membranes Are Entirely Attributable to Its B-Subunit*. Biochimica Et Biophysica Acta, 1991. **1067**(2): p. 166-170.
40. Guinier A, *X-ray diffraction in crystals, imperfect crystals, and amorphous bodies*. 1963, San Francisco: W. H. Freeman.

41. Vineyard GH, *Grazing-Incidence Diffraction and the Distorted-Wave Approximation for the Study of Surfaces*. Physical Review B, 1982. **26**(8): p. 4146-4159.
42. Tomasi M, et al., *Lipid Insertion of Cholera-Toxin after Binding to Gm1-Containing Liposomes*. Journal of Biological Chemistry, 1981. **256**(21): p. 1177-1181.
43. McCann JA, et al., *Conformational Changes in Cholera Toxin B Subunit Ganglioside Gm1 Complexes Are Elicited by Environmental Ph and Evoke Changes in Membrane Structure*. Biochemistry, 1997. **36**(30): p. 9169-9178.
44. Merritt EA, et al., *The 1.25 angstrom resolution refinement of the cholera toxin B-pentamer: Evidence of peptide backbone strain at the receptor-binding site*. Journal of Molecular Biology, 1998. **282**(5): p. 1043-1059.
45. Roser SJ, et al., *Energy-Dispersive X-Ray Reflection from a Liquid-Liquid Interface*. Langmuir, 1994. **10**(10): p. 3853-3856.
46. Schlossman ML, *Liquid-liquid interfaces: studied by X-ray and neutron scattering [Review]*. Current Opinion in Colloid & Interface Science, 2002. **7**(3-4): p. 235-243.
47. Richter AG, et al., *In situ and interrupted-growth studies of the self-assembly of octadecyltrichlorosilane monolayers*. Physical Review E, 2000. **61**(1): p. 607-615.
48. Rieutord F, et al., *High-energy x-ray reflectivity of buried interfaces created by wafer bonding*. Physical Review B, 2001. **63**12(12): p. 5408.
49. Reichert H, et al., *A new X-ray transmission-reflection scheme for the study of deeply buried interfaces using high-energy microbeams*. Physica B: Condensed Matter, 2003. **336**(1-2): p. 46-55.
50. Engemann S, et al., *Interfacial melting of ice in contact with SiO₂*. Physical Review Letters, 2004. **92**20(20): p. 5701.
51. Scherb G, et al., *A novel thick-layer electrochemical cell for in situ x-ray diffraction*. Review of Scientific Instruments, 1998. **69**(2): p. 512-516.
52. Wang J, et al., *Structure Changes in Model Membranes Monitored by Variable Period X-Ray Standing Waves - Effect of Langmuir-Blodgett Film Thickness on Thermal Behavior*. Journal of Physical Chemistry, 1994. **98**(42): p. 10957-10968.
53. Wang J, et al., *Direct profiling and reversibility of ion distribution at a charged membrane/aqueous interface: An X-ray standing wave study*. Langmuir, 2001. **17**(12): p. 3671-3681.
54. Zhang RT, et al., *Membrane Structure Characterization Using Variable-Period X-Ray Standing Waves*. Biophysical Journal, 1998. **74**(4): p. 1924-1936.
55. Koenig BW, et al., *Neutron Reflectivity and Atomic Force Microscopy Studies of a Lipid Bilayer in Water Adsorbed to the Surface of a Silicon Single Crystal*. Langmuir, 1996. **12**(5): p. 1343-1350.
56. Wong JY, et al., *Polymer-cushioned bilayers. I. A structural study of various preparation methods using neutron reflectometry*. Biophysical Journal, 1999. **77**(3): p. 1445-1457.
57. Majewski J, et al., *Structural Studies of Polymer-Cushioned Lipid Bilayers*. Biophysical Journal, 1998. **75**(5): p. 2363-2367.

58. Fragneto G, et al. *Fluctuations of model membranes: complementarity of neutron and x-ray studies*. in *Proceeding of The 20th General Conference of the Condensed Matter Division - European Physics Society*. 2004. Prague.
59. Fragneto G, et al., *Neutron and X-Ray reflectivity studies at solid-liquid interfaces: the interaction of a peptide with model membranes*. *Physica B*, 2000. **276**: p. 501-502.
60. Faller R, et al., *Simulation of domain formation in DLPC-DSPC mixed bilayers*. *Langmuir*, 2004. **20**(18): p. 7686-7693.
61. Ratto TV, et al., *Obstructed diffusion in phase-separated supported lipid bilayers: A combined atomic force microscopy and fluorescence recovery after photobleaching approach*. *Biophysical Journal*, 2002. **83**(6): p. 3380-3392.
62. Hughes AV, et al., *Phase behavior of DMPC free supported bilayers studied by neutron reflectivity*. *Langmuir*, 2002. **18**(21): p. 8161-8171.
63. Krueger S, et al., *Extending the Angular Range of Neutron Reflectivity Measurements from Planar Lipid Bilayers - Application to a Model Biological Membrane*. *Langmuir*, 1995. **11**(8): p. 3218-3222.
64. Perez-Salas UA, et al., *Characterization of a biomimetic polymeric lipid bilayer by phase sensitive neutron reflectometry*. *Langmuir*, 2003. **19**(19): p. 7688-7694.
65. Henke BL, et al., *X-Ray Interactions - Photoabsorption, Scattering, Transmission and Reflection at $E=50-30,000$ Ev, $Z=1-92$* . *Atomic Data and Nuclear Data Tables*, 1993. **55**(2): p. 349-349.
66. McKiernan AE, et al., *Cytoskeletal Protein Binding Kinetics at Planar Phospholipid Membranes*. *Biophysical Journal*, 1997. **73**(4): p. 1987-1998.
67. , Background was measured off the specular beam (on both sides of the specular reflection) for all points and rocking curve scans were performed at several incidence angles to check alignment.
68. Marra J, et al., *Direct Measurements of Forces between Phosphatidylcholine and Phosphatidylethanolamine Bilayers in Aqueous-Electrolyte Solutions*. *Biochemistry*, 1985. **24**(17): p. 4608-4618.
69. Marsh D, *CRC Handbook of Lipid Bilayers*. 1990: CRC Press, Inc.
70. Kuhl TL, et al., *A Neutron Reflectivity Study of Polymer-Modified Phospholipid Monolayers at the Solid-Solution Interface - Polyethylene Glycol-Lipids on Silane-Modified Substrates*. *Biophysical Journal*, 1998. **75**(5): p. 2352-2362.
71. Hetzer M, et al., *Asymmetric molecular friction in supported phospholipid bilayers revealed by NMR measurements of lipid diffusion*. *Langmuir*, 1998. **14**(5): p. 982-984.
72. Johnson SJ, et al., *Structure of an Adsorbed Dimyristoylphosphatidylcholine Bilayer Measured with Specular Reflection of Neutrons*. *Biophysical Journal*, 1991. **59**(2): p. 289-294.
73. Als Nielsen J, et al., *Principles and Applications of Grazing Incidence X-ray and Neutron Scattering from Ordered Molecular Monolayers at the Air-Water Interface [Review]*. *Physics Reports-Review Section of Physics Letters*, 1994. **246**(5): p. 252-313.
74. Schalke M, et al., *Submolecular organization of DMPA in surface monolayers: beyond the two-layer model*. *Biochimica et Biophysica Acta - Biomembranes*, 2000. **1464**(1): p. 113-126.

75. Note, Other 6-slab models consistently degenerated into a 5-slab model similar to the 5-slab model reported in Table II.
76. Miller CE, et al., *Grazing Incidence Diffraction of Cadmium Arachidate Multilayers at the Solid-Liquid Interface*. Zeitschrift fuer Krystallographie, 2005: p. In Press.
77. Li DQ, et al., *Chromophoric Self-Assembled Multilayers - Organic Superlattice Approaches to Thin-Film Nonlinear Optical-Materials*. Journal of the American Chemical Society, 1990. **112**(20): p. 7389-7390.
78. Wang H, et al. *Engineering Nanoscaled Nonlinear Optical Thin Film via Langmuir-Blodgett Technique*. in *Pacific Rim Conference on Lasers and Electro-Optics*. 2003. Taipei, Taiwan.
79. Roberts GG, *An Applied Science Perspective of Langmuir-Blodgett Films*. Advances in Physics, 1985. **34**(4): p. 475-512.
80. Munster C, et al., *Grazing incidence X-ray diffraction of highly aligned phospholipid membranes containing the antimicrobial peptide magainin 2*. European Biophysics Journal with Biophysics Letters, 2000. **28**(8): p. 683-688.
81. Spaar A, et al., *Conformation of peptides in lipid membranes studied by X-ray grazing incidence scattering*. Biophysical Journal, 2004. **87**(1): p. 396-407.
82. Takamoto DY, et al., *Stable ordering in Langmuir-Blodgett films*. Science, 2001. **293**(5533): p. 1292-1295.
83. Leveiller F, et al., *2-Dimensional Crystal-Structure of Cadmium Arachidate Studied by Synchrotron X-Ray-Diffraction and Reflectivity*. Langmuir, 1994. **10**(3): p. 819-829.
84. Leveiller F, et al., *Crystallinity of the Double-Layer of Cadmium Arachidate Films at the Water-Surface*. Science, 1991. **252**(5012): p. 1532-1536.
85. Vitta S, et al., *Structural assembly of Cd-arachidate molecules in multilayers*. Journal of Chemical Physics, 1999. **111**(24): p. 11088-11094.
86. Tippmann-Krayer P, et al., *Thickness and Temperature-Dependent Structure of Cd-Arachidate Langmuir-Blodgett-Films*. Thin Solid Films, 1992. **210**(1-2): p. 577-582.
87. Tolan M, *X-ray scattering from soft-matter thin films - Materials science and basic research - Introduction*. X-Ray Scattering from Soft-Matter Thin Films, 1999. **148**: p. 1-+.